Experimental and Numerical Study of the Mechanical Aspects of the Stitch Bonding Process in Microelectronic Wire Bonding

by

Alireza Rezvanigilkolaee

A thesis
presented to the University of Waterloo
in fulfilment of the
thesis requirement for the degree of
Doctor of Philosophy
in
Mechanical Engineering

Waterloo, Ontario, Canada, 2014

AUTHOR'S DECLARATION

I hereby declare that I am the sole author of this thesis. This is a true copy of the thesis, including any required final revisions, as accepted by my examiners. I understand that my thesis may be made electronically available to the public.

Abstract

The goal of this thesis is to improve the understanding of the stitch bonding process in micro-electronic wire bonding. In particular, it focuses on investigating the effect of the process parameters bonding force, scrub amplitude, and skid on experimental bond quality responses, including qualitative (non-sticking, sticking, and tail-lifting) and quantitative (stitch pull force, tail pull force). In addition to the experimental work, a finite element (FE) model is developed for the stitch bonding process using ABAQUS software, and compared with the experimental observations.

For the first set of experiments, the stitch bonding is performed with a 18 μm diameter Pd coated Cu (PCC) wire on a "low bondability" Au/Ni/Pd plated quad-flat non-lead (QFN) substrate. Results showed that a high bonding force, a high scrub amplitude, and a positive skid provoke the sticking of the stitch bond and reducing the chance of non-sticking observation. However, such parameters also increase the chance of tail-lifting. As a trade-off for a low bondability substrate, a process parameter combination containing a high bonding force and a high scrub amplitude and a negative skid could ensure a strong enough stitch bonding process with low chance of tail-lifting.

For the second set of experiments, the stitch bonding is performed with a 18 μm diameter uncoated Cu wire on a "high bondability" Ag plated QFN substrate. Statistical analysis of stitch and tail pull force showed that the skid and scrub parameters have a more significant influence than bonding force. A positive skid can degrade the stitch pull force, while enhancing the tail pull force. A high scrub amplitude is found to degrade both the stitch and the tail pull forces. The bonding force is shown to improve the stitch and tail pull forces slightly. Performing an optimization, process parameters of 70 gf (687 mN) bonding force, 3 μm scrub amplitude, and zero skid result in acceptable stitch and tail pull forces, along with a reliable stitch bond appearance (low peeling and shallow capillary tool impression).

The influence of the process parameters is significantly different depending on if bonding on low or high bondability substrates. For example, a positive skid increases the chances of sticking and tail-lifting on low bondability substrate, but it decreases the tail pull force and increases the tail pull force for high bondability substrate. This indicates that finding a general experimental rule for understanding the effect of process parameters on the stitch bond quality is difficult if not impossible. In other words, instead of general rule, it is more likely to find individual rules for specific individual applications.

To improve the understanding of stitch bonding a three dimensional (3D) dynamic explicit FE model is developed in ABAQUS. The model components and boundary conditions are constructed and applied to reflect the experimental conditions. The bonding force, scrub, and skid are successfully implemented into the model. Mass scaling is applied carefully to save calculation time while ensuring there are no artificial effects of inertia. The model is able to render the conventional responses reported in the past including stress and strain distributions. However, these conventional outputs were not sufficient to provide a correlation between model and experiment. Therefore, new candidate responses were developed and extracted from the numerical results. The new responses are based on accepted welding mechanisms.

One of the mechanisms is interfacial cleaning by frictional energy which is beneficial for bonding. Thus the friction energy accumulated during the simulated bond duration is extracted as a candidate response. For classical cold welding processes, the interfacial surface expansion is a key mechanism, as it opens up cracks in the surface contamination and oxide layers and thereby generates paths to bring the fresh metals together under pressure. Therefore, candidate responses related to surface expansion at the contact interface are extracted from the model.

The complete set of new responses extracted from the numerical model includes contact areas, surface expansion per areas, frictional energy, and combination of frictional energy combined with surface expansions per areas. In addition the bond interface is divided into “wedge” and “tail” regions. The model is run for the same DOE cells as used in the first set of experiments and candidate responses are extracted and compared with the experimental observations. By ranking the correlation coefficients of each individual candidate responses, for the first time correlations that are relatively strong are found between a numerical response and experimental observations of stitch bonding. Responses that have correlation coefficients of 0.79 and 0.85 were found for wedge sticking and tail-lifting, respectively. Such relatively strong correlation indicates that the friction enhanced cleaning and the surface expansion mechanisms are proper theories for the current stitch bonding system. These theories can be used for developing similar models for other types of the solid-state bonding processes.

Based on the best candidate responses, a procedure to determine numerical process windows is demonstrated for a specific application. Such a window defines the parameter ranges which result in an acceptable stitch bonding process and is an excellent indication of how suitable a process is for mass production. Depending on the application, materials, geometries, and tools, the FE model and process window procedure allow a variety of numerical process windows to be produced and compared.

Acknowledgments

I would like to express my sincere appreciation to my advisor Prof. Michael Mayer for his invaluable guidance, constructive discussion, and encouragement, without which this work would not have been possible. My appreciation is extended to the members of the Examination Committee: Prof. Norman Zhou, Prof. Shahrzad Esmaeili, Prof. Kaan Inal, Prof. Vassili Karanassios, and Prof. Ibrahim Guven for their scholarly suggestions, advices and examination in the whole process.

I am indebted to Mr. J. Brunner for his support and useful feedback at different times during my PhD work. I thank Dr. I. Qin, Dr. A. Shah, Dr. H. Xu, Dr. H. Clauberg, Dr. W. Song, Dr. J. Moon, Mr. J. Persic, Mr. S. Hong, Mrs. C. Nan, and Mr. G. Schulze for their support. I thank all my labmates and friends in Waterloo and Kulicke and Soffa Industries for their useful advice and support throughout this research.

Last but not the least, I am greatly indebted to my parents Mr. G. Rezvani and Mrs. N. Rezvani, and my sibling M for their continued moral support and love. Their sacrifices in making this work a reality is gratefully acknowledged.

This research was made possible by generous financial support from Kulicke and Soffa Industries (K&S), the Natural Sciences and Engineering Research Council (NSERC) of Canada, University of Waterloo Graduate Scholarship, and University of Waterloo International Doctoral Student Award.

To my loving family

Table of Contents

List of Figures

List of Tables

1 Introduction

This chapter provides an overview of the microelectronic wire bonding process and its importance and share in the IC manufacturing industry. In particular, the stitch bonding process is explained together with its current status and trend in the industry. Finally, the objectives and structure of this thesis are explained.

1•1 Background

Wire bonding is an important manufacturing step in the microelectronics packaging industry. It is used to make interconnections between metallic bond pads on the chip (die) and the substrate (lead). By 2012, 85% of all ICs (about 160 million units) were interconnected by wire bonding technology. There are other technologies for making such interconnections such as flip chip bonding, through silicon via (TSV), and others. These new interconnection techniques are growing fast and it is estimated that by 2017 they will provide interconnections for 20% of all ICs and wire bonding will provide interconnection for 80% of all ICs. However the absolute number of ICs interconnected is growing, and by 2017 there will be about 190 billion ICs interconnected by wire bonding (about 30 billion more ICs than in 2013) [1]. This shows clearly the important role of the wire bonding technology in microelectronics semiconductor industry and market [1,2]. Wire bonding is a low temperature - low cost process with excellent yield and flexibility making it the most used interconnection technique [1-13]. In the normal wire bonding process, a small diameter metallic wire (typically 20 μm diameter) is bonded with a tool firstly to a metal layer on the microchip (typically Al) and then to a metal layer on the packaging, leading to form an interconnection [14]. Wire bonds encapsulated in an integrated circuit (IC) package and a free-standing wire bonding loop are schematically shown in Figs. 1 (a) and (b), respectively. The most widely used method is thermosonic ball bonding in which ultrasonic energy is combined with thermal energy under a normal bonding force to form the bond. A first bond (also called ball bond) is normally placed on the chip side, and a second bond (also called wedge or stitch bond) is normally placed on the larger scale substrate side. It is widely accepted that the wire bonding is a solid state process, i.e. contains no melting. A proper selection of bonding temperature and a surface cleaning process usually are required [1-2].

For some more recent types of packages such as Quad Flat No-Lead (QFN) it has been shown that the application of ultrasonic vibration is problematic as it could cause severe failures in the bonding processes. The main reason is the resonance of the package lead finger with the frequency of the ultrasonic vibration and breakage of already bonded wires due to ultrasonic fatigue during the process. The solutions for bonding this type of substrates are either an ultra careful optimization of the process or replacing the ultrasonic vibration with other types of motions with lower frequencies called scrub or skid [15-23].

The ongoing trends in the microelectronics industry are smaller package sizes and lower cost of the processes and materials. With the increasing demands of integrated circuits (ICs), new and improved methods need to follow these trends [24].

1•2 Ball - Stitch Process Description

Ultrasonic vibration, low frequency XY motions, and thermal energy are used to form the wire bonds. A tool (capillary) is used to hold the wire during the process and provide normal bonding load, ultrasonic vibration, and XY motion during the bonding process. The capillary is fixed to the horn at a location as shown in Fig. 2.

The bonding process can be described as a succession of individual steps as illustrated in Fig. 3 and listed in the following

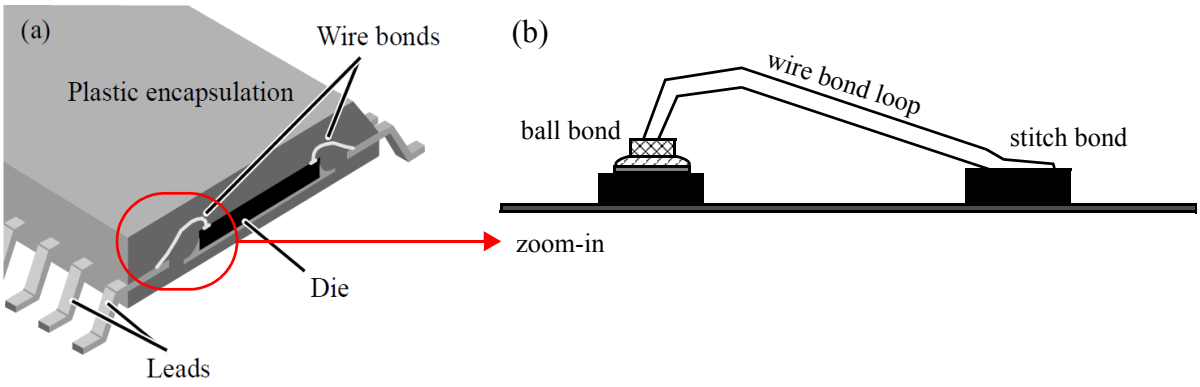

Fig. 1 (a) Wire bond position in an integrated circuit (IC) [14], (b) wire bonding loop description.

1. An electrical spark is applied to a tail of wire and melts the wire end which coils up in a molten drop and after the spark is turned off the drop immediately solidifies to form the free air ball (FAB).

2. The FAB is moved with the capillary tool towards the bonding area until it touches. Then, bond force and ultrasound or lower frequency motions are applied to the capillary tool and the heat is applied to the substrate.

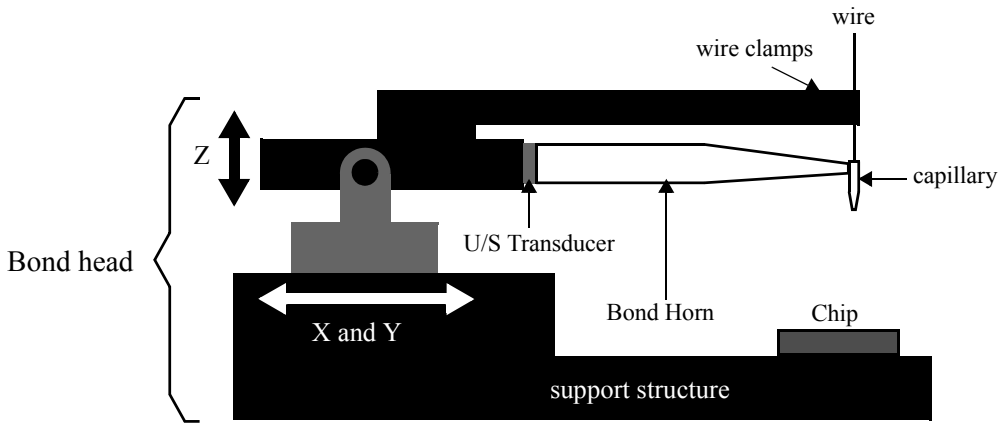

Fig. 2 Bond head and support structure of wire bonder.

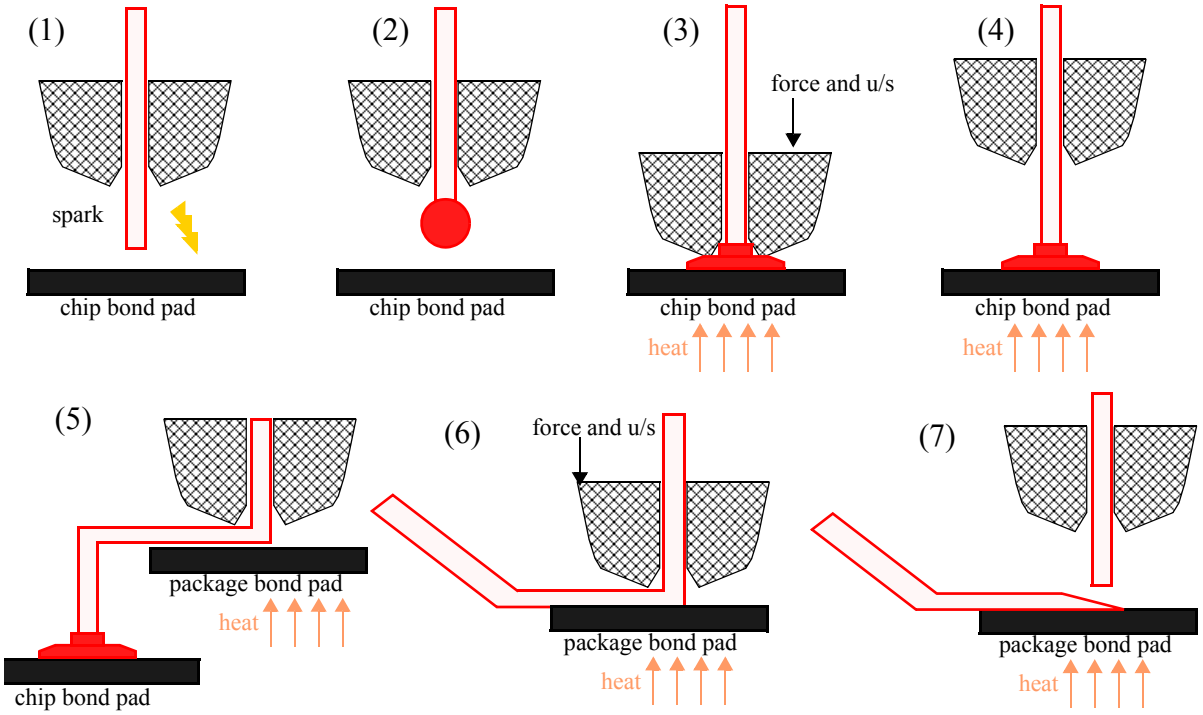

Fig. 3 Different steps of ball-stitch wire bonding.

3. Ball bond formation is completed.
4. The capillary rises.
5. A loop is formed.
6. The stitch bond is completed by means of bond force, ultrasound or low frequency XY motions, and heat.
7. After the stitch bond formation, the wire clamp closes and the wire breaks at the tail bond, so a new tail is formed and the process continues [25].

The stitch bond process is a complex process that includes normal force, ultrasonic vibration or other low frequency XY motions and heating. An SEM image and schematic pictures of the stitch bond [34] and the adjacent tail bond are shown in Figs. 4 (a) - (c), respectively.

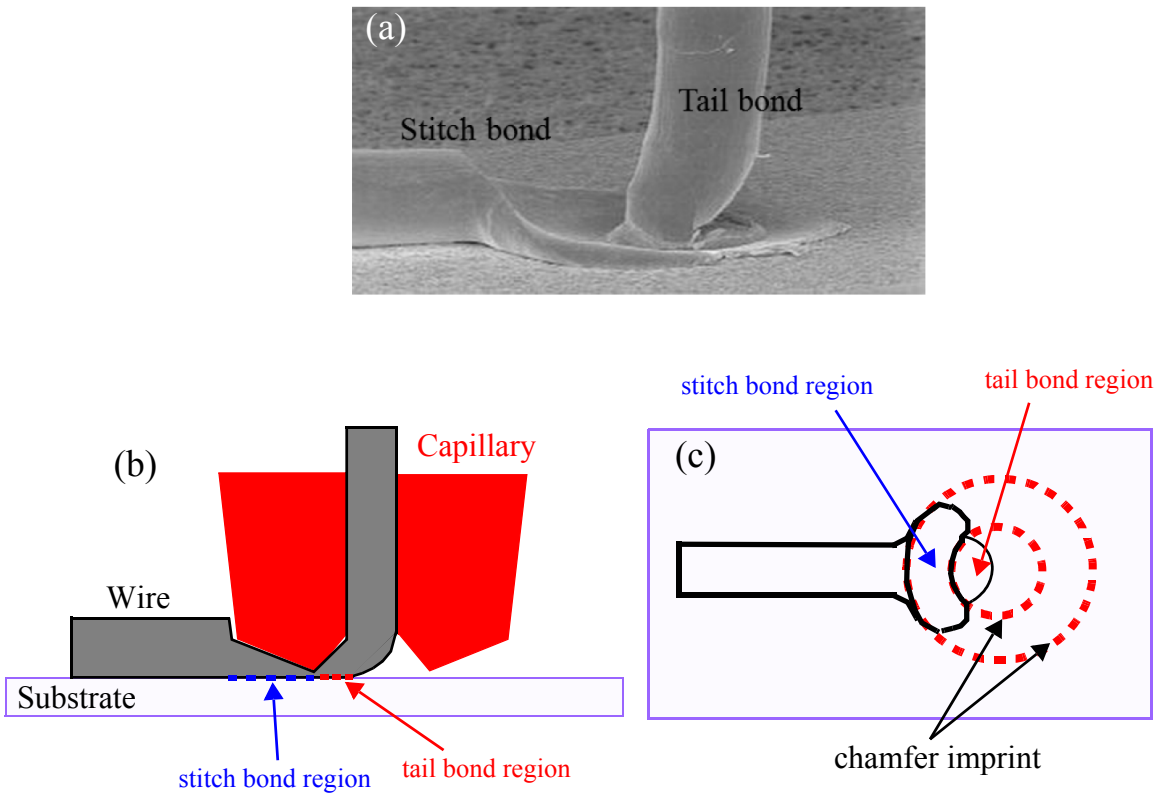

Fig. 4 (a) SEM image of stitch bond with tail bond still attached [12]. 2D side view schematic picture of stitch bond and tail bond (b) side view, and (c) top view.

1•3 Wire Bonding Trends and Challenges

Today, the majority of the interconnections (up to 85%) in the microelectronics packaging industry are done by ultrasonic wire bonding. The general trend in the wire bonding industry is toward reducing manufacturing cost, improving the performance, reducing package sizes, and increasing the I/O number of devices. This resulted in developing smaller diameter wires, new materials for wire/pad/substrate, and new processes [1,2].

The conventional wire material used in ultrasonic wire bonding is Au. Recently, Cu wire is replacing the Au wire mainly due to its much lower cost but also due to its superior electrical, thermal, and mechanical properties. It is also shown that Cu wire bonds have a better long term reliability [33].

However, there are two challenges for replacing the Cu wire with Au wire. Cu is harder than Au and has a stronger strain hardening effect during plastic deformation. This leads to an increased level of stress in the silicon chip underpad materials (silicon and low-k dielectric materials) during ball bond formation, which can lead to severe cracks that result in the chipping off of chunks of Silicon from the bond pad, called cratering. In addition, Cu wire has a high tendency for oxidation compared to Au. Oxidation degrades bondability, especially on the stitch bond side. Coating with insulation materials or protective metals such as Pd has shown to be effective in fixing the oxidation issue [27-32]. However, a careful process optimization is always required to avoid non-sticking and tail lifting issues with Cu wire [33].

In general, the understanding of the process mechanisms in wire bonding is still incomplete particularly for the stitch bond side. For example, what are the root causes (mechanisms) which make a specific set of process parameters more bondable and more repeatable? Why and how exactly does a thicker/thinner, rougher/smoother, or hotter/colder substrate influence bonding? What types of capillary surfaces (geometry, roughness, etc.) are more beneficial for bonding? Answers to these questions are helpful to enhance the stitch bond process so it can meet the future challenges.

So far, most attempts to understand the effects of process parameters, materials, and geometries on the stitch bond and tail bond relied on experimental process optimization. For example for the processes that contain bond force and ultrasound as process parameters, reducing

optimized bond force, improves the tail breaking force without significant influence on the pull force [35]. Another example of an experimental observation is that the stitch bond process is usually improved especially with respect to tail breaking force if Pd coated Cu wire replaces the bare Cu wire [34, 36]. Another example of an experimental observation is that normally rougher surface capillaries improves the stitch bond process compared to smoother capillary surfaces [37-39]. However, the main root causes and mechanisms leading to different experimental observations are still unclear. Hence, a deeper understanding of the mechanisms during stitch bonding would be beneficial to find out why particular materials, geometries, process parameters, or substrate surfaces and thicknesses improve the stitch bond process. This would help not only to improve the current processes, but also to predict new generations of materials, tools, and processes.

1•4 Objectives

This thesis aims to improve the understanding of the stitch bond process. Both experimental and numerical (finite element analysis) approaches are employed to address the main objectives of this research, which are

1. To understand the effect of stitch bonding process parameters (bond force, vibrational motions, etc.) on stitch bond quality.
2. To identify correlations between experimental data and the numerical model responses.

These objectives are pursued with the following experimental and numerical example systems. The wires used are 18 µm diameter Pd-coated Cu (PCC) and Cu wires, and the substrates are low and high bondability QFN, respectively. QFN samples are typically bonded without ultrasound due to their resonance and sensitivity to ultrasonic vibration frequency. Therefore, the process excludes the application of ultrasonic vibration, while compensating for it with lower frequency XY motions.

For the numerical model of the non-ultrasound stitch bond process, the ABAQUS^{TM} (SIMULIA, Providence, Rhode Island, United States) finite element analysis (FE) software is used. Incomplete pieces of substrate, wire, and capillary constitute the model. The bonding

input parameters includes bonding force, low frequency cyclic XY motion (scrub), and non-cyclic XY motion (skid).

1•5 Thesis Structure

In chapter 2, the process parameters, process evaluations, mechanisms, and theories are discussed. In addition, a literature study is provided about the QFN substrates and their sensitivity to ultrasonic vibration.

In chapter 3, the experimental non-ultrasonic stitch bonding process of 18 µm PCC wire is discussed. The process responses, and interactions are shown and discussed. The effect of process parameters including bonding force and low frequency XY motions on process responses (non-sticking, sticking, tail lifting, stitch bond pull force, tail bond pull force) is shown.

In chapter 4, the development of the FE analysis of non ultrasonic stitch bond process through using ABAQUS software is discussed. The model parts, geometries, loads, boundary conditions, meshes, and etc. are the subject of this chapter. All the detailed steps used to develop the model is shown and discussed.

In chapter 5, the numerical model results are shown. The detailed methods used to extract the model responses together with the required codes are discussed. The process of selecting candidate responses, and their correlation with the experimental observation are discussed in detail.

Finally, in chapter 6 the main conclusions of the current work (experimental and numerical) are given. In addition, an outlook on possible future work is presented.

2 Literature Review

In this chapter, a literature survey about the stitch bonding will be discussed. It will include an introduction to the process parameters and their effects on the bonding, and process development. The methods of evaluation of stitch bond quality will be discussed. Some existing bonding mechanisms such as ultrasonic bonding and solid state cold welding will be provided. In addition, example previous works on the numerical analysis of wire bonding processes will be shown and discussed.

2•1 Process Development

2•1•1 Process Parameters

The stitch bond, known as wedge bond or second bond, is basically a solid state joint between metallic wire and metallic substrate. A side view of a typical stitch bond process is illustrated in three steps in Figs. 5 (a) - (c). A top view illustration and SEM image is shown in Fig. 5 (d). A 3D view SEM image with the stitch bond subcomponents is shown in Fig. 6. Stitch bonds

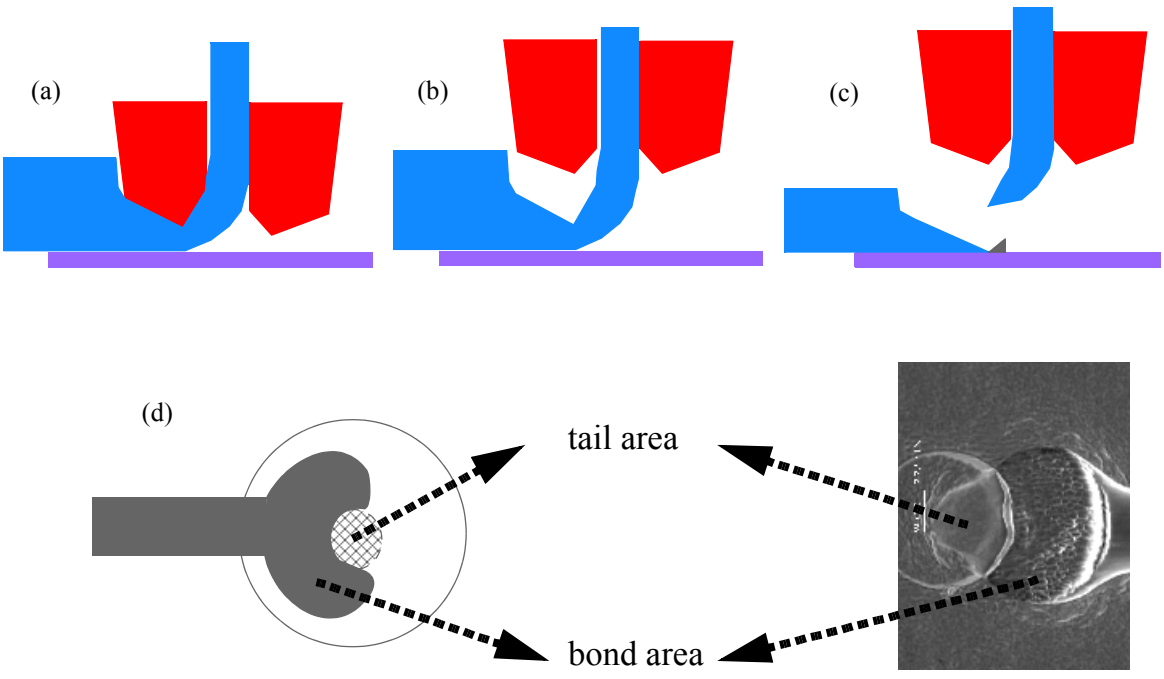

Fig. 5 Stitch bond process description. (a) capillary descends and forms the bond (b) capillary raises and clamp opens until the tail height is reached (c) clamps closes and breaks the tail (d) schematic and SEM images of the stitch bond and tail areas.

are created by simultaneous action of normal force (compression) and horizontal movement of capillary tip due to the ultrasonics or low frequency vibrations (motions). Simultaneously, a small crescent area is also formed which is called tail bond (Fig. 5). After the stitch bond formation, the capillary rises up to a certain height, then the capillary movement stops, the wire gets clamped, the capillary moves up again, and pulls up the wire to break the tail bond. This results in a new tail protruding from the capillary tip. This tail can now be used for the next FAB. If the tail bond is not strong enough, it breaks during the capillary upward movement and there will be no or a too short wire tail for the next FAB ("tail lift" problem). If the tail bond is too strong, it causes excessive tension in the wire before it breaks, resulting in a snap back effect and permanent bends form in the wire next to the clamp position [40]. Therefore, an intermediate bond strength(e.g. 1 gf for 18 µm Cu wire) is required for the tail bond, while a high bond strength is desired for the wedge bond. In addition to the tail lifting issue, there is another problem that could be observed with the tail area, called "peeling". Peeling can happen if the tail area is strong itself but the adjacent wedge area is not strong enough. Therefore during tail breaking, part of the wedge close to tail area peels up (pops up), and result in unreliable stitch bond. Comparison of a peeled stitch with a one that contains no peeling is shown in Fig. 7.

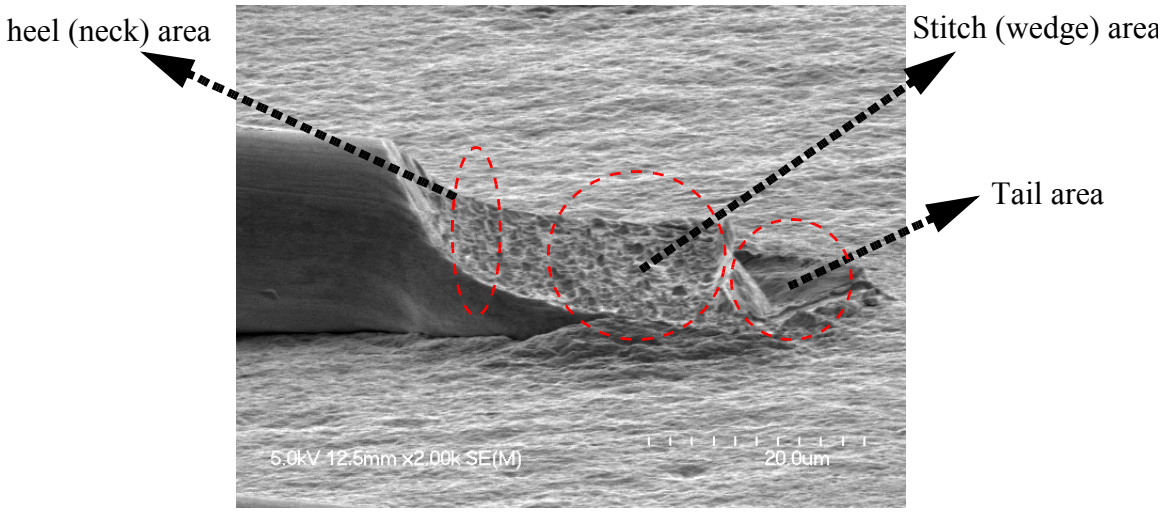

Fig. 6 A typical SEM image of bonded stitch bond with the corresponding subcomponents. The wire is 20 µm PCC and the substrate is Ag-plated Cu QFP (Quad flat

In order to achieve a high quality process, the process parameters, materials, and tools need to be optimized. Normally, the interaction between parameters make the optimization difficult. The following paragraphs give more details about the main process parameters.

Normal force is applied in the form of impact force and bond force. The normal force level needed in the process depends on the mechanical properties of the wire and the geometry of the capillary tip. Different capillary designs (mainly with different face angles, FA) influence the way in which force is acting on the wire. Basically the sharper the tip (i.e. the larger the FA), the lower the force needed for achieving a defined amount of deformation [2, 4].

Ultrasonic vibration enables a horizontal movement of the capillary tip with a certain frequency (typically around 120 kHz) and a programmable amplitude. The ultrasound generates an oscillating force acting onto the wire to overcome the static friction at the bond interface. It can cause local heating due to sliding friction that enhances the interdiffusion of metals and bonding. Ultrasound vibration oscillates in only one direction ("North-South direction"), so the wire loop direction influences the amount of the ultrasonic effect. In many processes, ultrasound acts more efficient onto wires in "North-South" direction and less efficient to wires in "East-West" direction which require a high ultrasound level for compensation. Figure. 8 shows the different directions in the ultrasonic wire bonding [4].

For most wire bonding machines , the bonding time parameter is defined as the duration of application of ultrasonic movement. Up to a certain level, increasing bond time enhances the metallurgical bond, up to a maximum duration after which the bond is completed. For too long bonding times, it starts to deteriorate due to the effect of ultrasonic fatigue. It is always preferred to set the bonding time as low as possible to increase the process speed.

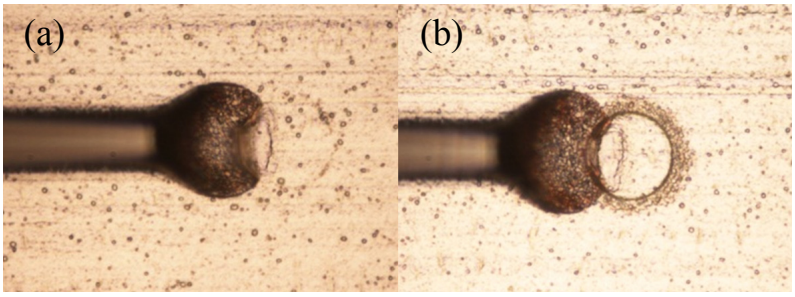

Fig. 7 Stitch bond peeling failure (a) stitch bond with peeling and (b) with no peeling. T wire diameter is 18 µm.

Increasing bonding temperature enhances the diffusion process and thus the bonding quality. It also increases the deformability of the wire. However, too high temperature can result in excessive wire deformation (overbonding) and inaccuracy in placement of the bond positions.

2•1•2 Process Evaluation

Pull Test: A pull test is usually performed to investigate the quality of wire bonds, mainly the stitch bonds. The pull test includes placing of a hook under the wire loop and lifting the hook up until the failure/break of wire while recording the maximum pull force value during breakage. The test schematic is presented in Fig. 9. Pull test is designed to provide a quantitative evaluation of the degree of the adhesion of the stitch bond to the substrate. However, it does not contribute to the long-term stability of the stitch bonds directly, since the long-term stability is a metallurgical issue rather than a mechanical issue. For most cases, the stitch bonds do not need to withstand severe forces (maximum force or stress they could see actually happens during molding). To compare the stitch bond pull force of the stitch bonds accurately, the wire bonding loop length and height and also the position of the pull test hook should remain identical (preferably at the center of the loop for the pull test hook position).

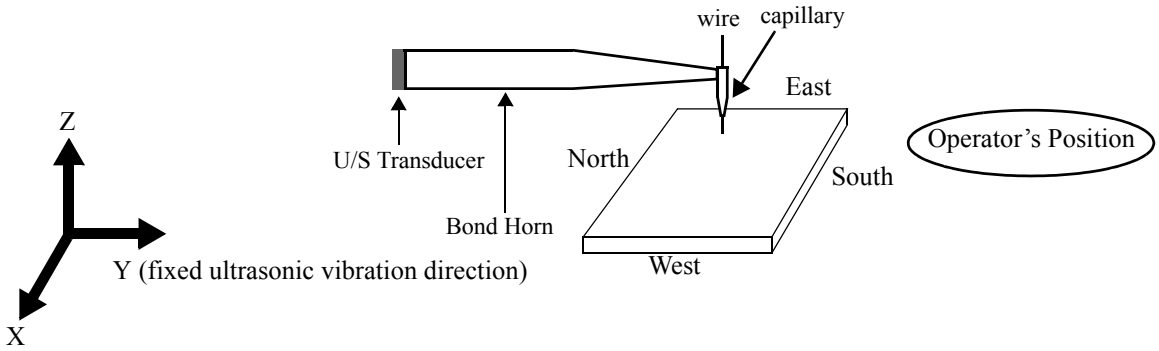

Fig. 8 Different directions in ultrasonic wire bonding.

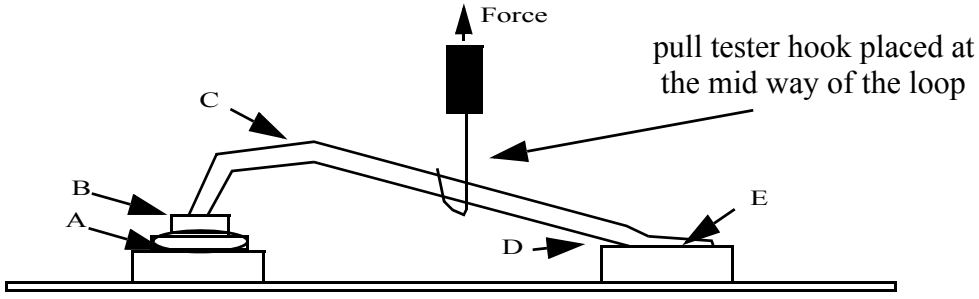

Fig. 9 Pull test description [41,42].

Different failure modes can happen during a pull test, as reported in pull test standards such as MIL-STD-883G [41,42]. They include ball lift (type A), ball neck break (type B), mid span break (type C), heel crack of stitch bond (type D) and stitch lift (type E). The most desirable failure mode is type C and it results in highest pull strength. It is indicative of a good quality ball bond and stitch bond, and the failure is because of the ductile fracture of wire. Type D happens if there is a thin and damaged heel area in the stitch bond. Severe bonding parameters can result into such condition. A failure type E is indicative of a not optimized stitch bond process.

Tail Breaking Test: A tail breaking test is a test that evaluates the strength of the tail bond. It is important to find parameters that result into high enough tail strength which consequently result in a more robust process. Tail breaking test can be performed by some wire bonder machines using the force signals during the stitch bond process. In some K&S wire bonders the tail breaking force measurement uses an internal force signal and is evaluated automatically during the process by the machine software "tail pull force" [43]. In contrast, on an ESEC 3100 wire bonder, the tail breaking force procedure is not automated. During tail breaking, the machine's force and z-position signals are extracted into a data file and later analyzed off-line by a custom evaluation program [43]. Typical machine signals used for tail breaking force are shown in Fig. 10 [44-51]. Moreover, due to the limited time resolution of the recorded signals, the ESEC 3100 off-line method requires the tail breaking procedure to be slowed down to durations between 50 ms to 100 ms.

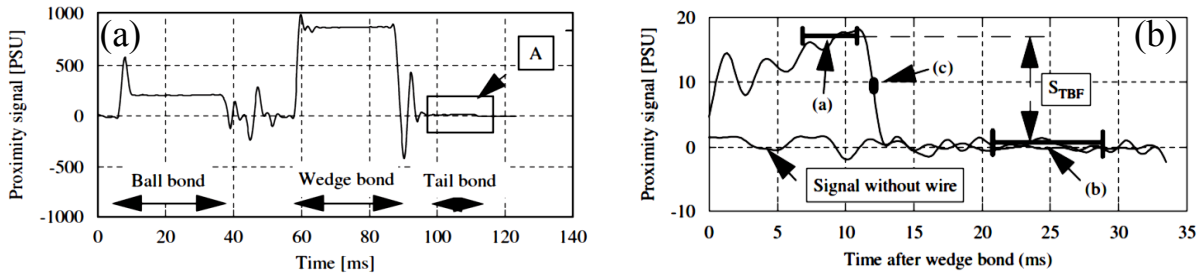

Fig. 10 Machine signals use for tail breaking force measurement test [44]. (a) proximity sensor force signal during different stages of stitch bond process, (b) zoom of the force signals during tail breaking segment.

2•2 Process Mechanisms

Up to now, several approaches have been attempted to improve the stitch bondability. They include optimizing stitch bond process parameters, improving the surface quality of the substrate, and improving the geometry/surface of capillary tool. Below, some of the previous studies are reviewed.

2•2•1 Effect of Process Parameters

In an early study Fujmioto and Nakata [52] worked on the effect of process parameters on stitch bondability of bare Cu wire on Cu substrate. They studied the influence of force and ultrasonic vibration on the amount of wire deformation, pull force, and failure mode during the pull test. They showed that increasing normal force or ultrasonic vibration duration, increase the amount of wire deformation, and in addition, increase the pull force up to a certain level, but beyond a limit of force or ultrasound, pull force starts to decrease. The onset of decrease in pull force is normally due to the transition in failure mode from interfacial break to wire heel (neck) break (Figs. 11 and 12). They report that by adjusting the normal force and ultrasonic vibration duration, it is possible to achieve bonds with same amount of deformation, but different pull force/failure mode (Fig. 13). They concluded that even though the wire

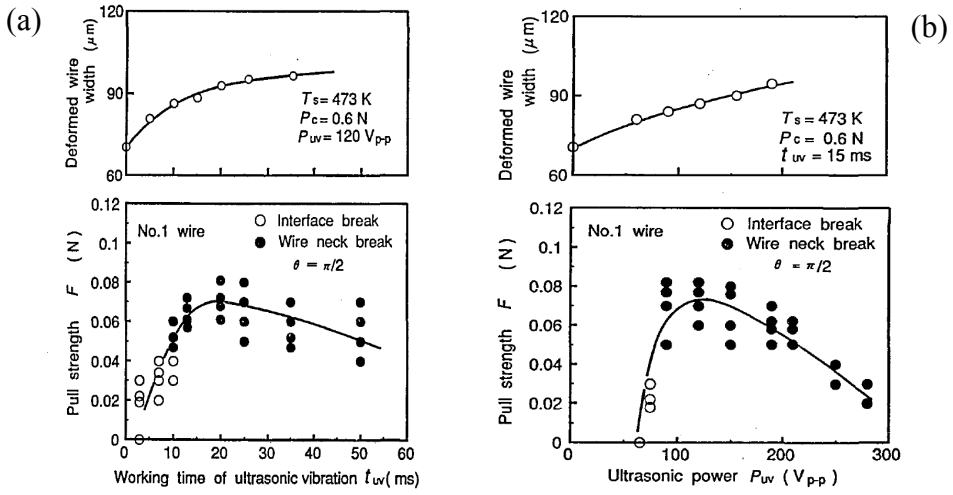

Fig. 11 Effect of ultrasonic energy on wire deformability and stitch bond pull strength (a) ultrasonic energy power (b) ultrasonic energy duration [53].

deformation and pull force are related to each other, the absolute value of deformation does not determine the final bondability/strength.

In their second work [53], they developed a two-step load (bond force) pattern (profile) instead of a one-step loading. They used a high load P_1 followed by a lower load of P_2. The ultrasonic vibration is applied at the beginning of the 2nd loading. The schematic of their loading is presented in Fig. 14. They observed that if a two-step load is used, higher pull strength is achieved. It has been concluded that in a one-step process, some of the ultrasonic energy is consumed for wire deformation, while in a two-step process, the contact area is already large

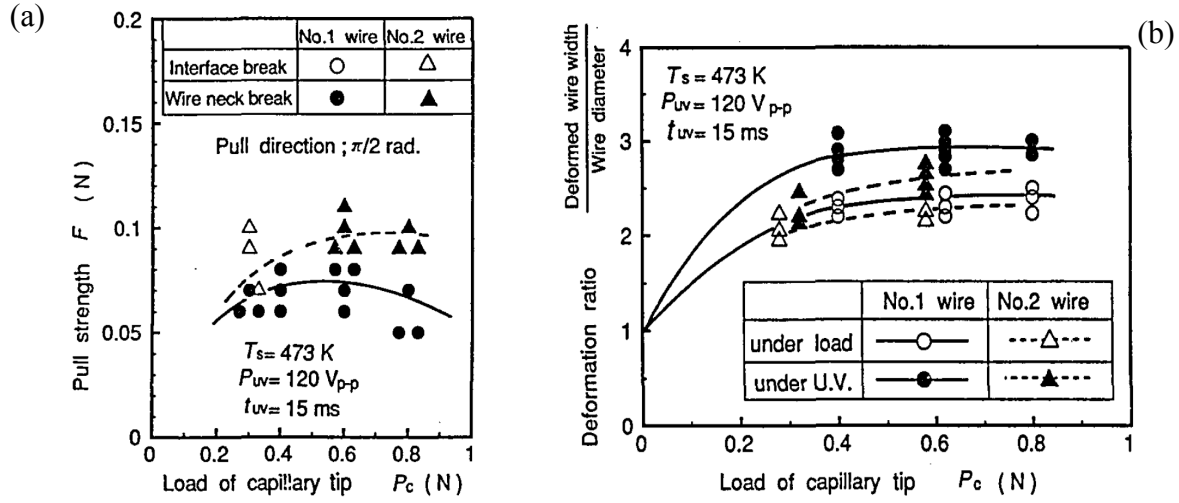

Fig. 12 Effect of bond force (load of capillary tip) on (a) stitch pull strength and (b) wire deformability. U. V. stands for ultrasonic vibration [53]. When the wire "under load" it means there is no U.V.

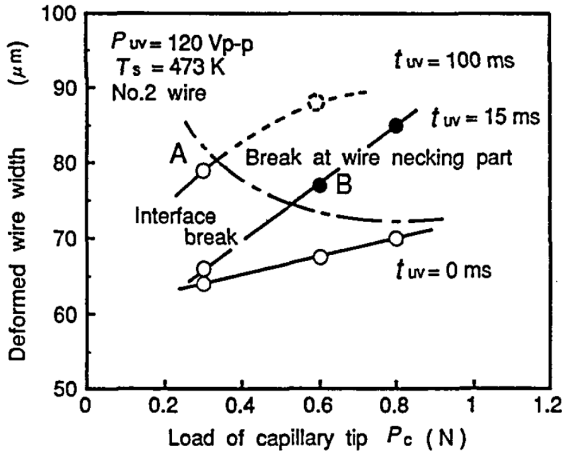

Fig. 13 Relationship between wire deformation and bondability [52].

after the impact segment, and then a higher portion of ultrasonic energy contributes to bonding. It is illustrated in Figs. 15 and 16.

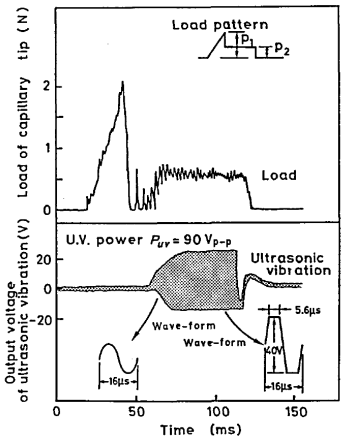

Fig. 14 Two step process description [53].

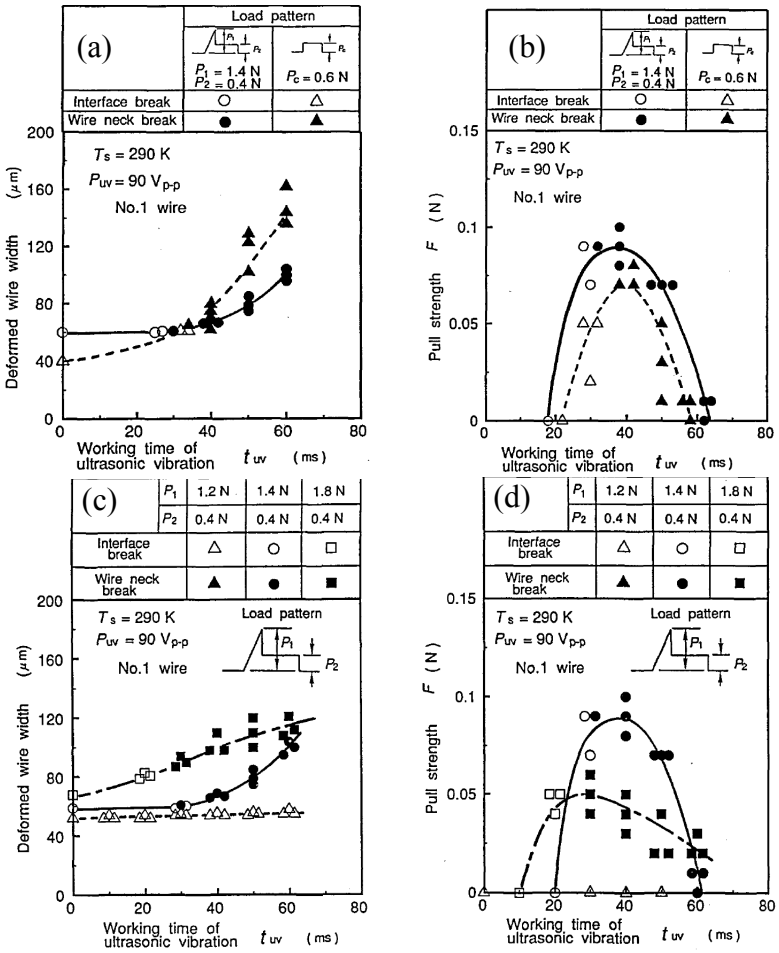

Fig. 15 Two step process proposed by Fujimoto. Effect of ultrasonic energy is investigated at different loading patterns. Effect of ultrasonic energy at $P_1 = 1.4$ N and $P_2 = 0.4$ N on (a) wire deformation, and (b) pull strength. Effect of ultrasonic energy at 3 different loading patterns on (c) wire deformation, and (d) pull strength [53].

In another study done by Li et al., the effects of bond force and bond ultrasound was investigated during the wedge-wedge bonding process. Wedge bonds were formed by different parameters and then etched away to reveal the interface [54]. In Figs. 17 and 18, interface evolution is shown upon increasing bonding force and ultrasonic energy application time, respectively. They concluded that with increasing ultrasonic energy (time), the real joined area increases until the entire area is bonded. However, increasing the bond force, increases the size of a non-bonded area at the central region of the interface. The schematic effect of bonding force and ultrasound on interface evolution is shown in Fig. 19.

In an optimization study done by Lee et al. [44], the tail breaking force was measured for Cu wire and optimized. For optimization, an iterative approach considering parameters of impact force (IF), bond force (BF), and ultrasonic energy (US) was used. Results showed that itera-

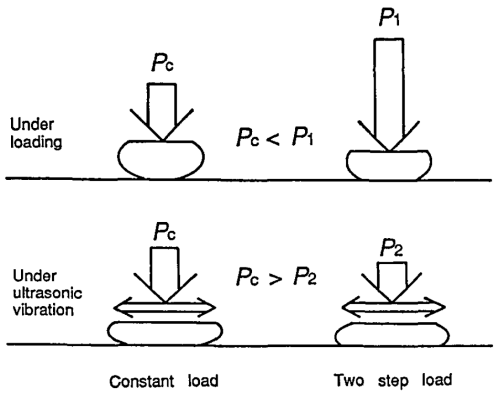

Fig. 16 Schematic description of the bonding mechanisms during one-step and two-step processes [53].

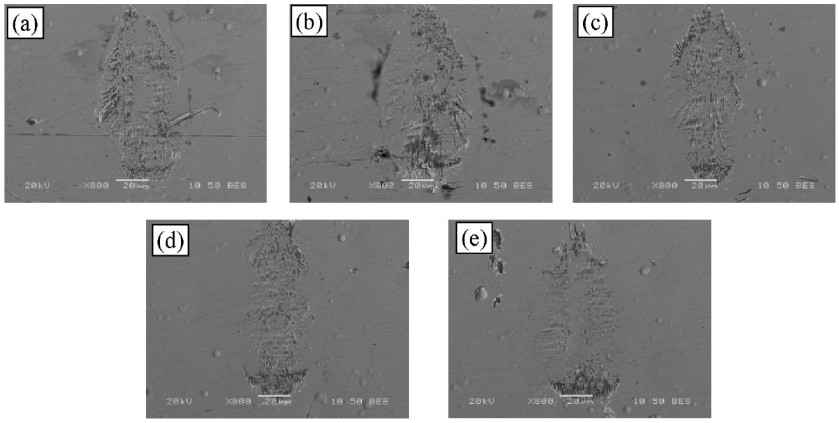

Fig. 17 Evolution of bond interface with increasing bond force. (a) 40, (b) 80, (c) 120, (d) 160, and (e) 200 gf [54].

tive method is strong to find a parameter combination which result in highest TBF. An example results of the fourth iteration is shown in Fig. 20.

In a second optimization study of Lee et al. [55], a DOE type of optimization was studied. They emphasized the importance of concurrent (simultaneous) optimization of both stitch bond pull strength and tail pull strength. Separate process windows were found for stitch pull force (PF) and tail breaking force (TBF). The quality of the process was measured by process capability index (Cpk), as a function of bond force and bond ultrasound. Then the individual process windows were overlapped and optimized process window with maximum PF and TBF found. The overlapped process window is shown in Fig. 21.

Tian et al. [56], studied the bonding mechanism of ultrasonic wedge-wedge bonding of copper wire on Au/Ni/Cu substrate at room temperature. They varied the ultrasonic energy level and

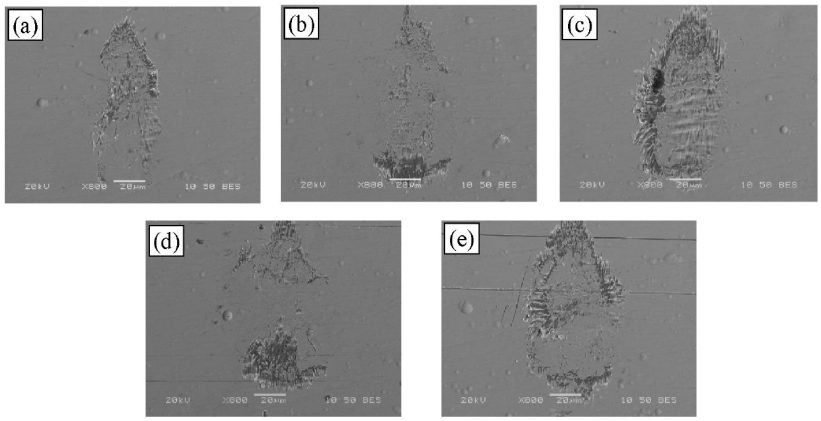

Fig. 18 Evolution of bond interface with increasing of bonding time. (a) 40, (b) 80, (c) 120, (d) 160, and (e) 200 ms [54].

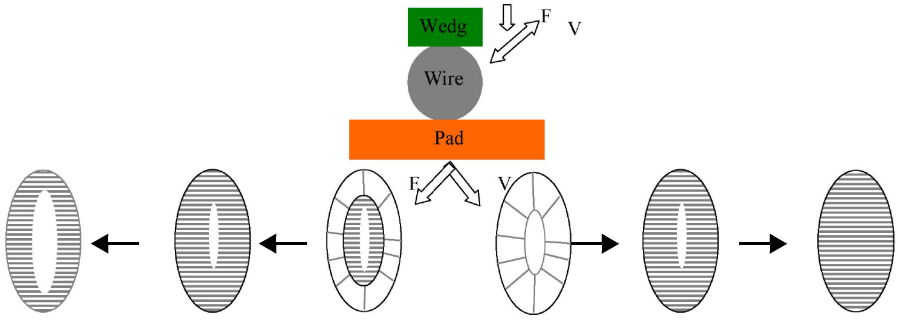

Fig. 19 Schematic picture describing the effect of bond force (F) and ultrasonic energy (V) on interface evolution [54].

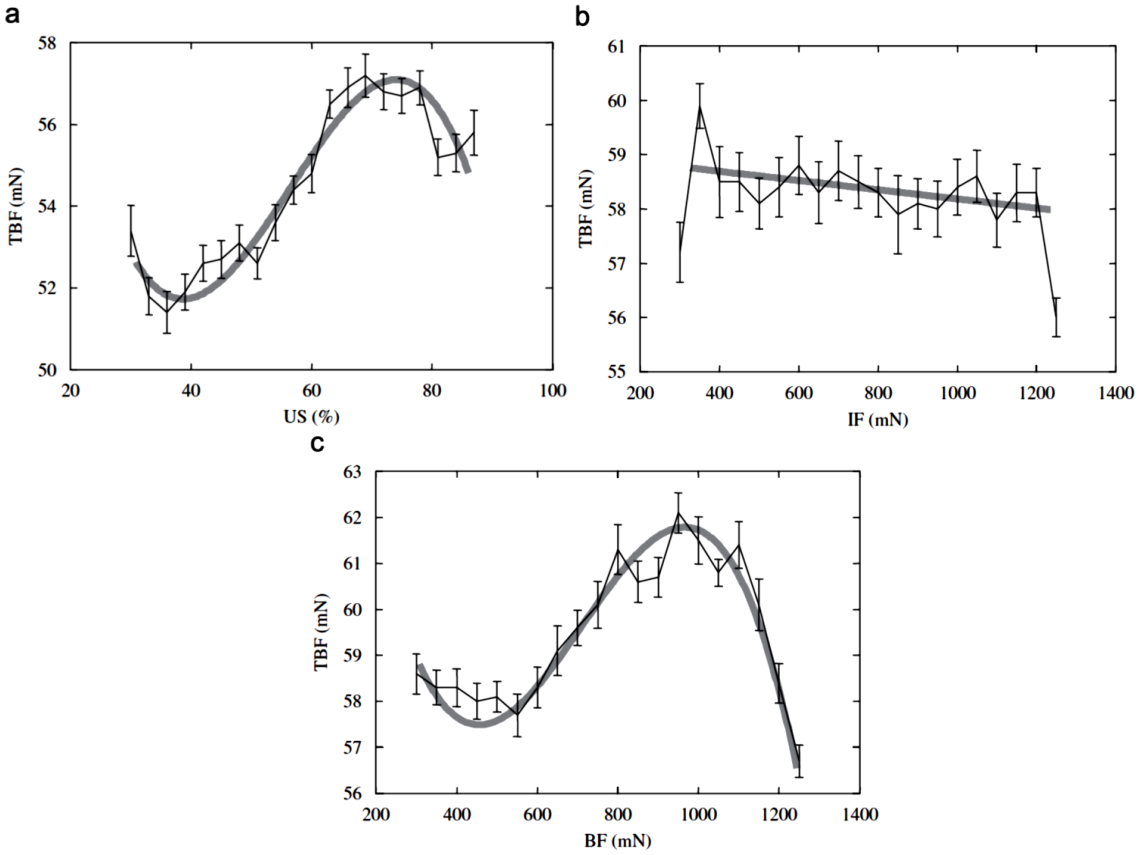

Fig. 20 The fourth iteration results of Au wire TBF: (a) US, (b) IF, and (c) BF. Gray lines are polynomial fits [44].

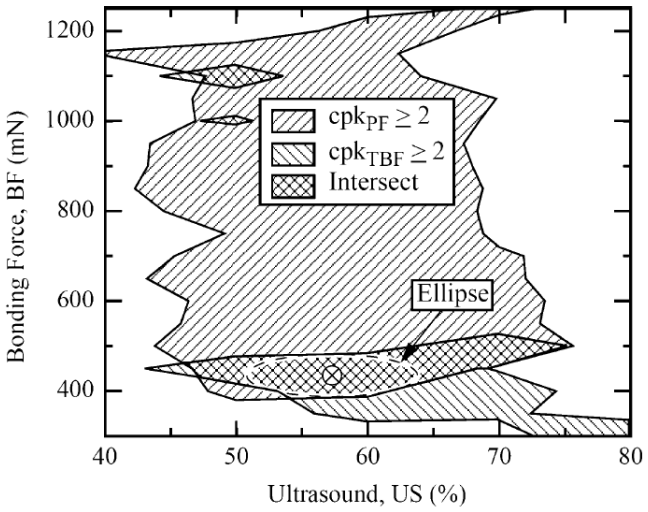

Fig. 21 Overlapping the process windows of PF and TBF to find the optimized parameters [55].

studied its influence on the quality of the wedge bond. Their results showed that by increasing ultrasonic energy, the failure mode of the bond evolves from interfacial break to neck break, and finally to bond break. The neck break failure mode showed the highest pull strength value as shown in Fig. 22 (a). They suggested that as the inter-diffusion between Au and Cu is very weak at the room temperature, the bond formation is induced by wear action and mechanical mixing. The ultrasonic power contributed to increase the deformability of the Cu wire. However further deformation induced the strain hardening of Cu as shown in Fig. 22 (b).

2•2•2 Interface of Stitch (Wedge) Bonds at Atomic Level

Several studies have been done to understand the wedge bond interface formation at atomic level. Many of them are done by using transmission electron microscopy (TEM), to reveal the atomic structure of the interface.

Geissler et al. [57] studied the interface formation between AlSi wire and Au substrate. They observed that ultrasonic energy quickly initiates the bond formation by formation of Au_8Al_3 inter-metallic compound at the interface. It is shown in Fig. 23. Their FE study showed that the maximum temperature at the interface does not reach values higher than 100 °C, so they concluded that the formation of inter-metallic compound is activated not by heat, but by an increased density of vacancies induced by ultrasonic vibration. In contrast, Ji et al. [58] studied the same process with the high resolution TEM. They observed high density of twin crys-

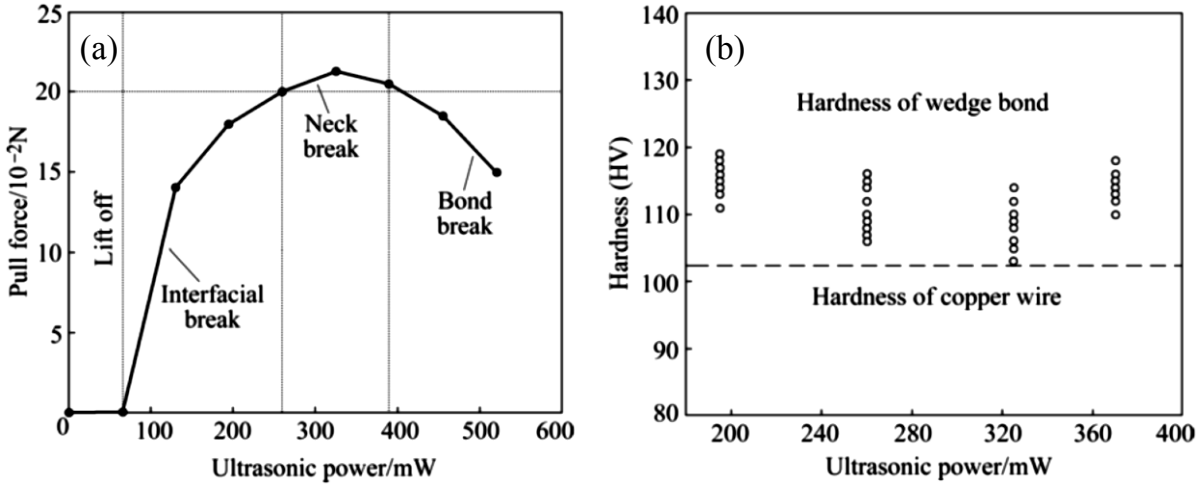

Fig. 22 Effect of ultrasonic energy on wedge bond's quality (a) pull strength (b) wedge bond's micro-hardness [56].

tals at Au-Al interface. They mentioned that rather than a vacancy interdiffusion induced by ultrasonic energy, ultrasonic vibration could activate the twin crystals formation at relatively low temperature which provide fast diffusion paths and enables the metallurgical adhesion. Their suggested schematic of a wedge bond is shown in Fig. 24.

Liu et al. [59] studied the interface of Pd-coated Cu wire stitch bonds on Ag plated lead frames. The topography of the stitch bond interface and the electron micro-diffraction pattern are shown in Figs. 25 (a) and (b). They observed that due to the protective nature of the Pd layer on the Cu wire, no oxide layer forms at the interface. The Pd coating gets extensively deformed, reaching only 30 nm thickness. The EDX results showed that there is a sharp

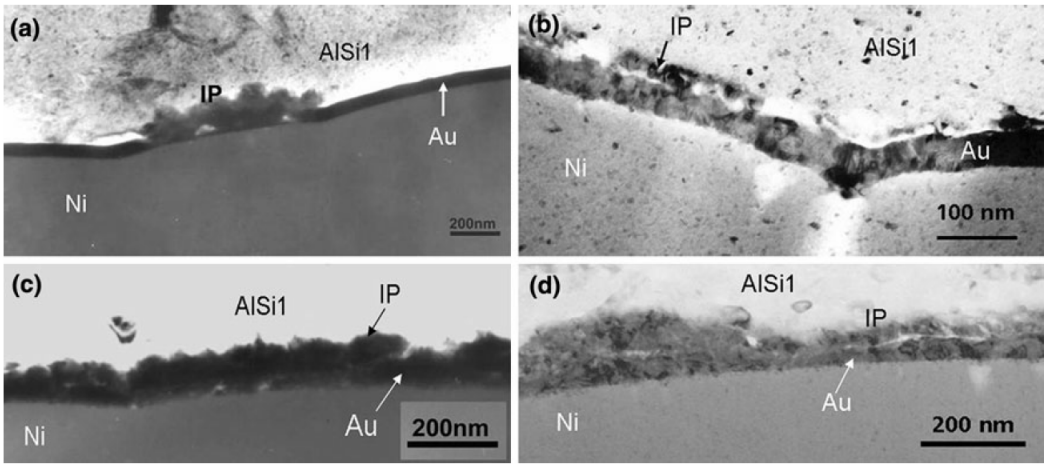

Fig. 23 Growth of Au_8Al_3 intermetallic phase during the wire-bonding process, after bonding times of (a) 7 ms, (b) 15 ms, (c) 22 ms, and (d) 50 ms [57].

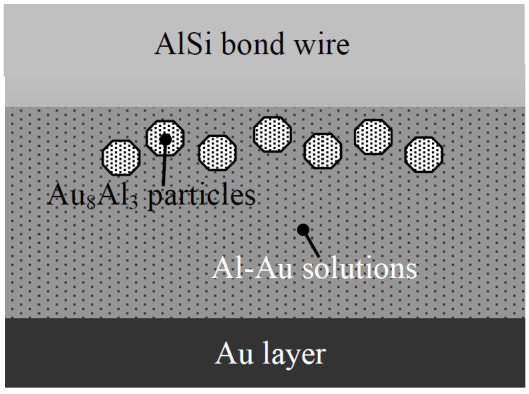

Fig. 24 Schematic of the constitutes of the wedge bond interface showing the Au_8Al_3 particles in an Al-Au matrix [58].

change in element composition of either Cu or Al, thus revealing a very narrow interdiffusion layer.

2•2•3 Effect of Substrate Surface Condition

In another work done by Fujimoto et al. [53], the effects of surface roughness and surface oxidation on pull strength of Cu wire stitch bonds are studied. They bonded Cu wire to different substrates containing various degrees of surface roughnesses R_{max}. Increasing the roughness of the substrate decreases the adhesion of wire to substrate, i.e. drops the pull strength if the same process parameters are used. They concluded that a high surface roughness results in a weak contact between wire and substrate as shown in Fig. 26 (a). The effect of substrate surface oxidation was investigated by holding the substrate at different temperatures before bonding. Figure 26 (b) shows the effect temperature and holding time on pull strength. It is shown that increasing the temperature and holding time degraded the pull strength. They mentioned that the oxidation of the substrate surface is the main reason of the degradation. The oxide layer is known as a barrier to the close contact of the metals, degrading the adhesion. Recently a new study done by Hu et al. [60] showed the effect of surface roughness on the stitch bondability with Au wire. Up to a certain roughness level (0.4 - 0.7 μm) increasing the roughness enhances the stitch pull force, but further increase in the roughness reduces the stitch pull force. The increase in the stitch pull force is related to an enhanced physical interlock between the Au wire and the microcones (rough features).

(a)

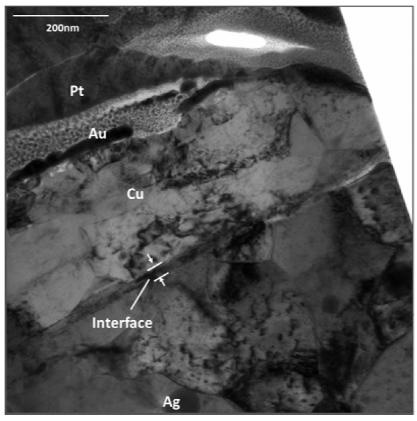

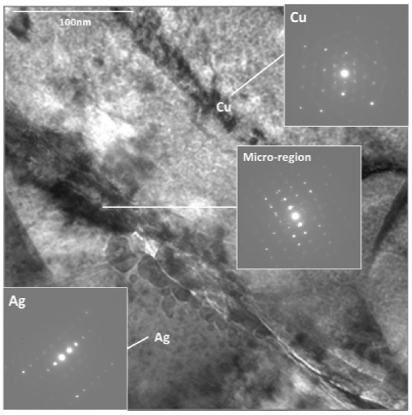

(b)

Fig. 25 Pd Coated Cu - Ag plated substrate bond interface (a) Sample topography (b) Electron micro-diffraction at pattern at interface [59].

Several attempts have been made to describe the of cleanliness of the bonding surface on the substrate. It was assumed that a cleaner surface is capable of enhancing the bondability. Methods such as plasma cleaning [61] or elemental contamination removal by chemical solutions [62] proved the effectiveness of cleaning methods to enhance the bondability. In a Au wire - Au substrate bonding system, plasma cleaning is capable of removing elemental surface contaminations such as C, O, Cu, and Ni. It is believed that oxides such as copper oxide and nickel oxide can form and degrade the bondability. The amount of such oxide is decreased by plasma cleaning process.

The types of the coating elements presented on the substrate surface, and their layer thicknesses are believed to be influencing the bondability. For example in [63] a study is reported of the effect of different surface finishes on the stitch bondability of Cu wire. This study showed that two different substrate types result in acceptable bondability and cost with Cu wire. Those two substrate are electro-less nickel/electro-less palladium (ENEP) with a pure Pd deposit, and electro-less pure Pd directly over copper. They concluded that if the bonding layer is thinner or harder, the deformation/bonding area is smaller, leading to reduced bondability and poor tail bond that consequently results in higher number of process stoppage as shown in Fig. 27.

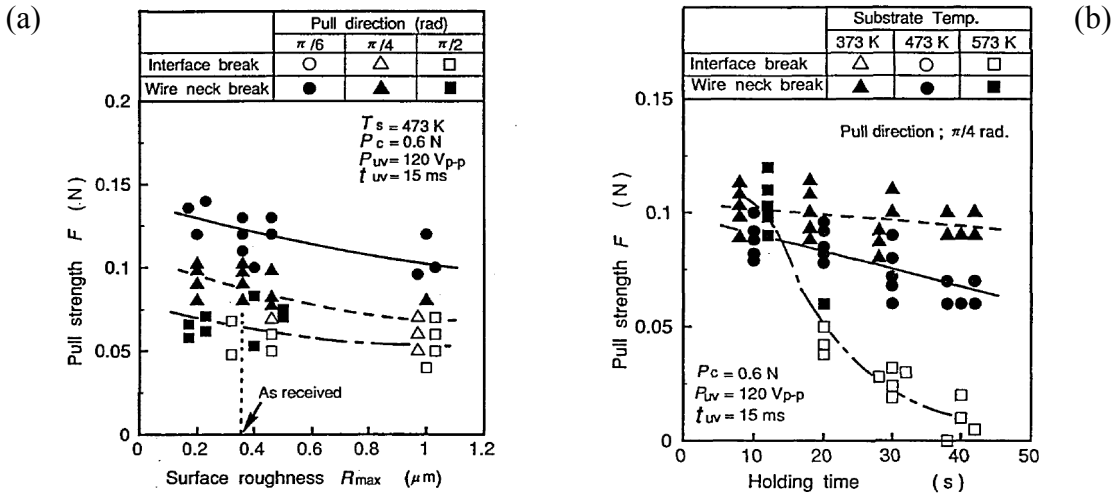

Fig. 26 Effect of (a) surface roughness and (b) temperature on Cu stitch pull strength [53].

2•2•4 Effect of Capillary Design

In general, the tip diameter greatly influences the pull force of the wedge bond. The larger the diameter, the stronger the pull force [64]. In [65, 66], it has been shown that the capillary tool design could affect the stitch bond process. Not only the capillary tip geometry, the capillary surface finish is also important. It is shown that the capillaries with rougher surface improve the stitch bond quality, especially for Cu wire. The improvement is attributed to a better coupling effect and less slipping between wire and capillary.

2•2•5 Contact Mechanics of the Interface (Micro-slip Theory)

Mindlin's micro-slip theory [67] describes the contact mechanics of two spheres in contact with each other with relative elastic motion and a oscillating tangential load. For a suitable set of values for normal force and amplitude of tangential oscillation the middle area stays fixed, while the periphery is slipping as shown in Fig. 28. The distribution of normal and tangential forces, $P_n(x)$ and $P_t(x)$, respectively, and the radius of the stationary area, a', are as follows:

$$P_n(x) = \frac{P_n}{2\pi a^3}(a^2 - x^2)^{\frac{1}{2}} \tag{1}$$

$$P_t(x) = \frac{P_t}{2\pi a}(a^2 - x^2)^{\frac{-1}{2}} \tag{2}$$

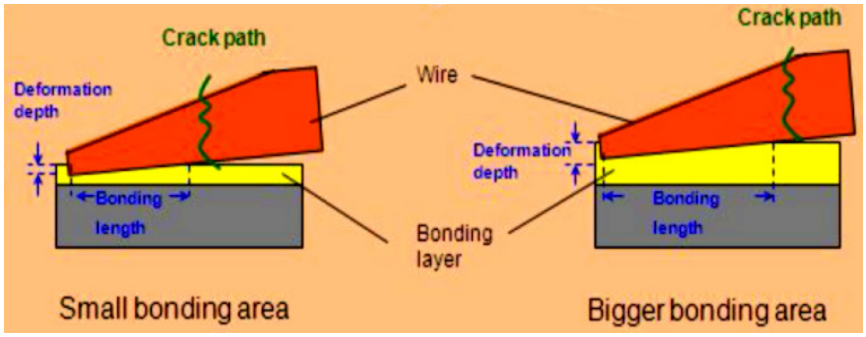

Fig. 27 Effect of substrate thickness/hardness on stitch bond area [63].

$$a' = a\left(1 - \frac{P_t}{\mu_S P_n}\right)^{\frac{1}{3}} \tag{3}$$

where $P_n\,(x)$ and $P_t\,(x)$ are the distributions of a normal and tangential forces over the contact area, respectively, x the radial coordinate from the center of the contact area, a the radius of this area, and a' is the radius of the stationary area [67]. Despite the distribution of the normal and tangential force, however, Mindlin's micro-slip does not provide any insight about the distribution of stresses at the contact directly. But this theory was a starting point for some other work toward investigating the distribution of the stresses at the contact interface. For example [68] numerical analysis to investigate the distribution of the stresses in silicon substrate as a result of the Cu to Cu ball bonding, as shown in Fig. 29.

Lum et al. [25 and 70] and Xu et al. [71] used the Mindlin's theory to investigate the effect of bond force and bond ultrasound on the ball bond process. They found that metallurgical bonding starts at the peripheral regions in the direction of ultrasound and grows toward the central region upon increasing ultrasound energy. At low forces, the bonded area contains the entire interface, even though the bond is weak. By increasing the force, an unbonded region initiates at the central region and expand towards the periphery upon increasing force. The mechanism proposed by Xu for ball bond is schematically shown in Figs. 30 and 31. Lum et al. [70] have shown similar trend for the effect of bond force and ultrasonic energy on the wedge-wedge bonding of Al on Cu. They suggested that the ultrasonic energy encourages relative motion at the interface and cleans up surface oxides which consequently facilitates bonding.

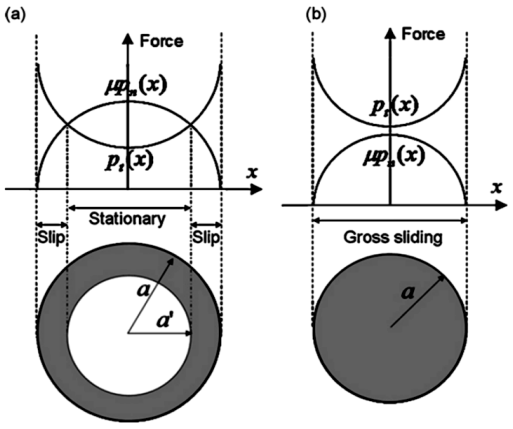

Fig. 28 (a) Microslip regions in contact of two spheres together with stationary area (b) gross sliding [70].

2•3 Ultrasonic Vibration Sensitive Substrates

Some types of the more recently developed substrates including Quad-Flat no lead (QFN) are known to be sensitive to ultrasonic vibration [15-23]. Despite the outstanding achievements brought by these new packages such as lower cost and smaller sizes, the issue with sensitivity to ultrasonic vibration has reduced the process capability of stitch bonding significantly. A

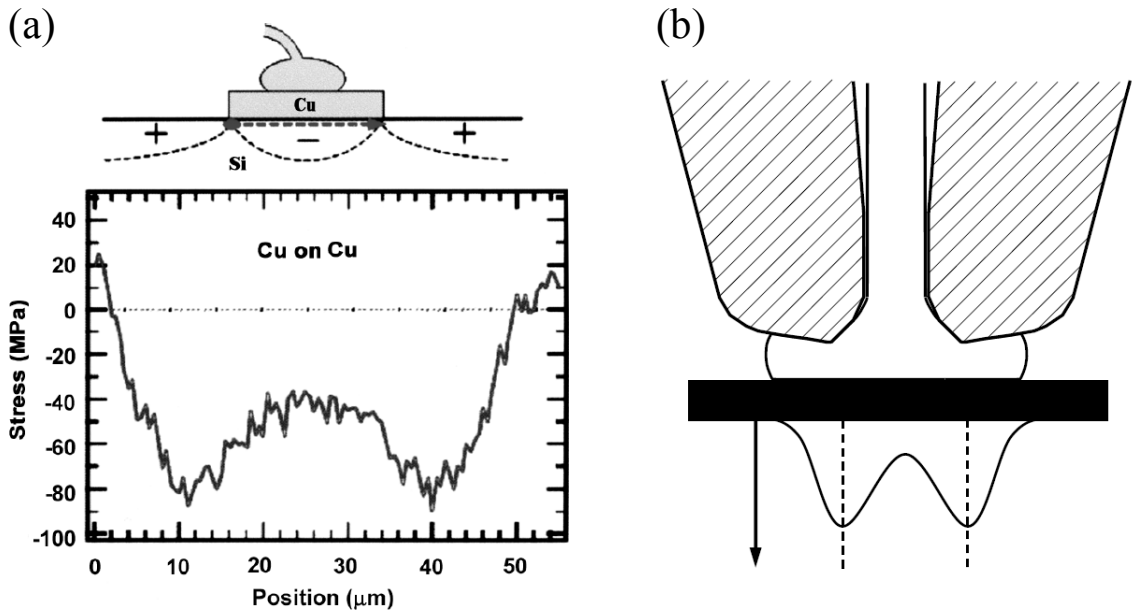

Fig. 29 (a) Distribution of stresses in the Si substrate as a result of the Cu on Cu wire bonding [68] (b) Schematic distribution of stresses underneath of a ball bond [69].

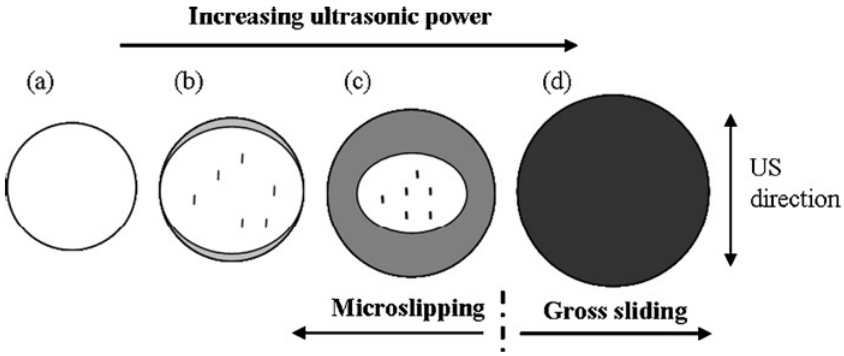

Fig. 30 Schematic evolution of bond initiation and growth by increase in ultrasonic energy (US): (a) bond initiation at the periphery of contact area (no US); (b) bond initiation at the periphery according to the direction of ultrasonic vibration; (c) growth of bonded area towards center; (d) bond completion. The stationary areas are shown by white color. The darker the bond area, the stronger the bond [70].

photograph of a QFN substrate and typical leadframe inside design are shown in Figs. 32 (a) and (b). The main cause of the sensitivity of the QFN leadframe to ultrasonic vibration is due to resonance of the leadfingers at the frequency of ultrasonic vibration (~ 120 kHz). The FE modeling results of resonance of QFN leadfingers at 138 kHz is shown in Fig. 33 (a). A typical cracked/failed stitch bond made on QFN leadfinger by means of ultrasonic vibration is shown in Fig. 33 (b).

To reduce the failed stitch bond problem occurrence with the QFN, different approaches have been attempted. They include redesigning the leadfingers to reduce the resonance at ultrasonic

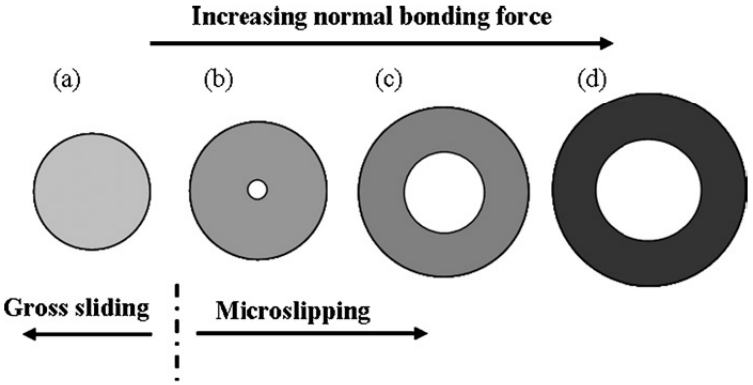

Fig. 31 Schematic illustration of bonded regions progress with increasing normal force: (a) gross sliding (b) stationary area initiation; (c) outward growth of stationary area and footprint; (d) more outward growth of stationary area and footprint, increasing bond strength.The stationary areas are shown by white color. The darker the bond area, the stronger the bond [70].

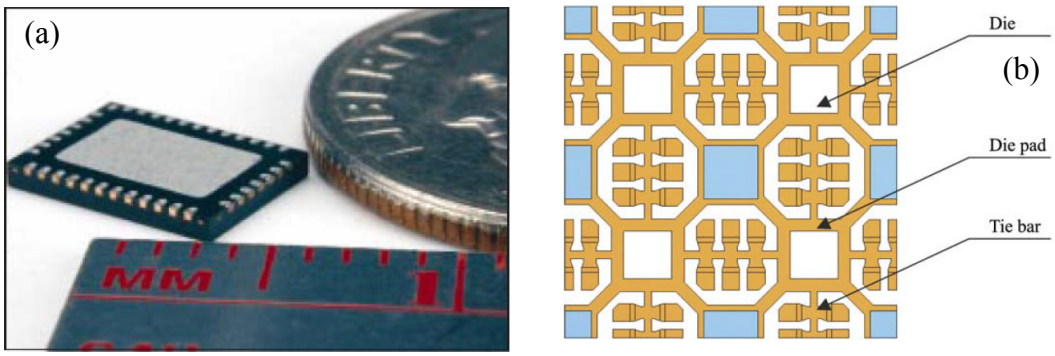

Fig. 32 (a) Micrograph of a typical QFN device [19] (b) Typical leadframe design in QFN package [18].

vibration frequencies [16,18,22,23] optimizing the process parameters with attention to use ultrasonic vibration as low as possible [15], changing the ultrasonic frequency for the stitch bond with new transducer designs [72], and finally replacing the ultrasonic vibration with low frequency machine motions such as scrub and skid [17]. Such low frequencies cannot excite the vibration modes of the QFN leadframe fingers. The leadfinger redesign and re-optimization of the process parameters approaches seem to be able to reduce the problem, however they do not provide a general solution for all different types of QFN or similar devices. The latter approach (replacing ultrasonic vibration with low frequency XY motions) is successfully used in many QFN applications but becomes more and more challenging with the smaller wire diameters required for nowadays advanced ICs. Low frequency motions are not able to provide the same amount of bonding energy as ultrasonic vibration, so a proper optimization and process knowledge is crucial for future advanced processes.

2•3•1 Low Frequency XY Motions

There are two types of low frequency XY motions that can be applied independently from each other. One of the motions is called “scrub”. Scrub is a cyclic motion with a low frequency. Scrub could be applied in different directions, including perpendicular to wire direction, in-line with the wire direction, or circular. The number of cycles and the scrub frequency can be adjusted. The typical cycle numbers is three and the typical scrub frequency is 100 Hz.

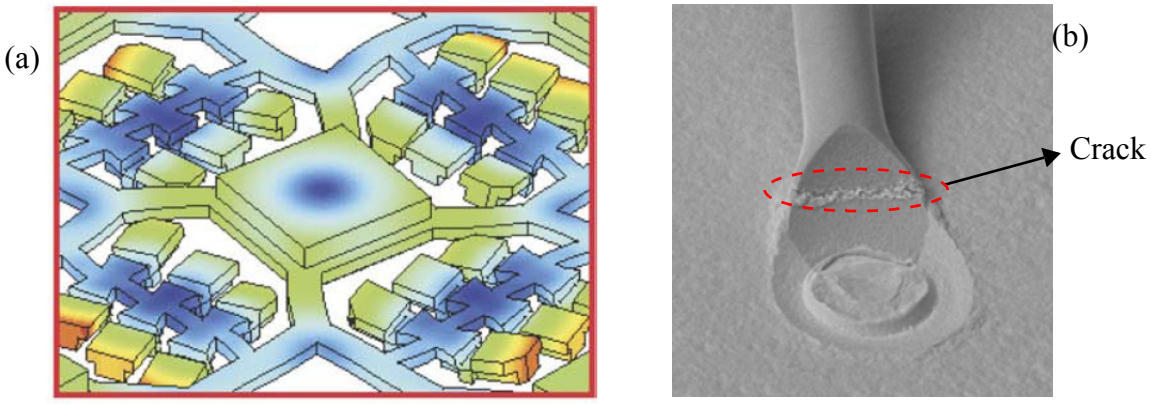

Fig. 33 (a) Position of maximum vibration from FE simulation of leadfinger resonance of QFN at 138 kHz [18] (b) SEM micrograph of a failed/cracked stitch bond made by ultrasonic vibration on QFN [23].

The other motion is called “skid”. Unlike scrub, skid is non-cyclic, and it can be only in-line with the wire direction. If it is directed towards the first (ball) bond, it is called “negative skid”. If it is directed away from the ball bond, it is called “positive”. The schematic visualizations of the ultrasonic, scrub, and skid motions are shown in Figs. 34 (a), (b), and (c).

In ultrasonic bonding, the ultrasonic vibration assists wire deformation and provides cleaning of the interfacial area by friction, which consequently brings cleaner surfaces close to each other and facilitates bonding. In the absence of the ultrasound, the scrub and skid can assist in a similar way.

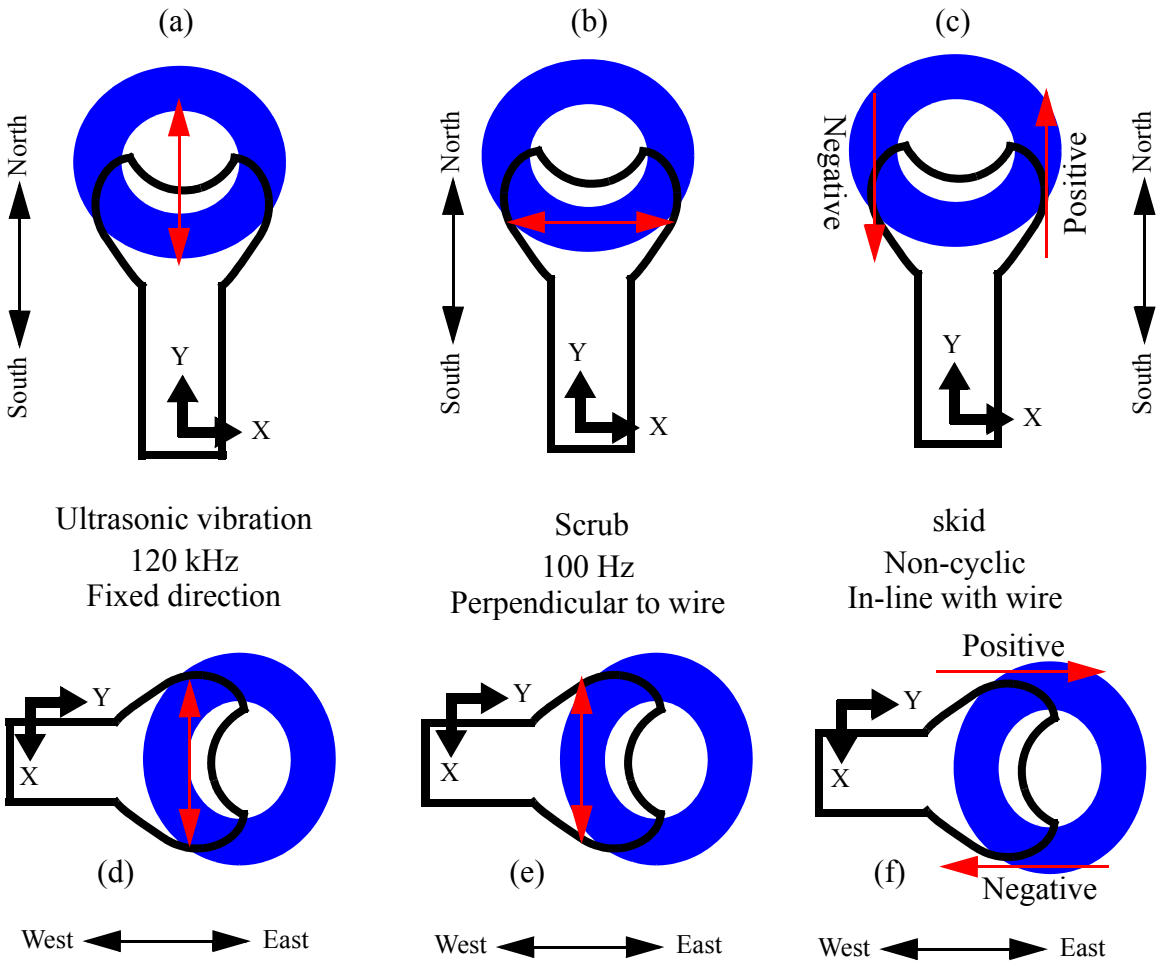

Fig. 34 Schematic visualizations of ultrasonic, scrub, and skid motions for two different wire directions. South to north wire direction (a) ultrasonic, (b) scrub, and (c) skid. West to east wire direction (d) ultrasonic, (e) scrub, and (f) skid. Pictures show that the wire direction influences the function of ultrasonic vibration while it has no effect on scrub and skid.

As there is no ultrasound for the stitch bond processes of substrates such as QFN, the bonding mechanism remains questionable. Even though the low frequency motions can provide some friction for cleaning, its amount is expected to be much less than that of high frequency ultrasonic vibration. Without application of ultrasonic vibration, the process looks more like cold welding. Therefore, a study of cold welding mechanisms might reveal some clues about the root causes of bonding in absence of ultrasonic vibration.

2•3•2 Cold welding Mechanism

Cold welding has been used for a large number of applications. To achieve successful cold welding, it is important to provide sufficient deformation (elongation) at the interface [73-79]. Mohamed et al [73] for the first time suggested a mechanism for cold welding. They found that a certain level of plastic deformation is required to break the oxides and encourage the bonding. This deformation is normally expressed as surface expansion X at the interface defined as

$$X = \frac{A_1 - A_0}{A_0} \tag{4}$$

The bonding strength for samples welded by rolling in pure shear for some combinations of metal pairs is shown in Fig. 35. The important message of this figure is that no bonding is happening until a certain amount of surface expansion is achieved. This is called the critical surface expansion (X_C). Its value for a specific metal-metal pair might vary from one process to another because the level of surface cleanliness, surface roughness, and bonding temperature influences the magnitude of the required X_C.

To further understand the mechanisms behind cold welding, Bay [74] carried out a series of tests for Al-Al cold welding with a custom designed pressure welding test setup. The force (pressure) and the level of surface expansion were. The outputs recorded included the weld strength, and scanning electron microscope (SEM) micrographs of the weld interface at different conditions. The pressure is expressed as $\frac{\bar{P}}{2K}$ where $\bar{P}$ is the normal pressure at the bonding surface and K is yield strength of aluminum at pure shear (pure shear is used to match the experimental condition). The weld strength is reported as the ratio of bond strength σ_B to tensile strength of base material σ_t, in the form of $\frac{\sigma_B}{\sigma_t}$. Three levels of $\frac{\bar{P}}{2K}$ equal to 1.6, 2.9, and

4.4 are used. The bond strength as a function of pressure and surface expansion is plotted in Fig. 36. Results indicate that the bond strength depends on both surface expansion and pressure. The effect of pressure is more significant at low surface expansions. The higher the normal pressure, the stronger the bond.

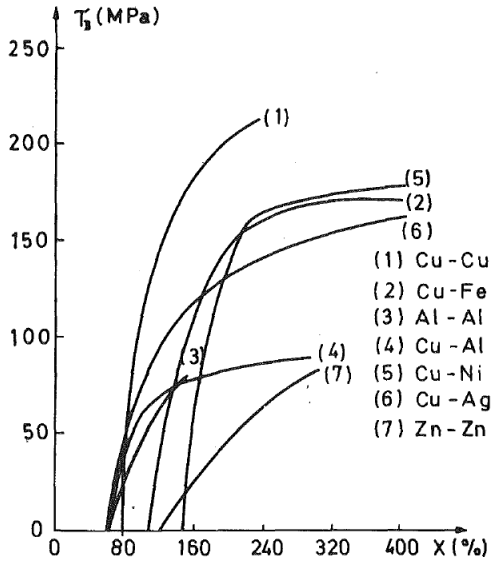

Fig. 35 Experimentally determined bond strength as a function of surface expansion, rolling [74].

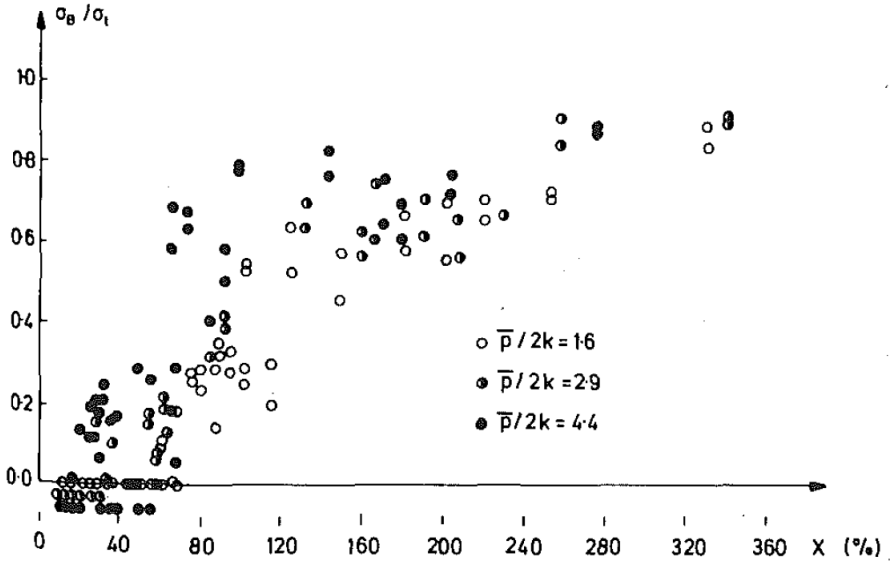

Fig. 36 Experimentally determined bond strength as a function of surface expansion and normal pressure [74].

SEM fractography can reveal some useful information about the bond mechanism. An example case with $\frac{\bar{P}}{2K}$ equal to 1.7 and $X = 0.6$ shown in Fig. 37 (a). The micrograph shows that at such relatively low pressure and low X, only the surface oxide layers (cover layers) are fractured and extrusion of the fresh metal areas from inside the cracks are started. However, there is not much contact between the fresh areas of both counterparts, and in consequence there is only a low bond strength of this sample ($\frac{\sigma_B}{\sigma_t} = 0.02$). The SEM micrograph for another example case with $\frac{\bar{P}}{2K}$ equal to 1.57 and $X = 2.54$ shown in Fig. 37 (b). Here, the unbonded regions of the surface oxide layer are small areas, and the bond fracture appears ductile including several neckings.

The suggested bonding mechanism is shown in Figs. 38 (a) to (d). In (a) the two surfaces are in contact but no pressure is applied on them. A small pressure initiates the fracture of the surface brittle layers and exposes the fresh metal areas (b). By increasing the pressure, surface expansion increases, and the fresh metal is starting to extrude through the cracks (c). Further increase in the pressure and surface expansion brings the extruded metal of each sides together and form the bond (d). This theory clarifies the necessity of a critical surface expansion to initiate the extrusion.

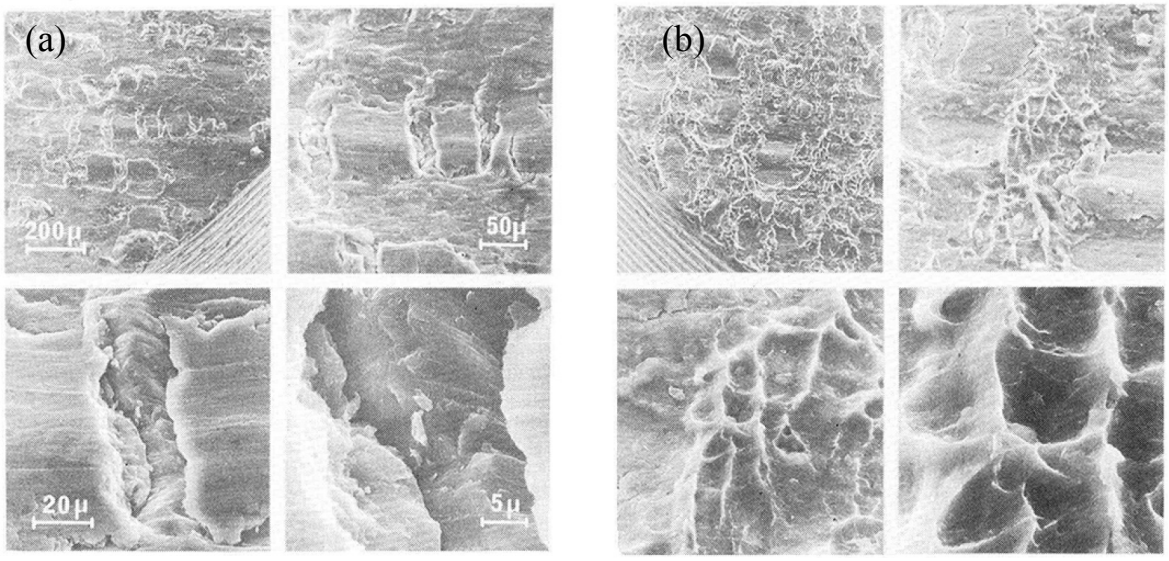

Fig. 37 (a) Scanning electron micrograph of bonding surface. $X = 60$ percent, $(P/2K) = 1.7$, $(\sigma_B/\sigma_t) = 0.02$) (b) Scanning electron micrograph of bonding surface. $X = 254$ percent, $(P/2K) = 1.5$, $(\sigma_B/\sigma_t = 0.71)$ [74].

2•4 Analytical and Numerical Approaches to Wire Bonding

In addition to mechanisms required for welding the wire to the substrate, there are deformation mechanisms altering the geometry of the wire during the process. In addition there are complexities in bond pad/wire/capillary material parameters. Overall, these complexities make finding an analytical solution difficult. However, e.g. for the case of the stitch bond, there are similarities with other processes such as cutting processes or wedge indentation as shown in Figs. 39 (a) and (b). An example indentation study by Grunzweig [80] is performed on the wedge indentation process. The goal of this work was to find the penetration, contact pressure, and plastic deformation fields in a substrate indented by hard wedge shape indenter.

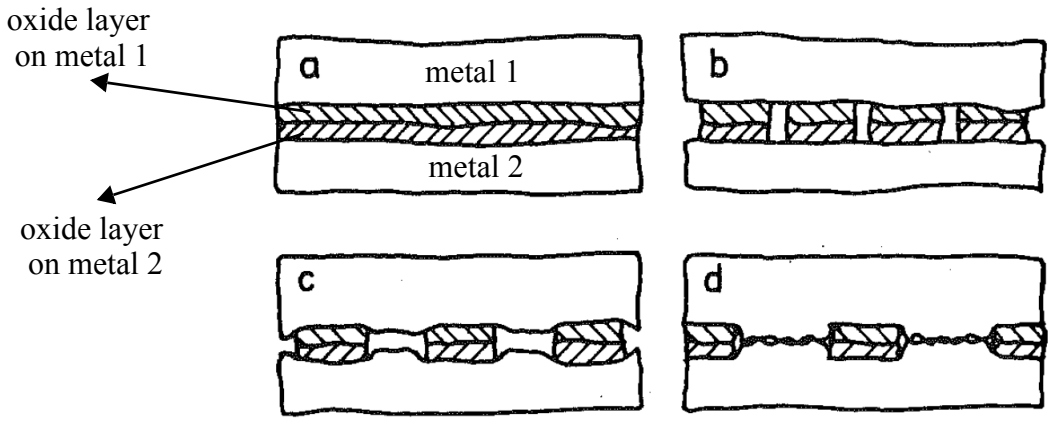

Fig. 38 Schematic outline of the bond formation [74]. (a) Metal 1 and metal 2 with their oxide layers, before bonding (b) pressure is applied and start to break the oxide layers (c) fresh metals 1 and 2 extrude into the cracks (d) extruded metals reach each other and form the bond.

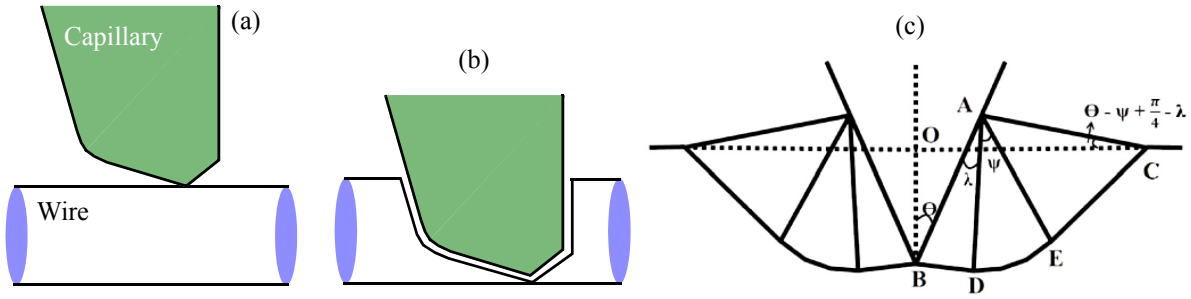

Fig. 39 Simplified cutting (indentation) problem in stitch bonding process (a) before, and (b) after cutting [81]. Only one side of capillary tip is shown. (c) Theoretical solution for wedge indentation problem [80].

The geometry of the wedge tool and the material are shown in Fig. 39 (c). Considering the geometry and the physics of the problem, these solutions are extracted for the specific problem with wedge indentations

$$h\cos\left(\Psi+\lambda-\frac{\pi}{4}\right)-c\cos\left(\Theta-\Psi-\lambda+\frac{\pi}{4}\right)=\frac{c\sin\Theta}{\sqrt{2}\cos\lambda} \tag{5}$$

$$h\cos\Theta-c=\sqrt{2}h\cos\lambda\sin\left(\Theta-\Psi-\lambda+\frac{\pi}{4}\right) \tag{6}$$

$$P=k(1+2\Psi+\sin 2\lambda) \tag{7}$$

$$\cos 2\lambda=\mu(1+2\Psi+\sin 2\lambda) \tag{8}$$

and h is length of AB, c is depth of penetration, μ is friction coefficient, P is pressure on wedge, and k is shear yield stress. Using these equations, it is possible to calculate the penetration depth of a hard wedge into a substrate and extract contact pressure for a variety of different substrates, different friction coefficients, and different geometries of wedge tool. The solutions indicate that the penetration depth and the contact pressure highly depend on substrate shear yield stress, friction coefficient, and the wedge angle θ. Assuming a similarity between the solution for the wedge indentation and the stitch bond process, the shear yield stress, friction coefficient, and the wedge angle θ are expected to have significant influence on a successful stitch bond design and process. The penetration can be compared with deeper/ sharper cut at the tail bond region and correlate with the breaking force. Similarly, the contact pressure can be correlated with bond strength, especially for processes which contain low or no level of ultrasonic energy. In addition the effects of different substrate materials, different surfaces (friction coefficients), and different bonding tools (e.g. face angle of capillary) can be studied. However, a full adaptation of the wedge indentation problem solutions to the stitch bond would extend the model to 3D, replace the flat surface with a cylindrical wire, and replace the bottom side of the model from infinite to an interface (wire/substrate interface).

The cutting part of the stitch bond process is similar to ultrasonic cutting processes like those used in surgery and food processing [82]. However, the authors [82] did not provide an ana-

lytical theory describing such cutting processes. Figures 40 (a) and (b) show images of typical ultrasonic cutting tools in surgery and food cutting, respectively.

Numerical solutions were reported to understand the stress distribution at the wire/substrate area [83-100]. Compared to analytical approaches, the numerical approach has the advantage of taking other parameters such as material parameters into account.

The FE method (FEM) has been used to model the wire bonding process [83-100]. As the ball bond is placed on brittle material such as silicon or low K materials, the main concern is the amount of stress transferred to the bond pad area during bond process. The target of several papers is mainly to minimize the transferred stresses to minimize the failure risks. In [90], Zhang investigated the effect of bonding parameters on ball bond deformation and stress distribution. His model is shown in Fig. 41. Figure 42 shows the von Mises stress distribution at

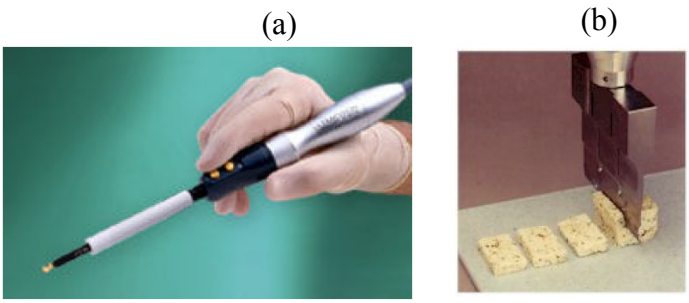

Fig. 40 Ultrasonic cutting tool, a) Surgery, and b) Food cutting [82].

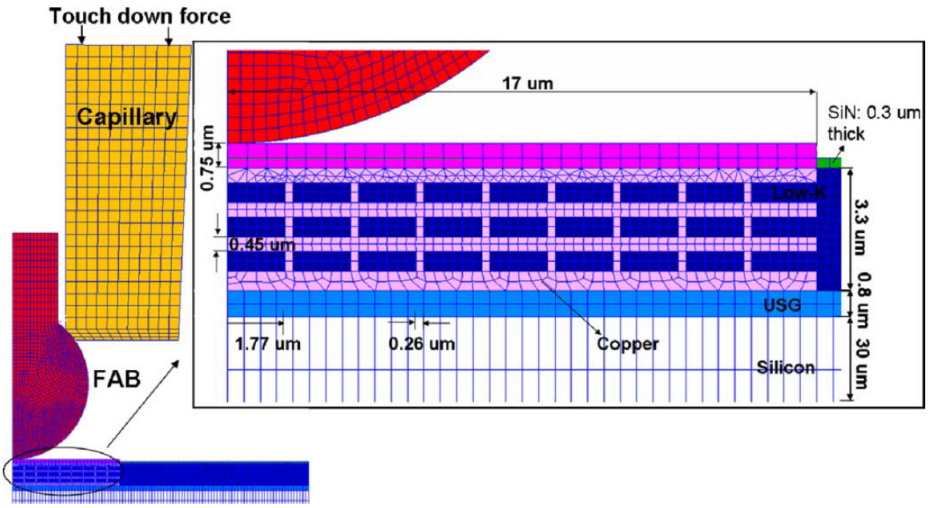

Fig. 41 Schematic of 2-D FE Model of ball bond [90].

different bonding times. He concluded that increasing the ultrasonic vibration amplitude increases the stress transferred to the bond pad, and increase the wire deformation.

In another FEM study of the ball bond [99], the effect of bonding parameters and wire bond position was investigated. They used Cu free air ball bonded to Cu substrate. The mesh and von Mises stress distribution of their model is presented in Fig. 43. Their results showed a good agreement with the experimental stress distribution measured by Raman microscopy.

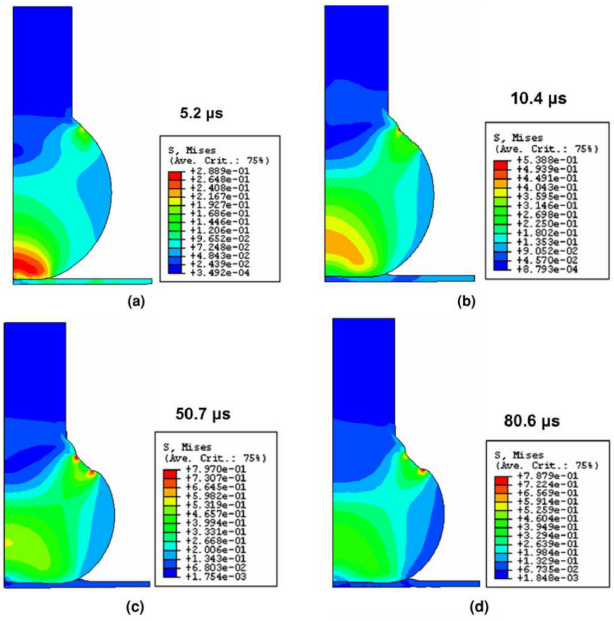

Fig. 42 Von Mises stress distribution within bonded ball and bond pad at various bonding times [90].

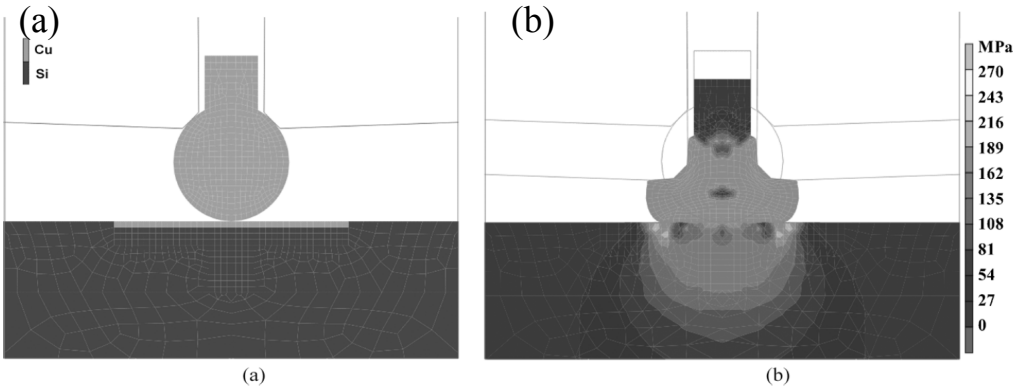

Fig. 43 FE model of Cu-to-Cu wire bonding. On top is the capillary tool. (a) Model mesh (b) von Mises stress at the end of the deformation process (before ultrasonic vibration) [99].

They concluded that bonding temperature and wire bond position on the bond pad, significantly affect the stress distribution in bond pad which could relate to the risk of failure in underpad materials.

Fewer studies simulated the wedge-wedge bonding process [83, 91, 94, 96, 100]. In [100] a wedge-wedge bonding process was modeled using the FEM software of ABAQUS^{TM} (SIMULIA, Providence, Rhode Island, United States). They developed both 3D and 2D models. They used Au wire and a Ni-Cu substrate (lead frame). Figures 44 (a) and (b) show the von Mises stress distribution in their 3D model at a low and a high forces, respectively. Their model showed that the maximum contact pressure occurs at the periphery of bonds which was in good agreement with experiments, as shown in Figs. 45 (a) to (c).

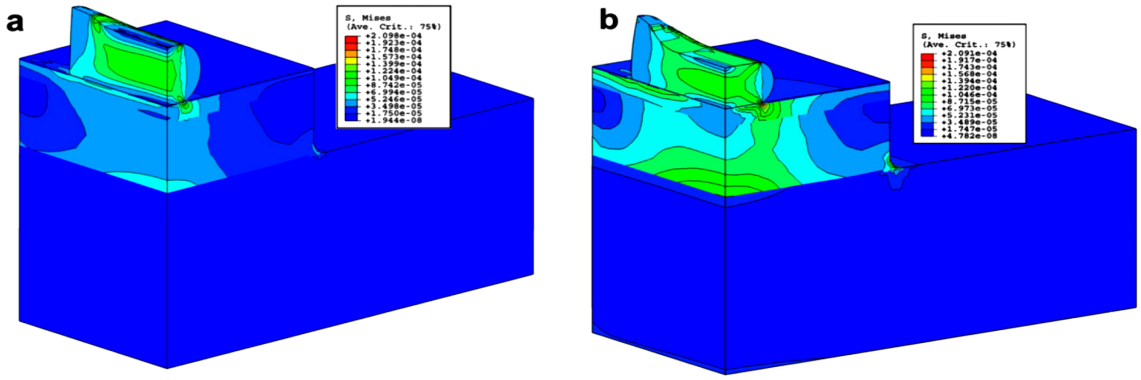

Fig. 44 von Mises stress distribution in wedge-wedge bonding process at (a) 0.1 N, and (b) 0.2 N forces [100].

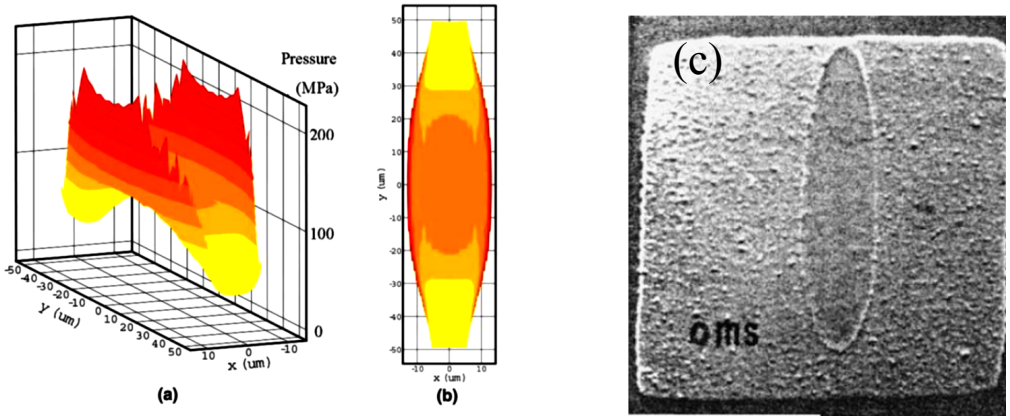

Fig. 45 Contact pressure distribution in FE model of wedge-wedge bond (3D), (b) 2D top view. (c) the SEM micrograph of the real wedge bond [100].

Then using the 2D model, they applied different levels of normal forces and measured contact length, maximum contact pressure, and average contact pressure. Results are shown in Figs. 46 (a) to (f).

According to the 2D model, the maximum contact pressure happens at the contact periphery at each normal force. The contact length increases by increasing the normal force as shown in Fig. 46 (e), however, the maximum and average contact pressure does not necessarily increase by increasing bond force as shown in Fig. 46 (f). It was concluded that increasing bonding force does not necessarily enhance the bond strength. Next, they calculated the generated fric-

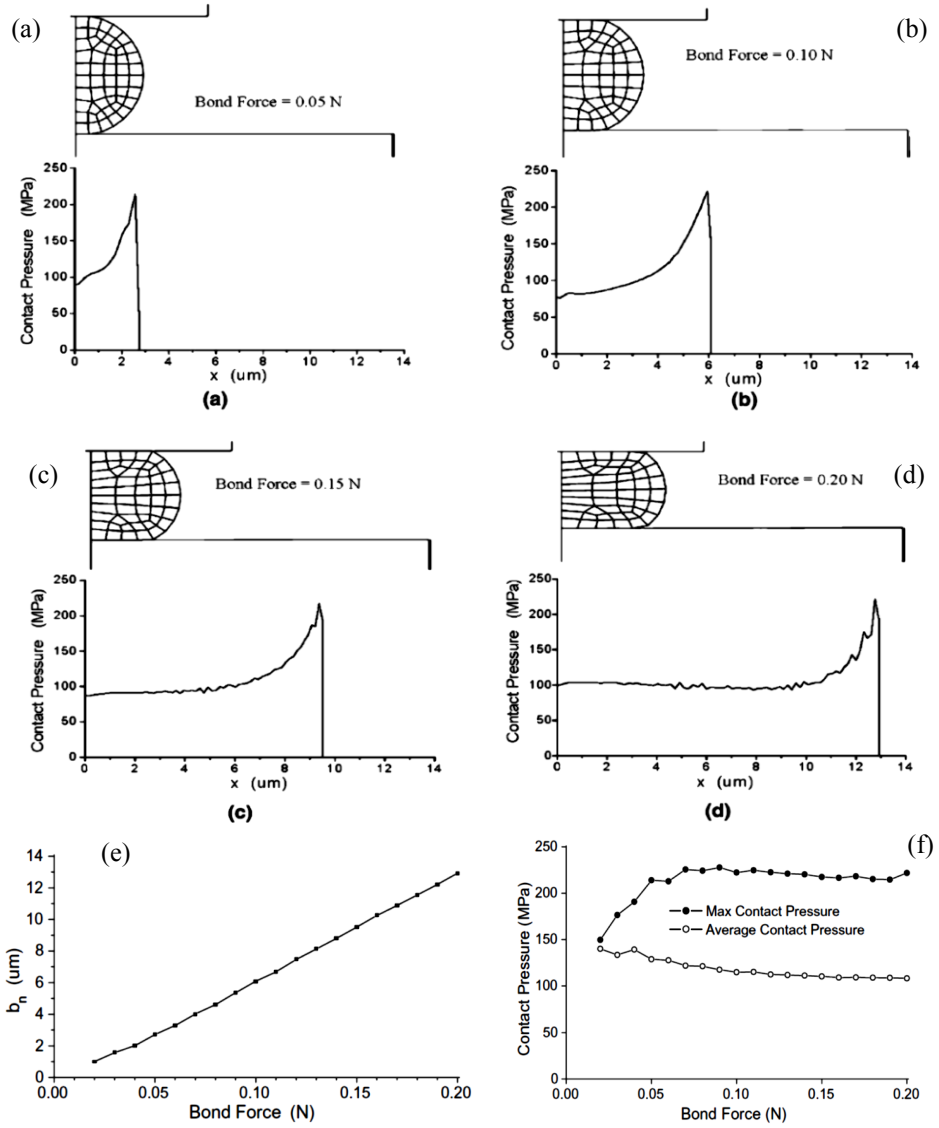

Fig. 46 Distribution of the contact pressure along the contact for different forces (a) 0.05 N, (b) 0.1 N, (c) 0.15 N, and (d) 0.2 N. (e) Contact length at different bond forces, (f) Maximum and average contact pressure at different bond forces [100].

tion intensity at the contact interface for variety of forces. The friction energy intensities were measured for ultrasonic frequency of 60 kHz and an amplitude of 1 µm. The friction density distribution at the contact for four different bond forces are shown in Figs. 47 (a) to (d). As results show, the frictional density is maximum at the bond periphery for all four forces. In addition, they calculated the total friction energy per unit length as shown in Fig. 48. They concluded that the friction energy density is an important factor for a successful bonding.

In a more recent work, Kramer et. al. [83] studied the FE analysis of wedge-wedge aluminum wire bonds on Cu bond pad. Their model included bonding force and horizontal low frequency vibration. The model is visualized in Fig. 49 together with the vertical and horizontal movement of the wedge tool (process parameters). In this work, the FE software of LS-Dyna (Livermore Software Technology Corporation, Livermore, California, USA) is used to model the process. The stress distribution in the underpad is shown in Fig. 50. Their work showed

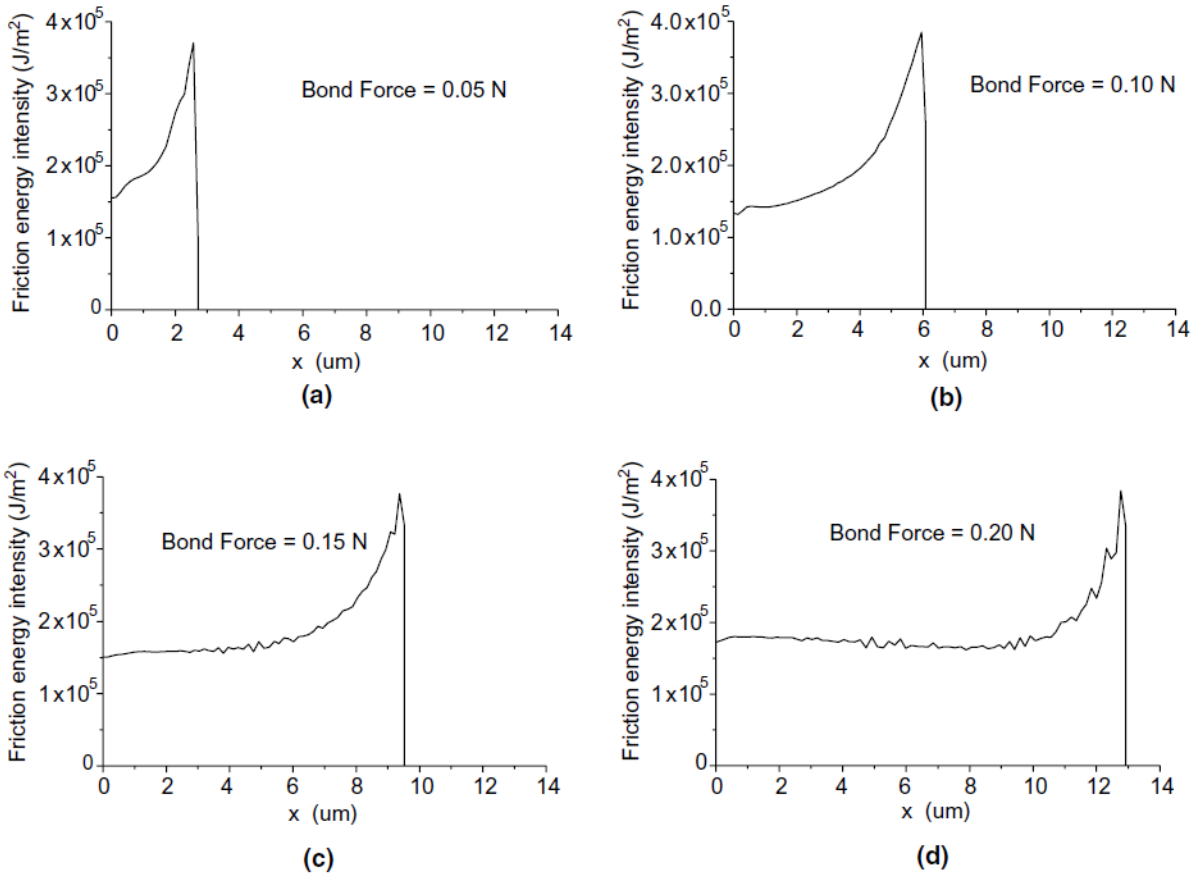

Fig. 47 Distribution of friction energy density in the wire - substrate contact interface for different bond forces (a) 0.05 N, (b) 0.1 N, (c) 0.15 N, and (d) 0.2 N [100].

that the material type of the underpad and its stiffness can influence the maximum contact force between wire and substrate, which consequently can influence the bond formation process. They concluded that such differences in the stiffness (elastic modulus) and material type of underpad can change the amount of contact pressure at wire-substrate interface, which can consequently initiate problems in microjoining of wire to substrates.

Takahashi et al. [84, 85] studied the numerical analysis of wedge-wedge bonding process. Wedge-wedge bonding is a similar process to the stitch bonding process. A wedge tool is used in wedge-wedge bonding process instead of capillary for bond formation. Takahashi et al. used the cold welding theory proposed by Mohamed [73] and Bay [74] to find the effect of process parameters on the wedge-wedge bonding process. They calculated the surface expansion (also called extension) at the wire/pad interface with a 2D FE model. They correlated the deformed wire geometry with experimental observations. According to their findings the periphery of the bond results in larger surface expansion than central regions and therefore can have a stronger adhesion. Their model geometry and calculated surface extension at the wire/pad interface are shown in Figs. 51a and 51b, respectively. They did not provide information about the correlation between process parameters and the experimental observations.

In [86 and 87] Saiki et al. investigated the deformation behavior of the Au ball bonds on the Al pad using self developed FE code and correlated the numerically calculated bonded ball diameter and thickness with experimental observations. Their results showed that a softer pad (softer pad is equal to a higher flash) results in a less ball deformation. In addition they found

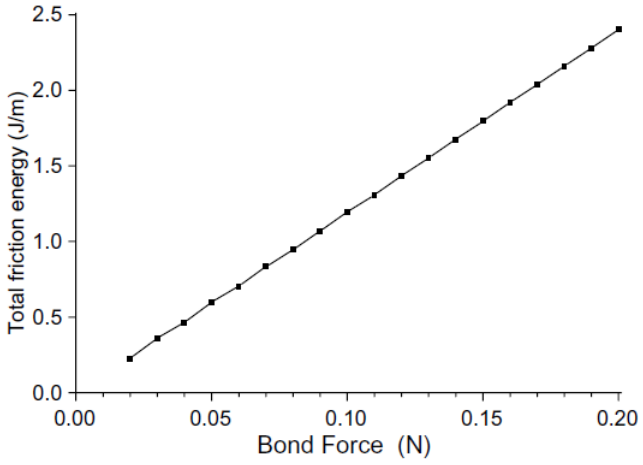

Fig. 48 Total friction energy generated at the contact interface as a function of bond force [100].

that with a sharper chamfer angle, CA, a higher sliding distance can be achieved. Therefore it is possible to optimize the bonding with changing the CA.

The thermal field distribution at the interface was the subject of some numerical work [88, 89]. In [88] the temperature distribution at the Au-Ni ultrasonic wedge-wedge bonding interface is analyzed by a proper using of FE method by authors. In [89] the temperature distribution at the Al-Al ultrasonic ribbon bonding interface is analyzed using FE. Both of the above mentioned analyses showed that the temperature rise is less than 100 °C. For the case of non-ultrasonic bonding even less than 100 °C temperature rise is expected since there is no high frequency ultrasonic motion.

According to literature investigated on the FE of the wire bonding process, no paper has been found that contains a correlation between stitch bond model responses and bond quality. They rather are about the stress transferred or the temperature rise at the interface.

The development of a FE model that could correlate the numerical responses to the experimental observation of the stitch bond quality could be useful in order to enhance the knowledge about bond formation, and effect of process parameters. Such a correlation could be useful for improving the stitch bonding process. In addition, it could be useful in order to understand the observations and mechanisms with some of the other processes which deal with cold welding and solid-state joining.

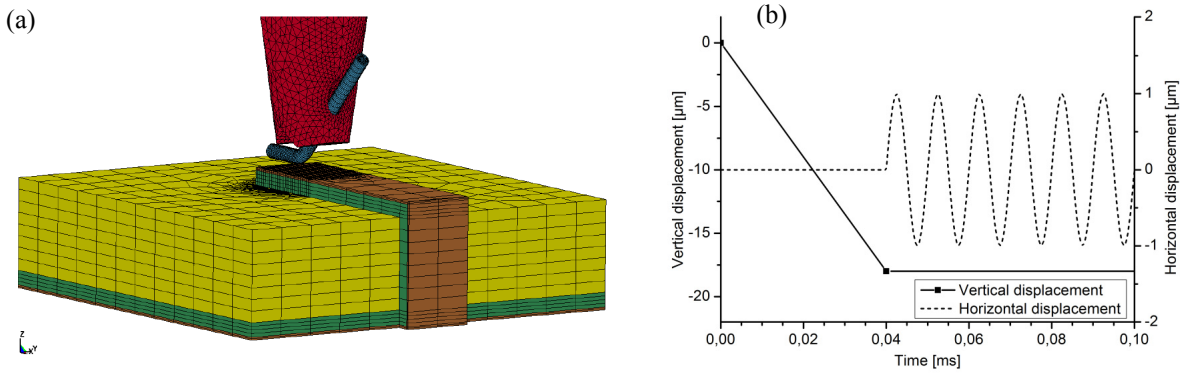

Fig. 49 (a) 3D FE model of wedge-wedge bonding process. (b) Vertical and horizontal displacement curves of the wedge tool for the bond simulation [83].

2•5 Status of Stitch Wire Bonding

The stitch bonding process is similar to other solid-state welding processes including cold pressure welding. Therefore not only a clean surface requirement (mainly by friction energy), but also a certain amount of surface expansion at the bond interface is a determining key for a successful bond. Previous experimental and numerical studies have improve the understanding of the stitch bonding process including wedge and tail bond.

Experimentally, the following two findings were obtained:

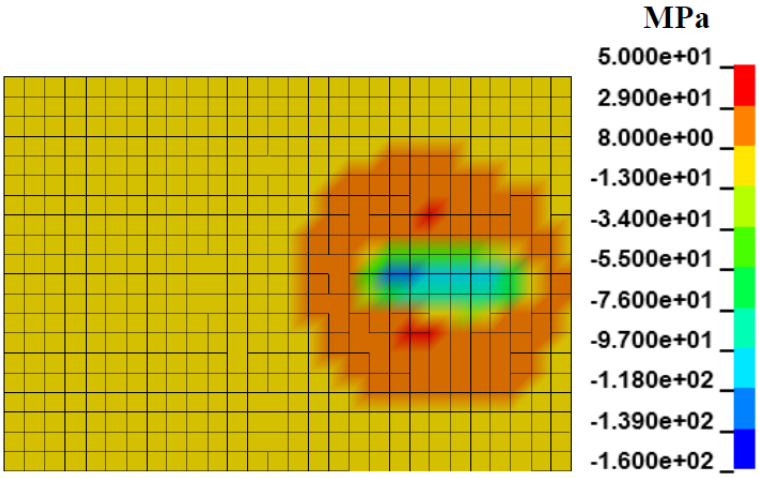

Fig. 50 Distribution of the first (maximum) principal stress distribution on the Cu bond pad in case of a silicon substrate at the end of bond wire compression [83].

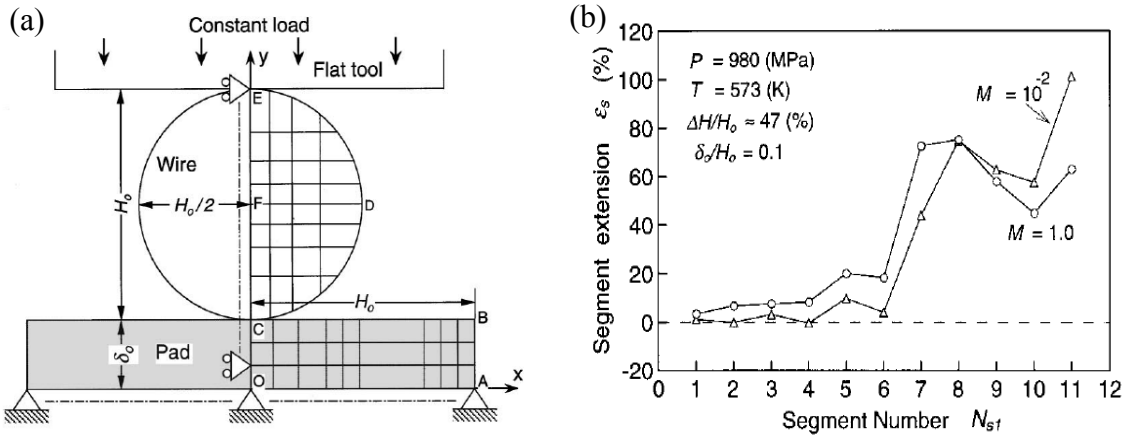

Fig. 51 Wedge-wedge wire bonding model geometry. (a) model parts (b) Surface expansion (extension) for two different ratios of the pad/wire hardness. [85]

1. The stitch bond forms by simultaneous actions of wire deformation by bond force and vibratory motions, and interface cleaning by vibratory motions. The wire deformation is not the only process response determining the stitch bond quality.

2. It is possible to use DOEs to improve the stitch bond quality and optimize the responses stitch bond pull force and tail breaking force.

Numerically, it has been found that bonding force and vibratory motions influence the contact pressure and friction energy generation at the contact interface. For the case of bonding on sensitive substrate, the bonding force and vibratory motions transfer stress to the substrate and underpad materials, which need to be carefully adjusted to manage the risk of failure.

This work relies on previous efforts as a basis for addressing some of the remaining challenges of the stitch bonding process. For example, there is a lack of experimental work on recently developed QFN substrates. With these substrates, the use of conventional vibratory motion of ultrasound is usually avoided as it can cause bond pad resonance, excessive deformation, and bouncing. The newly developed process parameters QFN substrates are scrub and skid, and there are few reports about their effects on the stitch bonding process. This is addressed in this work.

A remaining challenge for numerical studies is to improve the correlation of numerical stitch bond process responses with experimental observations. A similar challenge exists for cold welding processes. Until now there has been no comprehensive effort to link numerical responses for interfacial surface expansion and friction energy with experimental quality of stitch bonds.

3 Stitch Bonding Process of Cu wire on QFN Substrate

This chapter discusses the experimental procedure used for stitch bonding of Cu wire on QFN substrate. Two DOEs are carried out (Test I and Test II) and described in subsections 1 and 2, respectively. The results are discussed in subsection 3.

3•1 Test I: Stitch Bond Process Window

3•1•1 Experimental Procedure

For the first type of experiment, 0.7 mil (18 µm) diameter Pd coated Cu (PCC) wire is selected as wire material. The substrate used was an Au/Pd/Ni PPF (pre-plated frame) Cu QFN. The schematic cross section of substrate is shown in Fig. 52. The optical micrograph of the Au-plated Cu QFN substrate is shown in Fig. 53. This substrate has a low stitch bondability, therefore PCC wire is selected to provide a sufficient range of stitch bond responses regarding

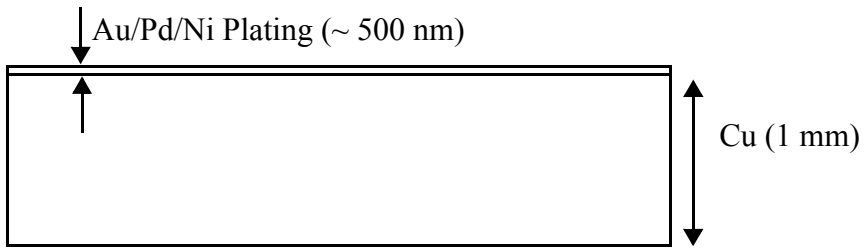

Fig. 52 Schematic cross-section of Au/Pd/Ni plated Cu QFN substrate.

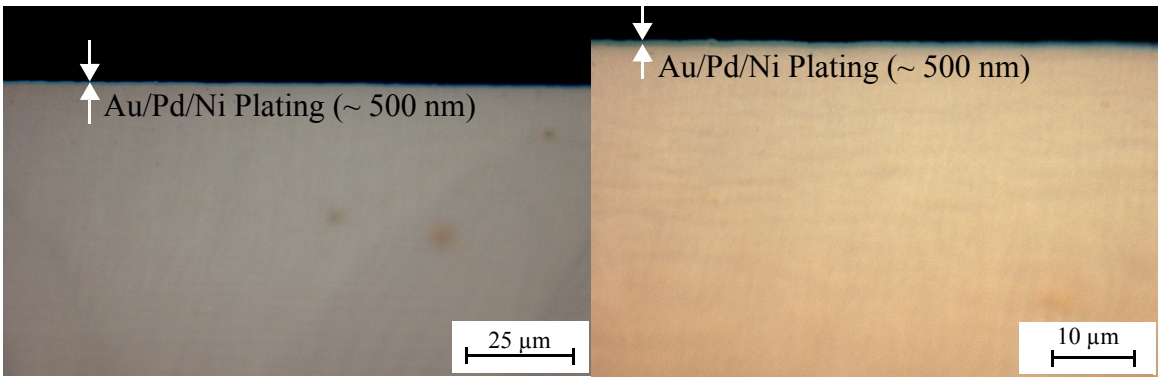

Fig. 53 Optical micrograph of cross-section of Au/Pd/Ni plated Cu QFN substrate at different magnifications. (a) 50× and (b) 100×

the stitch bond sticking or non-sticking, and tail lifting. The capillary used was a conventional Cu capillary made of alumina. The capillary geometry is shown in Fig. 54 and explained in Table 1. The images of the wire spool, QFN substrate, and capillary are shown in Figs. 55 (a), (b), and (c), respectively.

To bond the samples, an automatic wire bonder marketed by Kulicke and Soffa Ind. (Fort Washington, PA, USA) is used. The image of the wire bonder is shown in Fig. 56.

As this experiment is a DOE, all bonding parameters are kept fixed, except the bond force, scrub amplitude, and skid parameters. The skid parameter is called "XY-Distance" on the K&S wire bonding machine. The bonding temperature was kept constant at 200 °C. Contact velocity (CV) was kept fixed at 0.3 mils/ms (7.62 µm/ms), and is representative of the impact force. A one segment bonding procedure is used for stitch bonding. No pre-ultrasound "pre-bleed" is used. The bonding parameters are is shown in Fig. 57. Instead of ultrasound, the low frequency XY motions scrub and skid are used. A total of three 100 Hz cycles of scrub per-

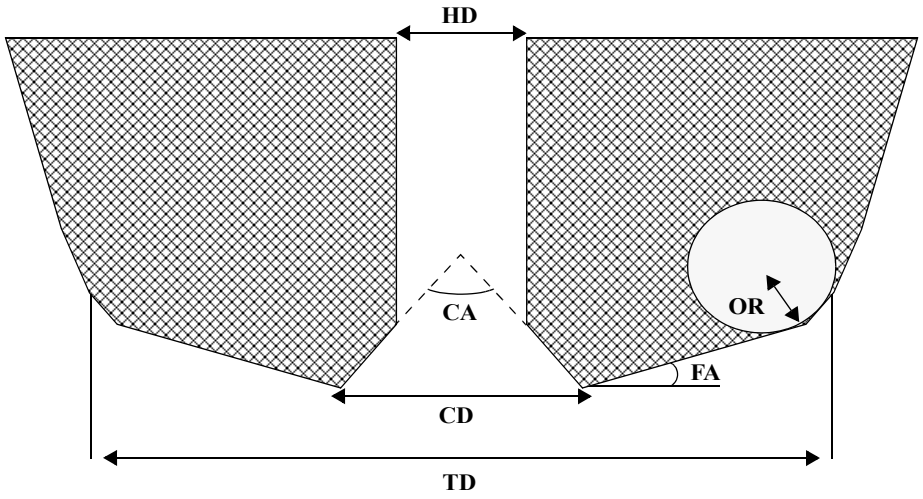

Fig. 54 Capillary geometry details.

Table 1: Capillary geometry used for PCC wire on Au plated QFN

Feature	Hole Diameter (HD) [µm]	Chamfer Diameter (CD) [µm]	Tip Diameter (TD) [µm]	Outer Radius (OR) [µm]	Face Angle (FA) [°]	Chamfer Angle (CA) [°]
Value	23	27	70	5	11	90

pendicular to the wire loop direction are used throughout the entire DOE. The total stitch bonding time from capillary touchdown to lift-off is 55 ms. In the DOE, three levels of scrub

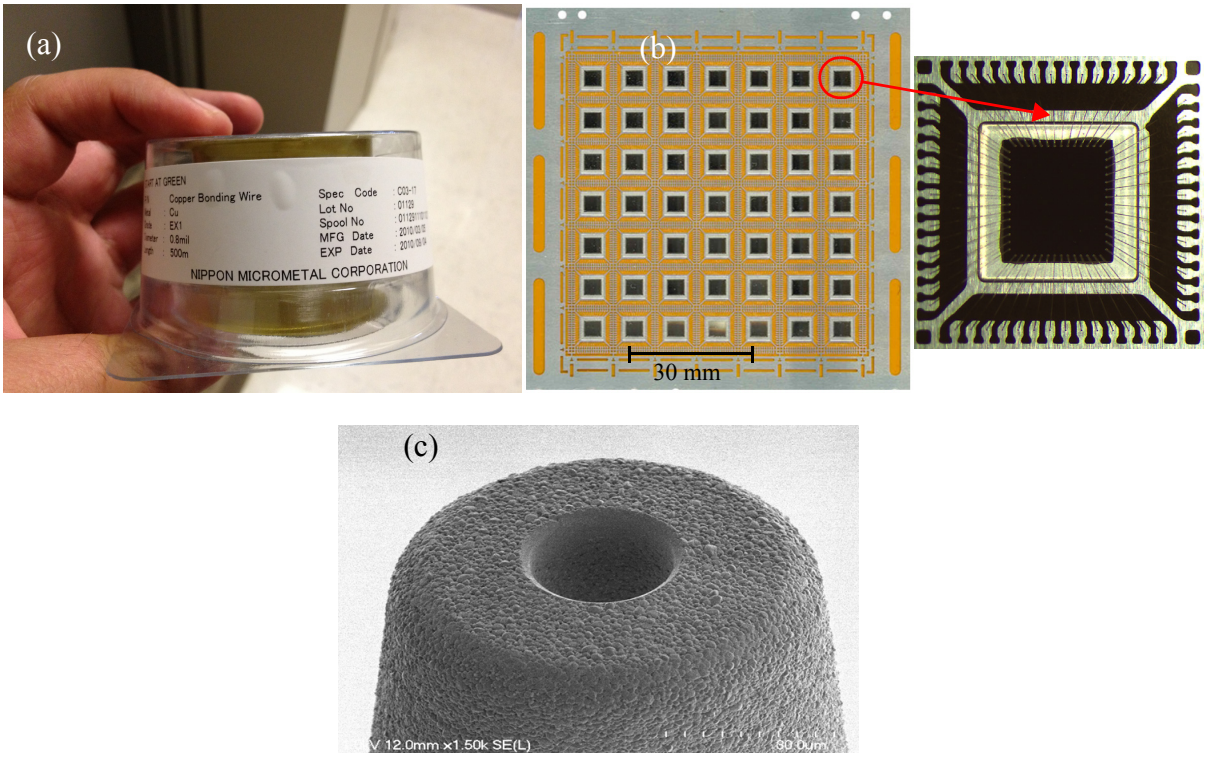

Fig. 55 (a) PCC wire spool (b) QFN substrate with zoom of one device (c) SEM image of capillary surface.

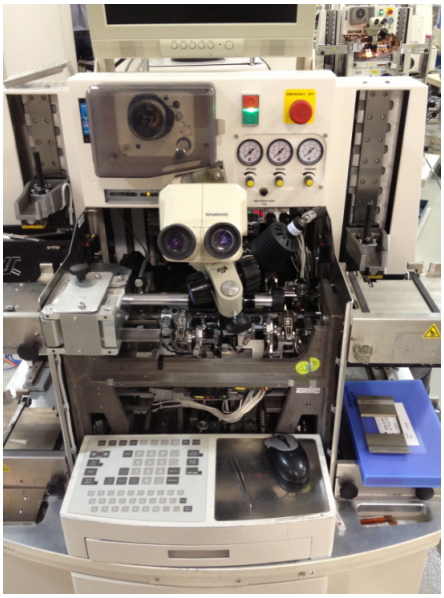

Fig. 56 K&S automatic ball-wedge wire bonder. The model is ConnX Plus.

amplitude are used: 1 µm, 3 µm, and 5 µm. Three levels of skid are used: -5 µm, 0, and +5 µm. Five levels of bond force are used: 30 gf, 40 gf, 50 gf, 60 gf, and 70 gf. A total of 45 (3 × 3 × 5) cells are included in the DOE. The variables of the DOE are summarized in Table 2.

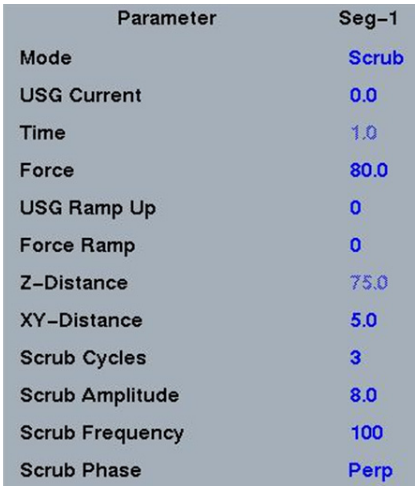

Parameter	Seg-1
Mode	Scrub
USG Current	0.0
Time	1.0
Force	80.0
USG Ramp Up	0
Force Ramp	0
Z-Distance	75.0
XY-Distance	5.0
Scrub Cycles	3
Scrub Amplitude	8.0
Scrub Frequency	100
Scrub Phase	Perp

Fig. 57 Stitch bonding parameters on K&S automatic wire bonder taken as screenshot from wire bonder machine.

Table 2: DOE 1 Process Parameters and Cells

		Force [gf]						
		30	**40**	**50**	**60**	**70**		
skid [µm]	**+5**	1	2	3	4	5	**1**	**Scrub Amplitude [µm]**
	0	6	7	8	9	10		
	-5	11	12	13	14	15		
	+5	16	17	18	19	20	**3**	
	0	21	22	23	24	25		
	-5	26	27	28	29	30		
	+5	31	32	33	34	35	**5**	
	0	36	37	38	39	40		
	-5	41	42	43	44	45		

For each DOE cell, 5 stitch bonding attempts are tried. Each “attempt” means an individual stitch bonding trial. This attempt could result in a perfectly sticking stitch bond and a repeatable tail bond (so the wire bond loop completes). If the wire does not stick or the tail breaks before the tail adjustment step, the previously designed circuits in the wire bonder detect a short in the current (voltage) which can be attributed to either non-sticking or tail lifting. For each sample the sticking, non-sticking, or tail lifting is observed. The non-sticking and short tail observations are more common to be addressed by Non Sticking on Leadfinger (NSOL) and “short tail” in the industry, respectively. If for 3 or more attempts out of 5 attempts the stitch bond was sticking to the bond pad, then the corresponding DOE cell is labeled as “sticking”, otherwise it is considered as “non-sticking”. The other observation (response) is the tail lifting. Tail lifting happens if there is no or a too small wire tail left after the stitch bond. Tail lifting or short tail can be detected by the wire bonding machine. The basis of the detection is the fact that once the tail is missing or too short, it is not electrically connected to the substrate anymore which alters the impedance measured between the wire clamp and the oven plate. Consequently, the next free air ball (FAB) would not have enough material to proceed with an arc, and so the machine sends an alarm. For a sticking stitch bond, if for 3 attempts or more than 3 attempts out of 5 attempts the sticking stitch bond results in tail lifting, then the corresponding DOE cell is labeled as “tail lifting”, otherwise it is kept as “sticking”.

3•1•2 Results

To evaluate the effect of process parameters, the occurrence of non-sticking, sticking, and tail lifting (i.e. the stitch bond status) is recorded for each of the samples. The results are shown in Fig. 58 together with typical example micrographs of wedge bonds.

The very first observation is that the chance of sticking is increasing with increasing the scrub amplitude and force. This is mainly due to the increased wire deformation and expansion. The increase in the capillary tool mark impression on the substrate supports this conclusion (Fig. 58). The absolute value of skid does not influence the bond quality proportionally. Instead, the sign (direction) of skid is the main factor determining its effect on the bonding. According to the results, the more positive (away from the ball bond) the skid, the higher chance of the sticking, while a negative skid (toward the ball bond) decreases the chance of sticking.

The tail lifting occurs at two out of 45 DOE cells. The first case happens when scrub amplitude is 5 µm, skid is +5 µm, and bond force is 60 gf. The second case happens when scrub amplitude is 5 µm, skid is +5 µm, and bond force is 70 gf. Both of the cases are happening when positive skid is used, and at the higher forces. It seems that the same kind of process parameters trend which encourages sticking at low forces, increases the chance of tail lifting at higher forces. The tail seems to suffer from lifting when there is what could be expressed as excessive bonding or over-bonding. In other words, the excessive increase in the force, scrub amplitude, and positive direction of the skid, increases the chance of tail lifting. More fundamentally, tail lifting could be a results of excessive deformation in the tail area of the wires, or an ultra thin wire thickness at the tail area which facilitates the breakage of the wire from the stitch bond, resulting in a weak tail force.

Test I is an example for a systematic DOE to reveal a rough process window for a specific bonding system (capillary, wire, substrate). It could serve as a basis for a more detailed DOE to further optimize the process parameters if required.

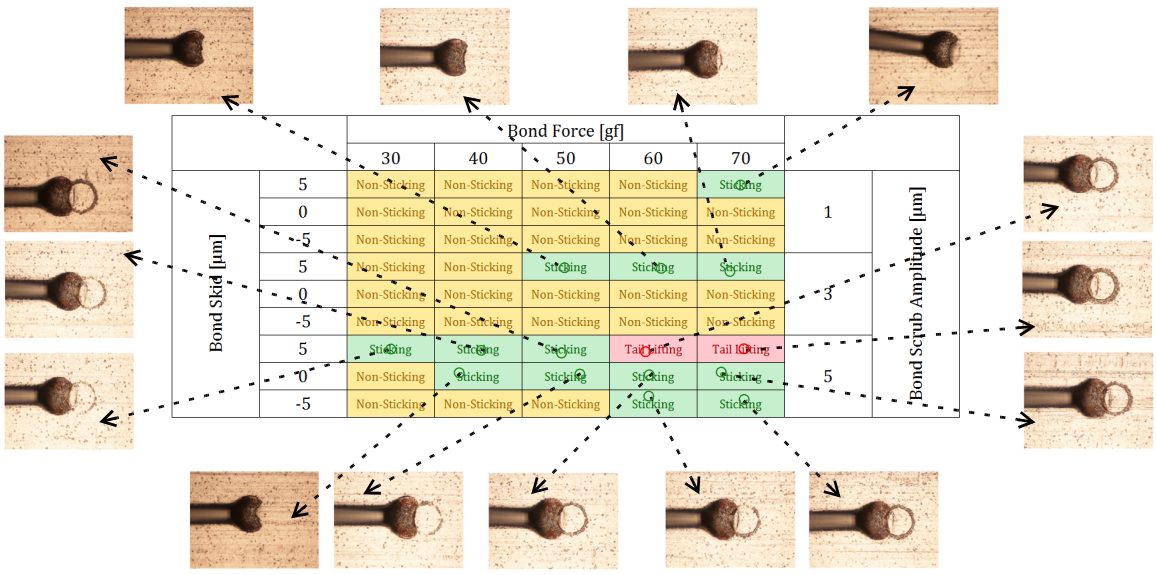

Fig. 58 Effect of process parameters on stitch bondability (qualitative) of PCC wire on QFN substrate. The scrub frequency is kept fixed at 100 Hz and the number of scrub cycles is kept fixed at three.

3•2 Test II: Stitch Bond DOE

Test II addresses how the process parameters influence the stitch bond quality within a already safe process window. In other words, what would be the best process parameters for the stitch bond process. To answer this question, an optimization experiment which is carried out with a full factorial DOE which results in bonding (sticking) for all DOE cells is helpful. As it could be seen for the Au plated PPF QFN substrate (test I), finding such a region is quite demanding (sometimes impossible) due to a relatively narrow process window. To proceed with the DOE (optimization) test, a new type of process is used in this subsection, which is able to provide successful bonding for a relatively wide range of process parameters.

3•2•1 Experimental Procedure

For the DOE part of the experimental approach, 18 µm diameter bare Cu wire is used as bonding wire. Instead of the Au plated QFN, a more bondable Ag plated QFN is used. The schematic cross section of substrate is shown in Fig. 59. Ag plated QFN is a highly bondable substrate. Using PCC on this type of substrate results in high quality stitch bonds (high stitch bond pull force, and high tail bond pull force), so there is not significant variations between samples bonded with different process parameters. To see a better variation in the stitch bond responses (low, high, and medium ranges for stitch and tail pull forces) the Cu wire is selected as bonding wire instead of PCC. In addition, despite the better stitch bonding performance with the PCC wire, industrial users are still looking for possibility of bonding with Cu wire, mainly due to its cheaper price [101]. The Ag plated QFN substrate is shown in Fig. 60. The bonding temperature is kept at 200 °C, and a conventional Cu capillary is used as bonding tool. The capillary made of aluminum oxide special for Cu wire bonding (similar material type of the capillary used in test I) is used. The geometry of the capillary is shown in Table 3.

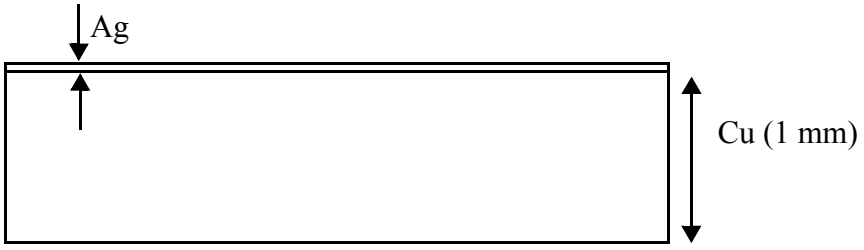

Fig. 59 Schematic cross-section of Ag plated Cu QFN substrate.

A 3 × 3 × 3 full factorial DOE (27 cells) is designed. The bond force (50, 60, and 70 gf), skid (-5, 0, and +5 µm), and scrub amplitude (3, 4, and 5 µm) at 100 Hz and 3 cycles, are the process parameters used. The responses collected are the stitch pull force and tail bond pull force. Each measurement is performed with sample size of at least 10. In addition, two qualitative responses including the stitch bond peeling severity and the capillary tool mark are recorded. To evaluate the peeling severity and the tool mark, they are ranked between 0 to 3, based on their severity, as shown in Fig. 61. A low peeling is desirable as it results in high reliability of stitch bonds. A low tool mark is helpful for ensuring a long capillary tool life (low wear).

3•2•2 Results Summary

To compare the stitch bonds made with different process parameters, optical micrographs of all the stitch bonds are taken. In addition, the stitch bond pull force and tail bond pull force are measured for all samples. The stitch bond pull force is measured by using a Dage 4000 pull tester (Aylesbury, UK), and the tail pull force is measured in-situ using the K&S wire bonding machine [43].

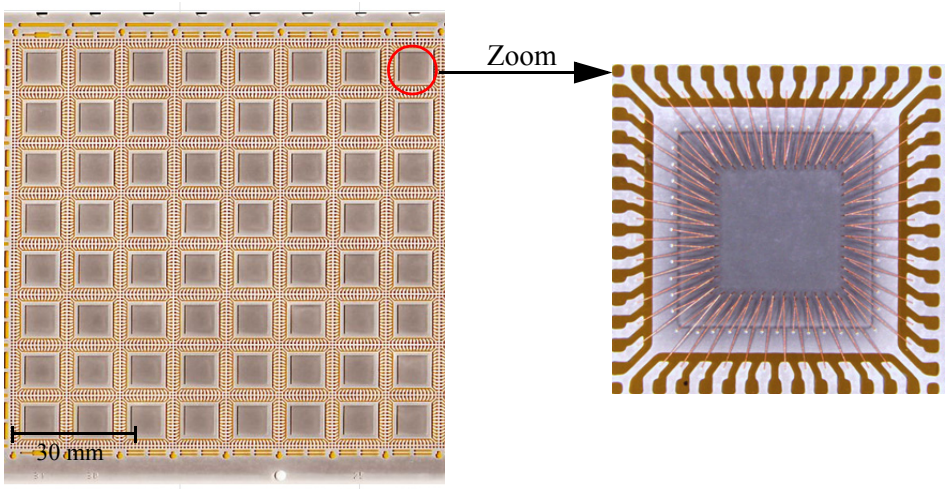

Fig. 60 Ag plated QFN substrate.

Table 3: Capillary geometry used for Cu wire on Ag plated QFN

Feature	Hole Diameter (HD) [µm]	Chamfer Diameter (CD) [µm]	Tip Diameter (TD) [µm]	Outer Radius (OR) [µm]	Face Angle (FA) [°]	Chamfer Angle (CA) [°]
Value	25.4	33	71	7.6	11	90

A quick summary of the resulting average values for stitch pull force and tail pull force, peeling severity, and tool mark for all cells is shown in Table 4. In addition to stitch and tail pull force, the process capability index (Cpk) is calculated and provided for all the DOE cells. The Cpk formula is

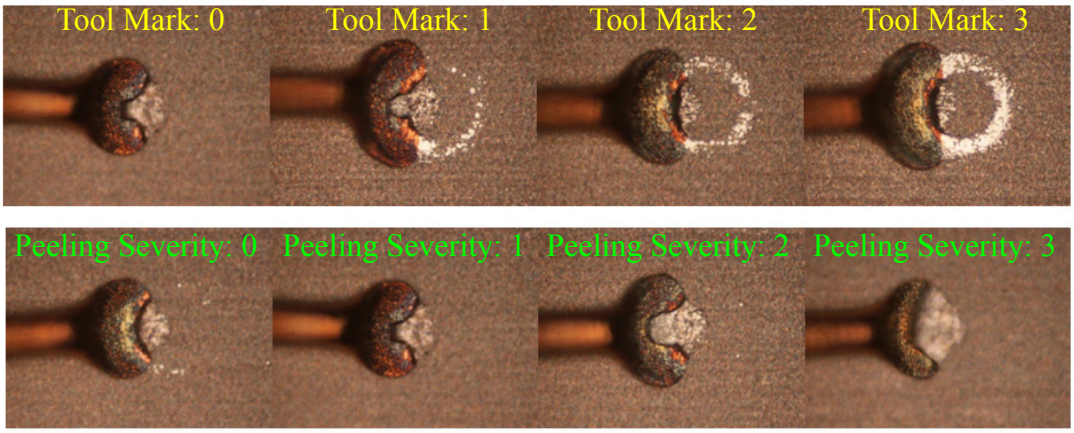

Fig. 61 Evaluation procedure of peeling severity and capillary tool mark.

Table 4: Stitch bond experiment DOE cells, process parameters, and process responses. The errors accompanying the averaged experimental responses are the standard deviations.

Cell #	Force [gf]	Skid [µm]	Scrub Amplitude [µm]	Stitch Pull [gf]	Tail Pull [gf]	Cpk Stitch	Cpk Tail	Peeling Severity	Tool Mark
1	70	0	4	5.5 ± 0.61	2.3 ± 0.19	1.3	1.5	1.0	3.0
2	70	5	4	5.5 ± 0.49	2.6 ± 0.23	1.7	1.6	0.0	3.0
3	50	0	5	5.6 ± 0.51	2.1 ± 0.15	1.7	1.4	2.0	2.0
4	60	5	3	5.3 ± 0.61	2.7 ± 0.14	1.3	2.8	1.0	1.0
5	50	-5	3	6.5 ± 0.78	2.5 ± 0.13	1.5	2.7	3.0	0.0
6	60	0	3	5.4 ± 0.97	2.7 ± 0.13	0.8	3.0	3.0	1.0
7	70	0	5	5.7 ± 0.54	2.5 ± 0.12	1.7	2.7	0.0	3.0
8	50	-5	4	6.3 ± 0.49	2.3 ± 0.14	2.3	2.0	3.0	1.0
9	50	0	4	5.7 ± 0.47	2.4 ± 0.19	1.9	2.3	2.0	1.0
10	50	5	5	5.4 ± 0.53	2.4 ± 0.17	1.5	1.7	0.0	3.0
11	70	5	5	5.7 ± 0.48	2.6 ± 0.19	1.9	1.9	0.0	3.0
12	50	-5	5	5.7 ± 0.57	2.2 ± 0.17	1.6	1.4	3.0	2.0
13	70	-5	5	5.9 ± 0.72	2.4 ± 0.15	1.3	2.0	3.0	3.0
14	70	-5	4	6.2 ± 0.78	2.5 ± 0.18	1.3	1.8	3.0	2.0
15	60	5	4	5.5 ± 0.60	2.7 ± 0.15	1.4	2.5	0.0	2.0
16	70	5	3	5.7 ± 0.59	2.9 ± 0.15	1.5	3.2	1.0	1.0
17	60	-5	4	6.2 ± 0.58	2.3 ± 0.18	1.8	1.5	3.0	1.0
18	60	5	5	5.5 ± 0.53	2.5 ± 0.17	1.6	1.9	0.0	3.0
19	50	5	3	4.8 ± 0.84	2.9 ± 0.16	0.7	2.9	3.0	0.0
20	60	-5	3	6.9 ± 0.66	2.6 ± 0.15	2.0	2.5	3.0	3.0
21	70	0	3	6.2 ± 0.58	2.8 ± 0.09	1.8	4.8	2.0	1.0
22	50	0	3	5.2 ± 0.98	2.7 ± 0.13	0.8	2.9	3.0	0.0
23	60	-5	5	5.7 ± 0.79	2.2 ± 0.18	1.1	1.2	3.0	3.0
24	60	0	5	5.6 ± 0.57	2.4 ± 0.15	1.5	1.9	0.0	3.0
25	50	5	4	4.9 ± 0.48	2.7 ± 0.15	1.3	2.8	1.0	2.0
26	70	-5	3	6.5 ± 0.83	2.6 ± 0.15	1.4	2.5	3.0	1.0
27	60	0	4	5.9 ± 0.52	2.5 ± 0.10	1.9	3.5	1.0	3.0

$$Cpk = \frac{\mu - LSL}{3\sigma} \quad (9)$$

where μ is the average, σ is the standard deviation, and LSL is the lower specification limit i.e. the minimum acceptable limit for a specific response (stitch pull force, tail pull force). For the current case, the LSL for stitch pull force is considered as 3 gf, and the LSL for tail pull force is considered as 1.5 gf.

To compare the bond appearances, the optical micrograph of the samples before and after pull test are shown in Figs. 62 and 63, respectively, together with their stitch and pull force. The tested process parameters result in a variety of different stitch geometries. The scrub amplitude is an influential parameter on the stitch geometry, while bonding force and skid do not have a significant effect. In general, the larger the scrub amplitude, the larger the stitch bond size, especially in the direction of the scrub (perpendicular to wire). However, this increase in the stitch size does not automatically mean a stronger bond. Another observation is that with the -5 μm skid, there is a relatively weak bonded area which is broken with the tail breaking (stitch bond peeling). Increasing the skid to more positive values decreases the chance of such appearance in the bonds.

In general, a higher (more positive) skid decreases the stitch bond pull force substantially, increases the tail pull force substantially, decreases the chance of stitch bond peeling substantially, and increases the capillary tool mark imprint slightly. A larger bond force increases the stitch bond pull force slightly, increases the tail pull force slightly, decreases the chance of stitch bond peeling slightly, and increases the capillary tool mark imprint slightly. Finally, A larger scrub amplitude decreases the stitch bond pull force slightly, decreases the tail pull force substantially, decreases the chance of stitch bond peeling substantially, and increases the capillary tool mark imprint substantially. To select an acceptable stitch bond according to only the appearance one would look at the low capillary tool mark, and low peeling (sharp round cut at the tail area). Amongst the bonds, the bond made by 70 gf bond force, 3 μm scrub amplitude, and zero skid has the best appearance regarding the tool mark and the peeling severity.

The stitch bond pull remnants (Fig. 63) show a variety of different sizes as well. In general, increasing either scrub amplitude or bonding force, increases the size of the stitch bond pull

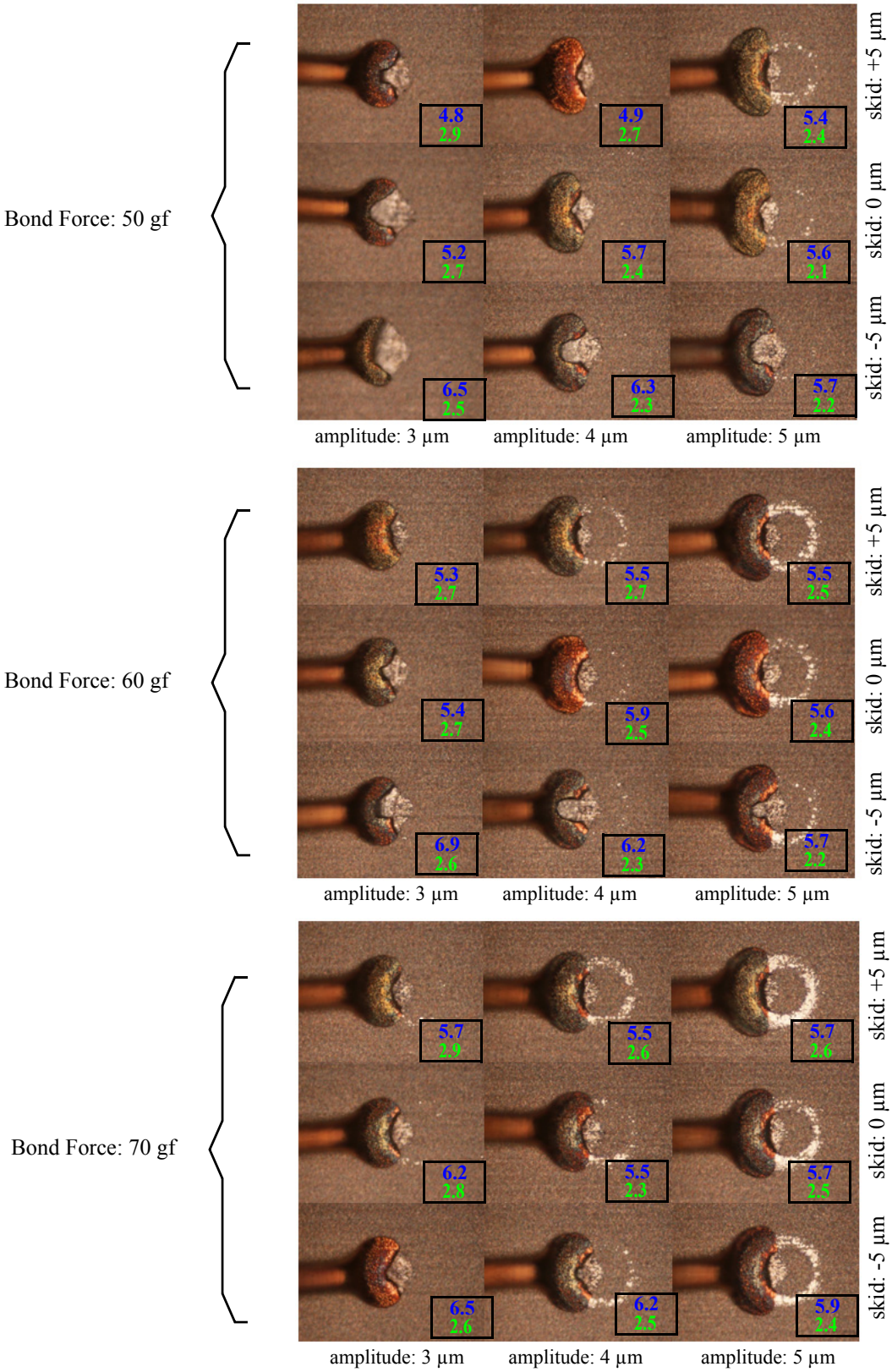

Fig. 62 Optical micrographs of stitch bond samples, before pull test. The blue number indicates the stitch pull force, and the green number indicates the tail pull force.

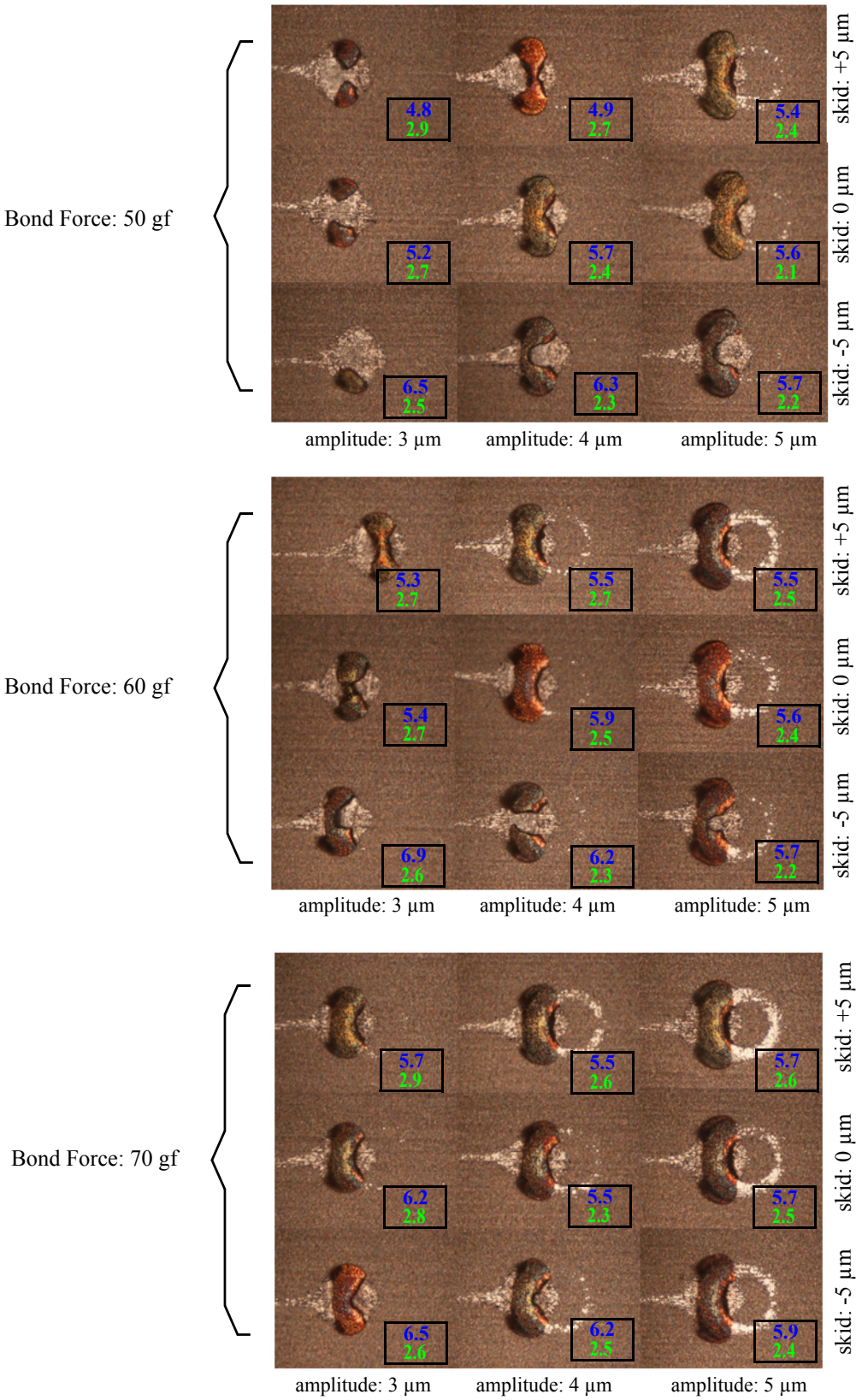

Fig. 63 Optical micrographs of stitch bond samples, after pull test. The blue number indicates the stitch pull force, and the green number indicates the tail pull force.

remnant. However this does not ensure a stronger bond at all. Indeed, high stitch bond pull forces are observed from both, samples with a small pull remain area and samples with a large pull remain area. This emphasizes the complex nature of the stitch bonding process. The remnants indicate that even for samples which result in low remnant and low stitch pull force, the peripheral regions of the interface (earings) are always bonded. This reveals that the stitch bond formation starts from the peripheral regions which contain the highest amount of deformation (expansion). The failure modes for samples bonded at minimum force and scrub amplitude (50 gf and 3 µm, respectively) is type E (stitch lift) which is not desirable. However, the rest of the samples result in failure mode D (heel crack). None of the samples result in type C (wire break).

3•2•3 Main Effects and Interactions of Process parameters

To further investigate the effect of process parameters on stitch bond quality (stitch and tail pull force) and considering the complexity of the process, a statistical analysis is carried out. For the statistical analysis, the Excel software (Microsoft^{TM}, Redmond, Washington, USA). Statistical analysis is important to understand to what extent each parameter could influence the bond quality, either by itself alone or in interaction with other parameters.

To find out the effect of process parameters on the process responses the main effects and second level interaction plots of the process responses are extracted and plotted. To extract the main (average) effects and interactions, the standard statistical approaches are used [102]. To calculate the effect of one parameter itself, all values of a specific response (e.g. stitch pull force) for samples bonded at a specific value of that parameter are averaged. To calculate the interaction effects, the same approach as with the main effect is followed with keeping another one the parameters constant during each calculation. For example, to analyze the interaction between force and skid, the stitch pulls of all samples with 50, 60, and 70 gf bond forces are averaged three times: first for samples with -5 µm skid, second with samples with 0 µm skid, and finally with samples with +5 µm skid.

According to the analysis of the main effects as shown in Fig. 64, the factor which is most influential on stitch pull force is skid. It results in largest change within its tested value range. In general, increasing the bond force increases the stitch pull. This increase is more significant when a larger value for positive skid is used. However, force and scrub do not have a signifi-

cant interaction regarding the stitch pull force. The more positive the skid, the weaker the stitch tail. This proportionality is more significant at lower values of force and scrub amplitude. Increasing scrub amplitude, can result in weaker stitch tail force. However, it is less significant if compared to the force and skid. There is a significant decrease in stitch tail, if a negative value of skid is used.

The statistical analysis of the effect of process parameters on tail pull force is shown in Fig. 65. The main effect plots show that the skid and scrub have the most significant effect on tail pull force, while the bond force is less significant. Increasing the bond force, slightly increases the tail pull. It seems that there is not a straight forward (or significant) interaction between force and skid or scrub. Increasing the skid level to more positive values significantly increases the tail force, regardless of the value of force or scrub amplitude. On the other hand, increasing the scrub amplitude decreases the tail pull force, regardless of skid or bond force. In general, there is more significant interaction between parameters considering the stitch pull force rather than the tail pull force.

To improve the statistical knowledge of the process, the main effects and interaction effects are plotted for pull force Cpk and tail pull force Cpk. They are shown in Figs. 66 and 67, respectively. For the stitch pull, increasing bond force at positive or zero skids improves the

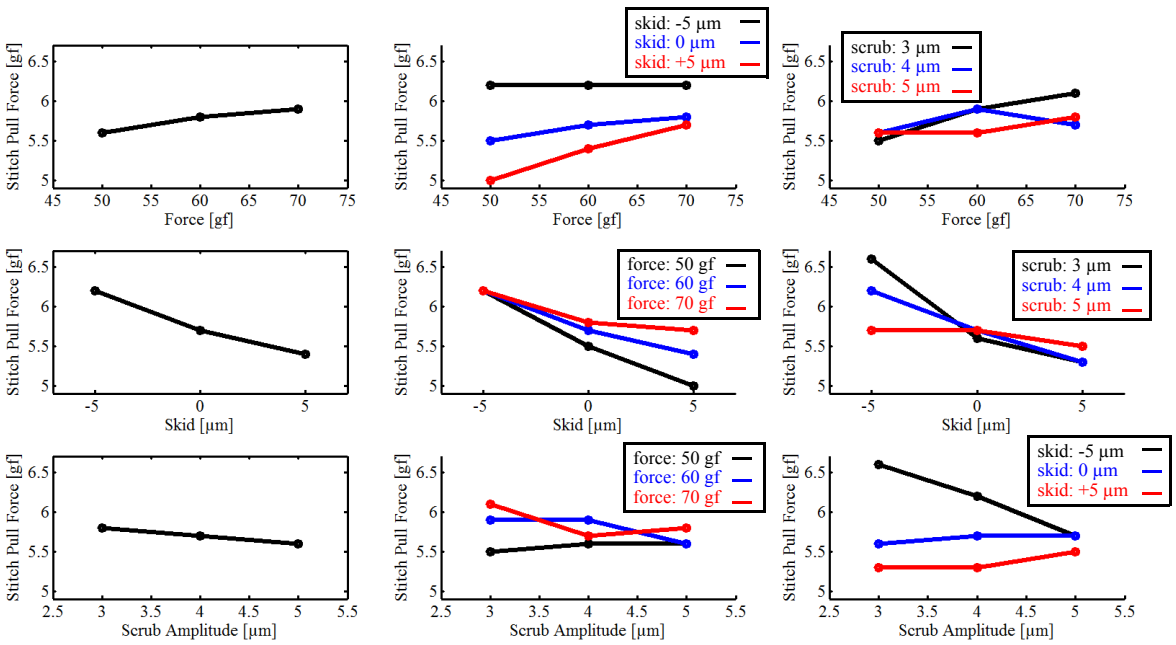

Fig. 64 Main effects and second level interaction effects of process parameters on the stitch bond pull force.

Cpk, however, a negative skid decreases the stitch pull force Cpk. In addition at moderate and high scrub amplitude the increase in bond force can degrade the pull force Cpk. Increasing skid, slightly decreases the pull force Cpk. However, a high force can reverse such trend.

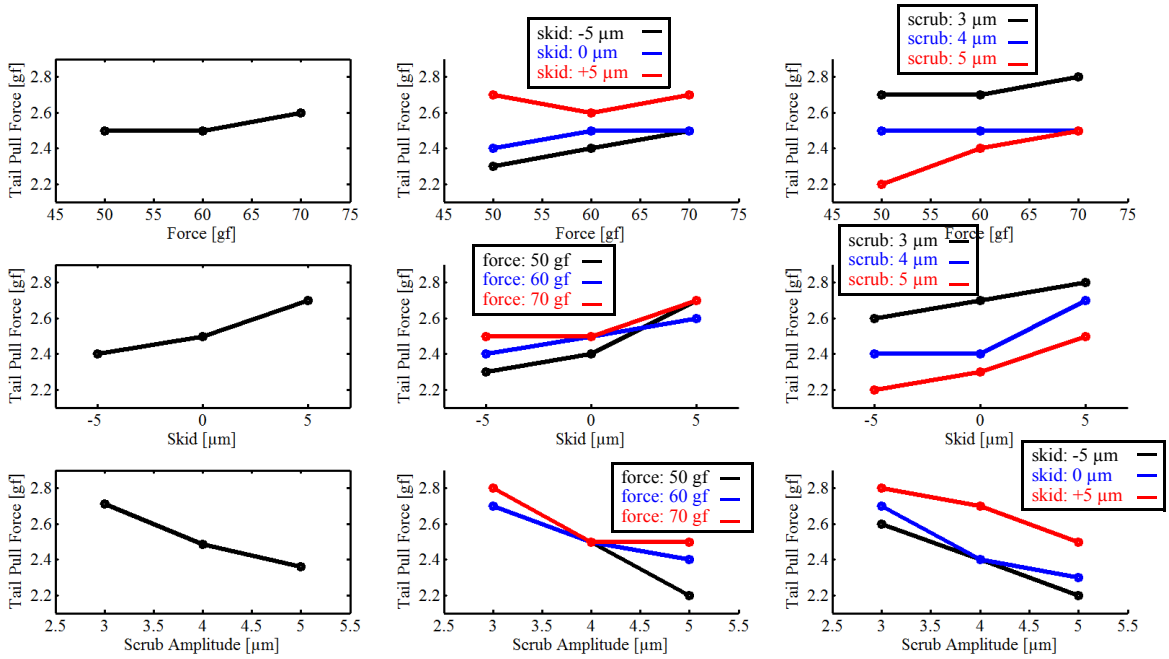

Fig. 65 Main effects and second level interaction effects of process parameters on the tail bond pull force.

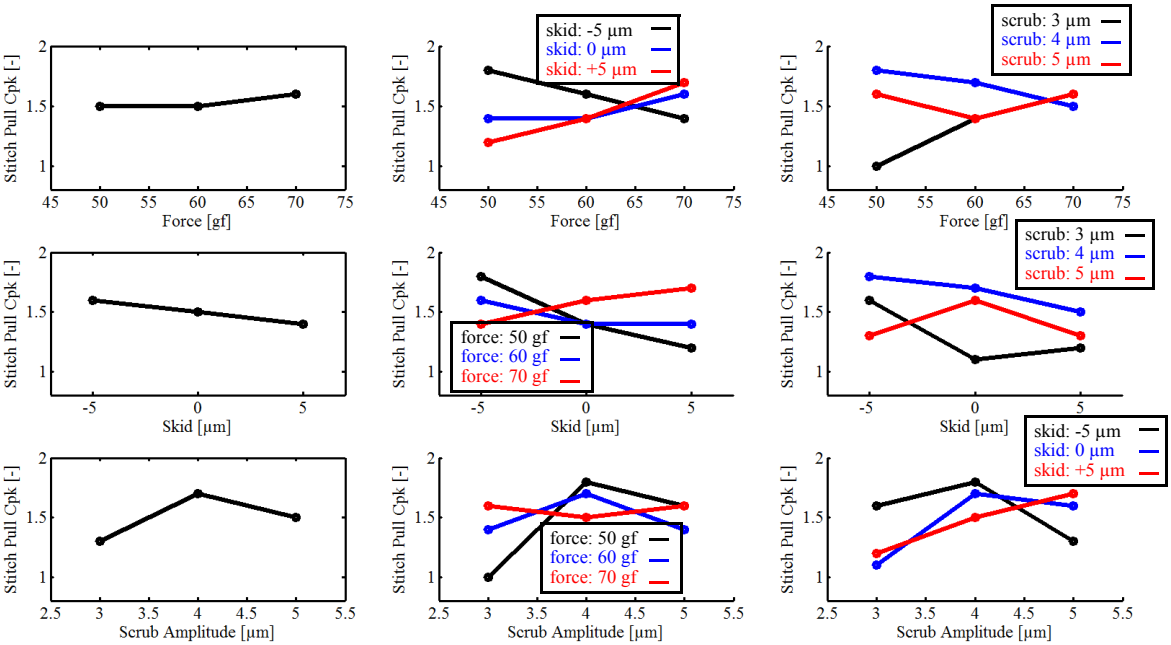

Fig. 66 Main effects and second level interaction effects of process parameters on the stitch bond pull force Cpk.

Between skid and scrub amplitude, there is no significant interaction regarding the pull force Cpk. Scrub amplitude has the most significant influence on pull force Cpk. It results in a maximum at the value of 4 µm. However, a high force, can degrade such dependency. In addition, at a high force, increasing scrub amplitude enhances the Cpk of the pull force constantly.

For the tail pull force Cpk as shown in Fig. 67 bond force has the least significant main effect. It enhances the tail pull force Cpk slightly. The interaction between bond force and skid regarding the tail pull force Cpk is not significant and the interaction between bond force and scrub amplitude is complex. skid has a significant main effect on tail pull force Cpk. There is maximum of tail pull force Cpk if no skid is used (skid = 0 µm). However, at low force, or a high scrub amplitude, such trend changes, and any increase in the skid will enhance the tail pull force Cpk constantly. The most significant main effect for tail pull force belongs to scrub amplitude, it significantly degrades the tail pull force Cpk. Only at a high bond force, there might be a slight improvement if the scrub amplitude increases from moderate values to high values.

The statistical analysis results of the effect of process parameters on the stitch bond peeling severity is shown in Fig. 68. Results show that increasing the bonding force and scrub amplitude reduce the peeling severity. The most significant parameter is skid. Increasing the skid

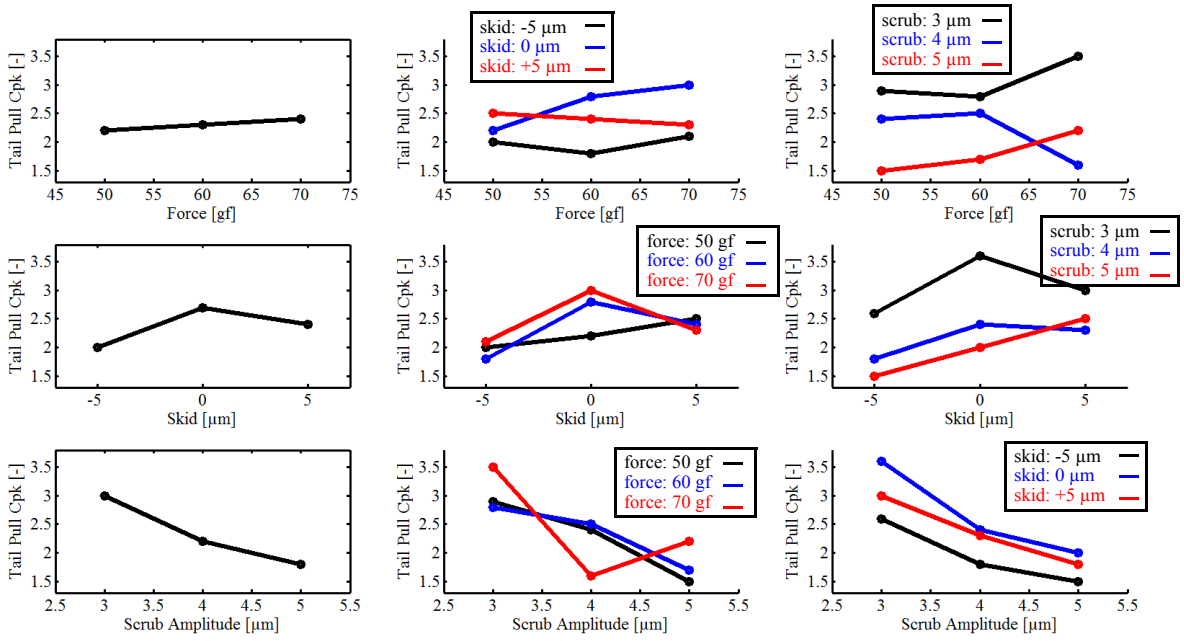

Fig. 67 Main effects and second level interaction effects of process parameters on the tail bond pull force Cpk.

value from negative to positive reduces the peeling severity significantly. No significant interaction effects is found between process parameters.

The statistical analysis results of the effect of process parameters on the capillary tool mark severity is shown in Fig. 69. Results show that increasing the bonding force slightly increases the tool mark. The skid is the least influencing parameter on the tool mark (almost has no effect). Scrub amplitude is the most influencing factor on the tool mark. Increasing the scrub amplitude increases the tool mark significantly.

3•2•4 Best Process Parameters Selection (Optimization)

In order to determine the best process parameters, as the first approach, the highest average Cpk of the tail pull force and the stitch pull force is considered as the selection target. Considering this target, the (however, these are not optimized) five cells are shown in Fig. 70. For comparison, the micrograph of the samples before and after the pull test are shown as well. The top three cells result in formation of the stitch bonds which show minimum or very low bond peeling at the tail area. However, the fourth cell results in severe bond peeling which reduces the process reliability, and the fifth cells make a heavy capillary tool mark impression on substrate, which is not desirable, as it decreases the capillary lifetime.

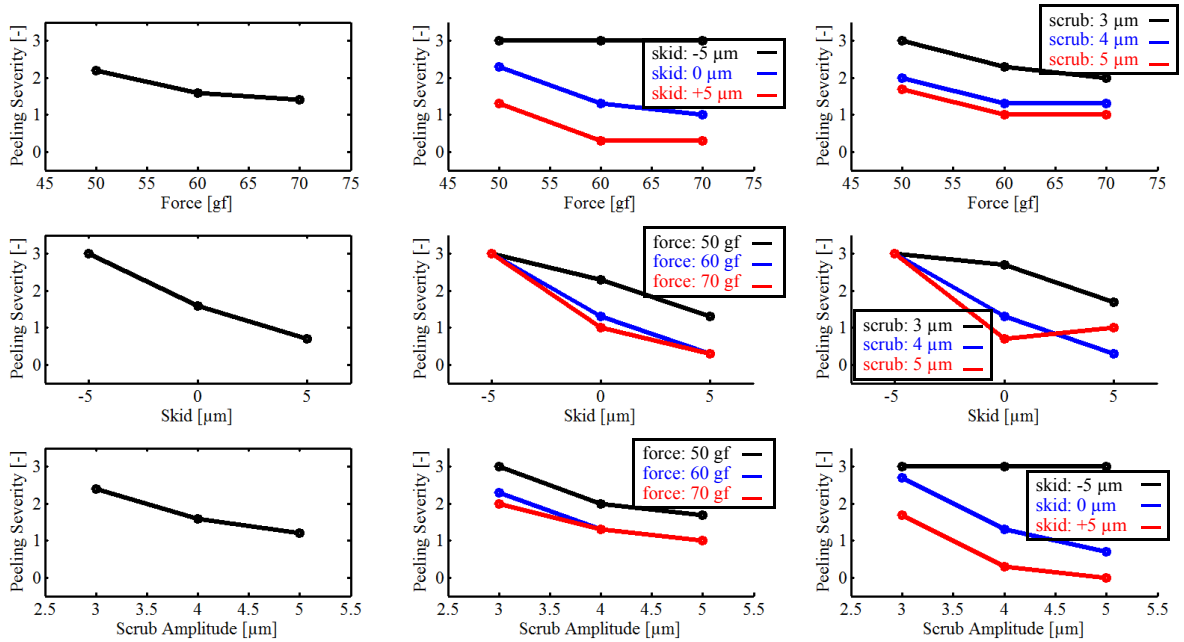

Fig. 68 Main effects and second level interaction effects of process parameters on the stitch bond peeling severity.

As an alternative approach to estimate optimum parameters, the multivariate response surface methodology (RSM) is used [103]. To perform a RSM analysis, the JMP software (JMP statistical Discovery from SAS, Cary, NC, USA) is used. The DOE cells, and Cpk of the responses are used to build up a RSM analysis model. For each response a fitting is performed by using JMP software according to the formula shown below:

$$Response = A \times force + B \times skid + C \times scrub + D \times force \times force + \tag{10}$$

$$E \times force \times skid + F \times force \times scrub + G \times skid \times skid + H \times skid \times scrub +$$

$$I \times scrub \times scrub$$

where response could be either stitch and tail pull force and Cpk, tool mark, and peeling severity, and the A to I are the fit coefficients. The effect of process parameters on tail pull force Cpk and stitch pull force Cpk modeled with RSM method are shown in Fig. 71. The

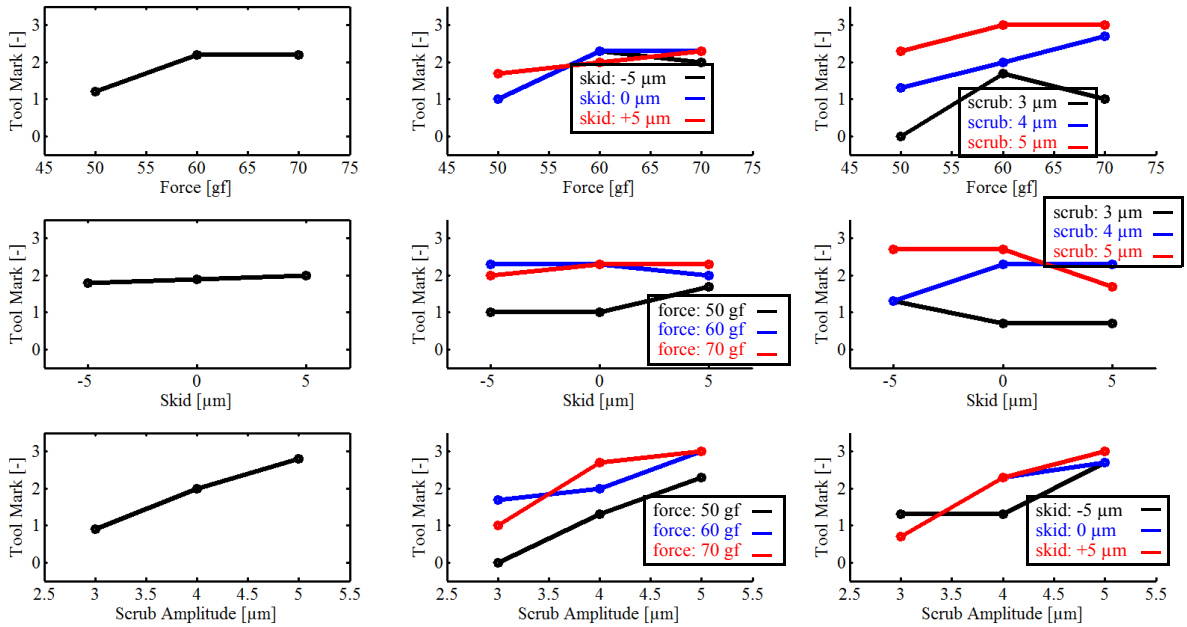

Fig. 69 Main effects and second level interaction effects of process parameters on the capillary tool mark severity.

actual values versus RSM predicted values for stitch pull force Cpk and tail pull force Cpk are shown in Figs. 71 (a) and (b), respectively. The diagonal solid red line means a perfect RSM fit between experimental and RSM predicted values, and so the closer the dots to the solid red line, the better the fitting. The goodness of the fit can be checked by the RSq (R-Squared) value too, and it is provided for each case. The closer the RSq to 1, the better the fit.

To find the optimized process parameters two desirable targets are defined in the JMP software based on the RSM analysis of DOE data. The desirable outputs include the stitch pull force Cpk and tail pull force Cpk. Next, these targets are maximized by JMP based on the RSM method, as shown in Fig. 72. The optimized parameters found are 70 gf bond force, 0.5 µm skid, and 3 µm scrub amplitude.

For comparison, the same type of RSM analysis is repeated with the values of stitch pull force and tail pull force, and the results are shown in Figs. 73 and 74. This second RSM attempt results in optimized parameters of bond force 70 gf, -5 µm skid, and 3 µm scrub amplitude.

Finally, the RSM analysis is repeated with the values of peeling and tool mark severity, and the results are shown in Figs. 75 and 76. This third RSM attempt results in optimized parameters of bond force 70 gf, 5 µm skid, and 3.05 µm scrub amplitude.

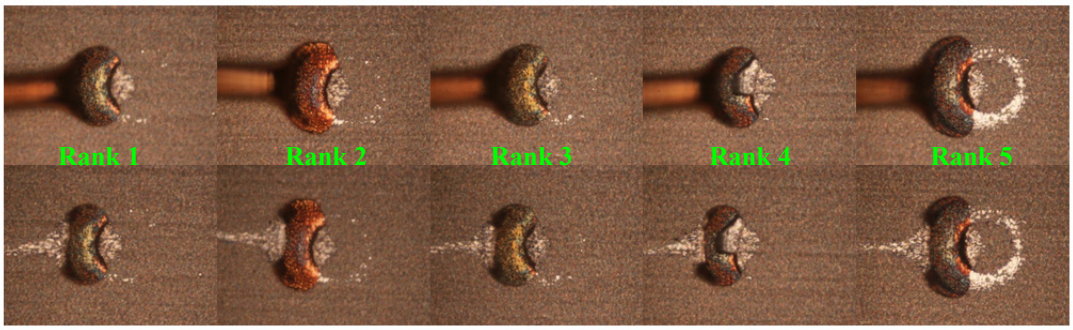

Rank	Force [gf]	Skid [µm]	Scrub Amplitude [µm]	Peeling Severity	Tool Mark	Cpk Stitch	Cpk Tail	Cpk_Average
1	70	0	3	2	1	1.8	4.8	3.3
2	60	0	4	1	3	1.9	3.5	2.7
3	70	5	3	1	3	1.5	3.2	2.4
4	60	-5	3	3	3	2.0	2.5	2.2
5	70	0	5	0	3	1.7	2.7	2.2

Fig. 70 Best of the process parameter sets based on average Cpk of stitch pull force and tail pull force. Micrographs of typical bonds obtained with the five sets of process parameters are shown as well.

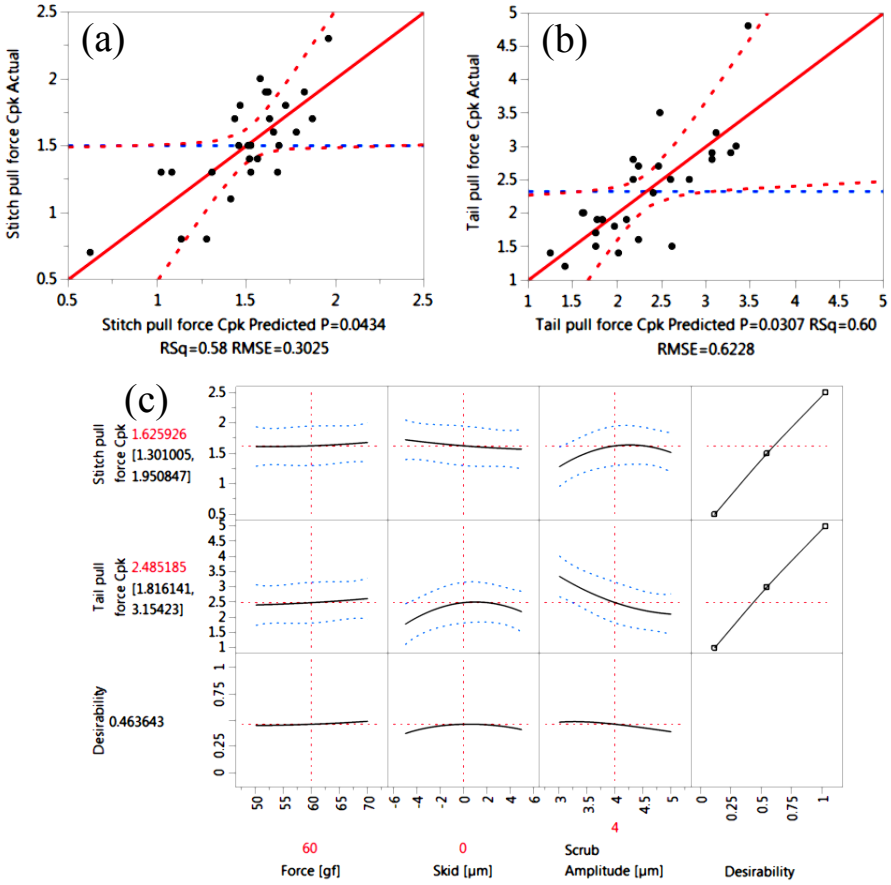

Fig. 71 RSM analysis of stitch pull force Cpk and tail pull force Cpk. (a) Stitch pull Cpk actual vs. predicted (b) Tail pull force actual vs. predicted, and (c) effect of process parameters on stitch and tail pull force Cpk.

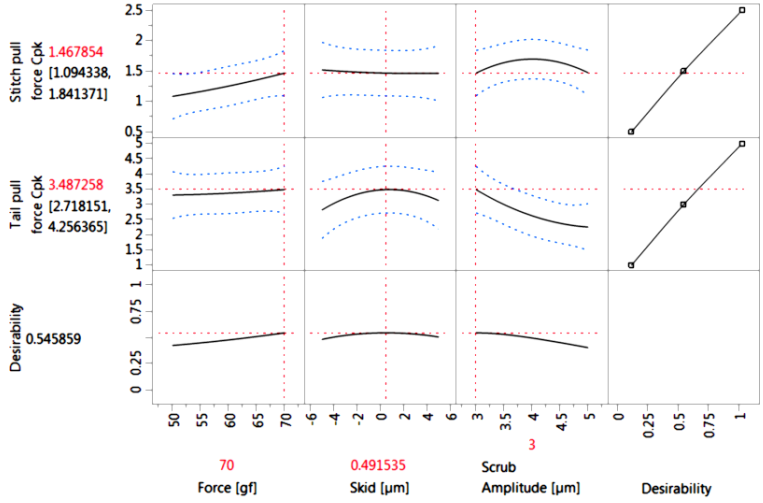

Fig. 72 Optimization of process parameters in order to maximize the tail pull force Cpk and stitch pull force Cpk, using RSM method by JMP software. The optimized parameters are 70 gf bond force, 0.5 µm skid, and 3 µm scrub amplitude.

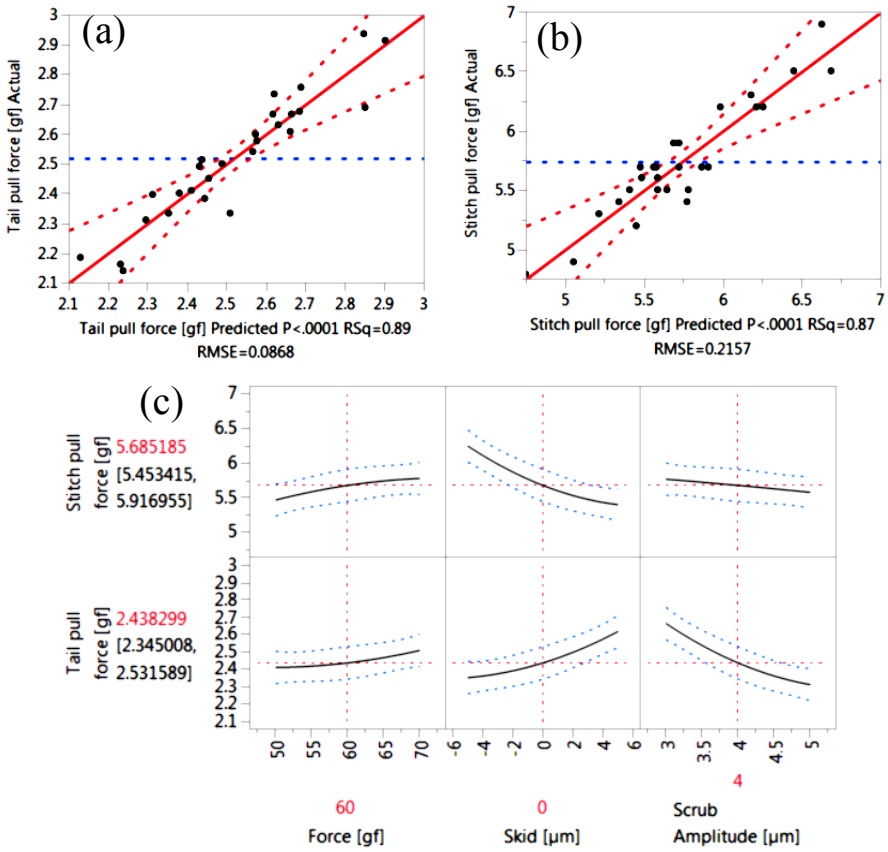

Fig. 73 RSM analysis of stitch pull force and tail pull force. (a) Stitch pull actual vs. predicted (b) Tail pull force actual vs. predicted, and (c) effect of process parameters on stitch and tail pull force.

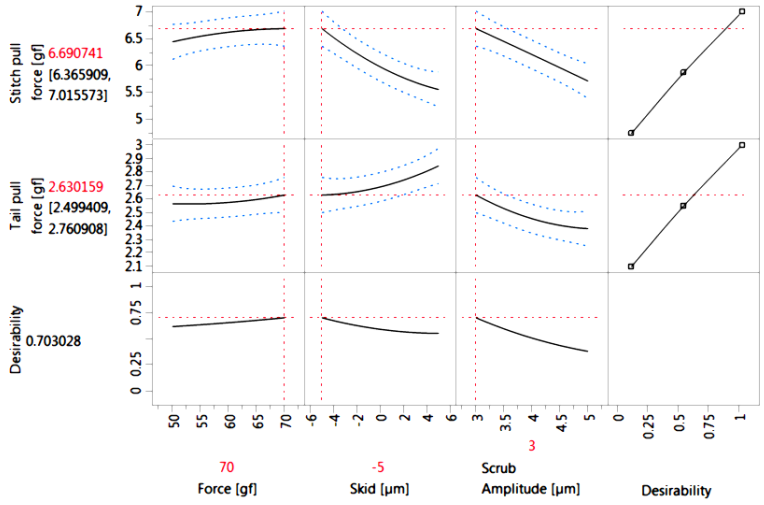

Fig. 74 Optimization of process parameters in order to maximize the tail pull force and stitch pull force, using RSM method by JMP software. The optimized parameters are 70 gf bond force, -5 µm skid, and 3 µm scrub amplitude.

All of the three RSM optimization approaches result in almost the same optimized bond force (70 gf) and optimized scrub amplitude (3 µm). In other words, it shows that a parameter set

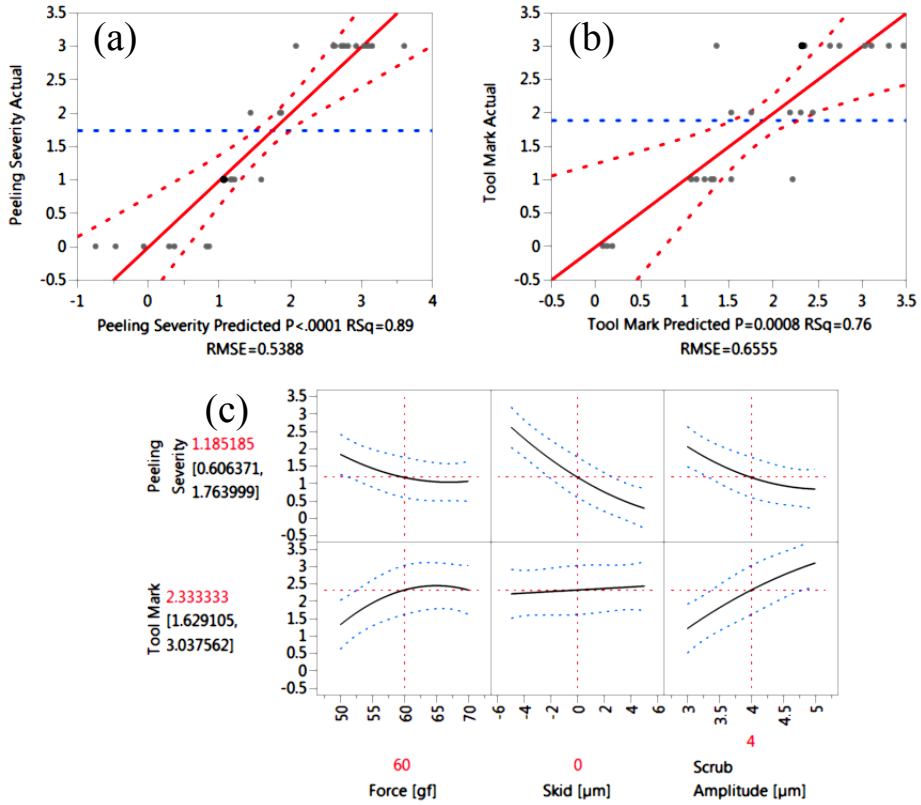

Fig. 75 RSM analysis of peeling severity and tool mark severity. (a) peeling severity actual vs. predicted (b) tool mark severity actual vs. predicted, and (c) effect of process parameters on peeling severity and tool mark.

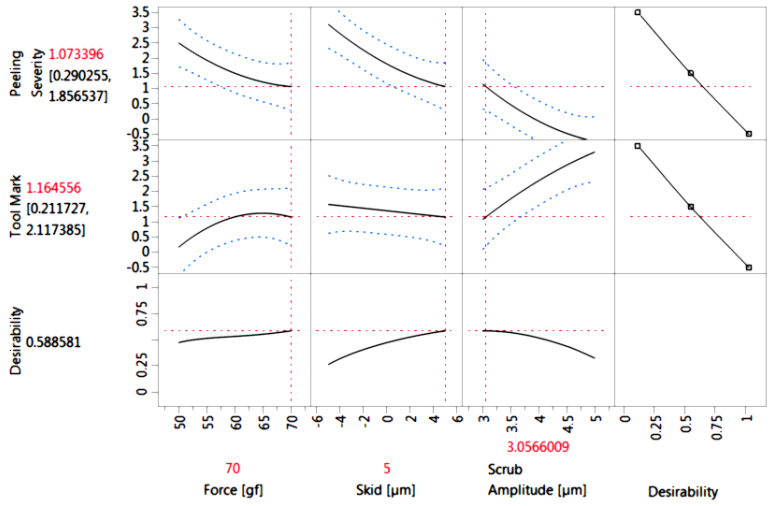

Fig. 76 Optimization of process parameters in order to maximize the peeling and tool mark severity, using RSM method by JMP software. The optimized parameters are 70 gf bond force, -5 µm skid, and 3 µm scrub amplitude.

containing a high force and low scrub amplitude results in the best process output. To investigate the effect of skid at these specific values of bond force and scrub amplitude, the stitch pull force and tail pull force at various skids, and the stitch pull force Cpk and tail pull force Cpk are plotted in Fig. 77. According to Fig. 77, within the specified range of process parameters, increasing skid from negative to positive values decreases the stitch pull force and increases the tail pull force. However, the Cpk of stitch pull force, and the Cpk of tail pull force have a maximum at skid equal to zero. This means, if the skid value is selected at zero, the process is less sensitive to slight variations in the process parameters, tools, machine, etc. In other words, there is a safer process if the skid value is selected to be zero. The stitch bond appearance is shown in Fig. 77 (e). As it can be seen, the skid of -5 µm shows slight peeling, which is not recommended as it could influence the process reliability. Therefore, it could be concluded that the bond force of 70 gf, skid of 0 µm, and scrub amplitude of 3 µm is the best

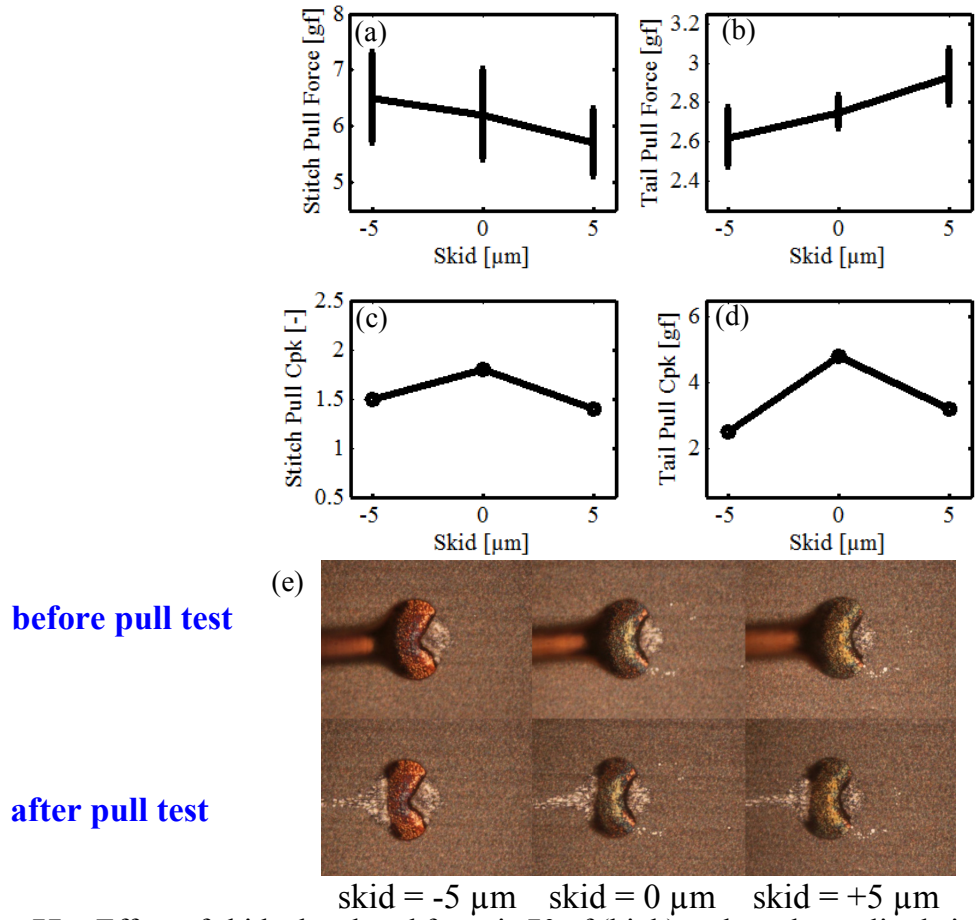

Fig. 77 Effect of skid when bond force is 70 gf (high) and scrub amplitude is 3 µm (low). (a) stitch pull force vs skid, (b) tail pull force vs skid, (c) stitch pull force Cpk vs skid, (d) tail pull force Cpk vs skid. (e) Micrograph of process parameter sets.

optimized process parameter set for the current bonding materials resulting in high stitch pull force and tail pull force Cpk, low peeling, and low tool mark.

3•3 Discussion

With the first DOE, the effect of the bonding process on sticking and tail lifting of stitch bonds made with PCC wire on a low bondability substrate of Au-plated QFN is investigated. The results showed that a higher force, a higher scrub amplitude, and a more positive skid increase the chance of sticking the wire to the substrate. Based on the cold-welding mechanism, a combination of these parameters has possibly resulted in the highest levels of surface expansion and surface cleaning. In addition, the same trend of process parameters encourage the tail lifting within the sticking stitch bonds. On the other hand, with the second DOE, the effect of the same process parameters are investigated with bare Cu wire on a Ag-plated QFN which is a high bondability substrate. The results of the second DOE showed some similarities and some differences with the first DOE. For example, similar to DOE 1, a higher bond force increases the stitch pull force (higher sticking), or increasing the scrub amplitude decreases the tail pull force (higher chance of tail lifting). However, there is a difference in the effect of skid. In contrast to the situation in DOE 1, in DOE 2 increasing the skid decreases the stitch pull force (less sticking), and increases the tail pull force (less chance of tail lifting). This means that the combination of wire type and substrate type can substantially influence the effects of the process parameters and their interactions with each other. The differences can arise from either the differences in the hardness of the wire and the substrate materials which result in different surface expansions at the interface, or from different friction coefficients which result in different interface cleaning. Possible tests for better checking of this hypothesis could be using for example an exactly similar substrate, and using wires with exactly similar diameter and surface (friction coefficient) but with a different hardness.

For comparison, an example stitch bond process window reported previously is shown in Fig. 78. It was obtained with 18 µm Au wire on Al bond pad. It indicates that for the ranges of the bond forces and ultrasonic powers, the stitch pull force is varying between 4 to 5 gf. However using bond force, scrub, and skid in the current optimization bonds with 18 µm Cu on QFN, high stitch pull forces between 5 to 7 gf are achieved. It indicates that scrub and skid parameters are successfully able to replace ultrasonic energy if optimized properly.

In conclusion, test I was able to provide information about how the process parameters could define the bondable region, regardless of the bond quality. This information can help the process engineers to pick proper process parameter combinations to run a detailed optimization test. Test II included a DOE for an optimization study of the stitch bond process. The target of such an experiment is to find the best process parameters. Through the optimization study including the determination of response surfaces, the best parameter sets which ensure a successful stitch bond process are found. In addition, by using a statistical analysis, the main effects and the interaction effects between process parameters are calculated and discussed. This information is helpful regarding the development of a systematic procedure for enhancing the stitch bond quality.

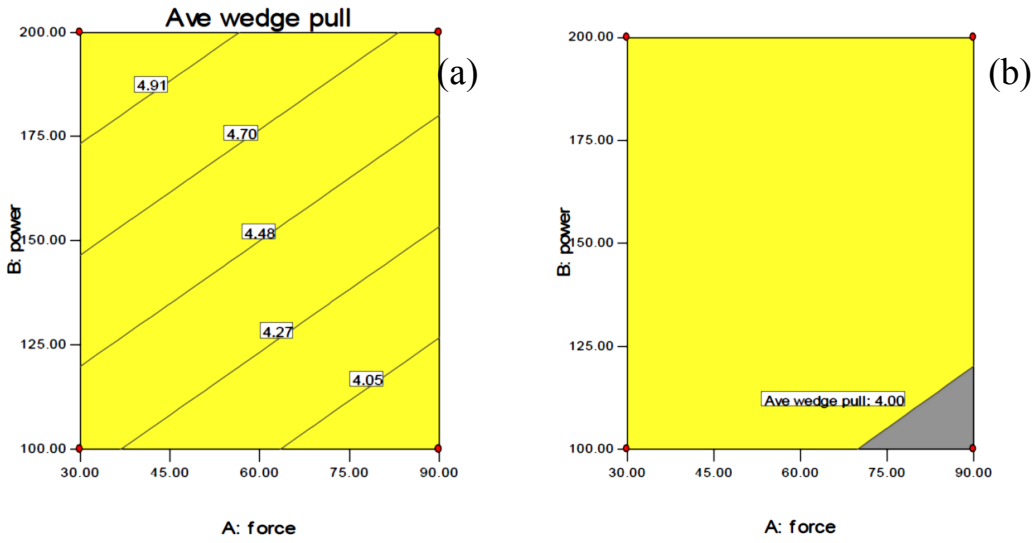

Fig. 78 Process window of 18 µm Au wire stitch bonding on Al substrate. (a) Variation of wedge (stitch) pull force versus bond force (gf) and ultrasonic power (mA), and (b) Process window for stitch bonds with stitch pull force greater than 4 gf [104].

4 Finite Element model of Stitch Bond, Part I: Development

In this chapter, a finite element (FE) model of a stitch bond process is developed. To develop such a model, some assumptions and limitations such as absence of thermal and chemical analysis are considered. The model components are made based on the common components used in the stitch bonding process. For sections which require experimental data (such as mechanical properties of parts, and friction coefficients), the appropriate experimental procedure is performed and the results are used. The modeling steps, loads, and boundary conditions are developed based on experimental steps of stitch bonding. Next, the meshable parts are meshed with appropriate techniques. Finally, the model is checked to ensure avoiding unwanted artificial inertia effects, and an example deformed model of stitch bond is provided.

4•1 Introduction

The stitch bond process is a complex process which requires careful and precise control of process parameter selection/optimization to ensure safety and robustness. The complexities with the different process parameters has been limiting researchers to understand the root causes of the successful or unsuccessful bonding outcome. FE analysis has been known as an effective tool for analyzing the process including structural changes. In this work, it is planned to use the FE analysis to improve the current knowledge with the stitch bonding process. The results of this work could be used for other similar processes as well.

A three dimensional (3D) model is chosen over a 2D model to better reflect the complexities of the geometry of the stitch bond. ABAQUS^{TM} CAE (version 6.10, SIMULIA, Providence, Rhode Island, United States) software is selected for developing the numerical model of the process. A complete model of the process would include the complete ultrasonic transducer, including horn, the capillary, a long enough piece of wire, and the complete substrate and the underlying tape material. Such a model is illustrated in Fig. 79 (a). To reduce the model size and increase the modeling speed, only the capillary tip, a short piece of wire, and a piece of substrate are considered as shown in Fig. 79 (b).

4•2 Model Goals

The goals of the finite element model developed in this work are first to find a correlation between numerical responses and experimental observations, and second to reproduce process windows for stitch bonding, and to study the effects of process parameters, materials, geometries, and etc. In this work, it is planned to achieve the following goals,

1. Develop a 3D FE model of a stitch bond process
2. Extract model outputs
3. Analyze model output and build up candidate responses
4. Compare candidate responses with experimental observations and make correlations

4•3 Model Components

The components of the model are shown in Fig. 80. As the capillary is made of alumina, it is possible to consider it a non-deformable part (analytical rigid, no mesh required). Therefore the modeling efforts are done with this assumption. This model includes a piece of wire, a

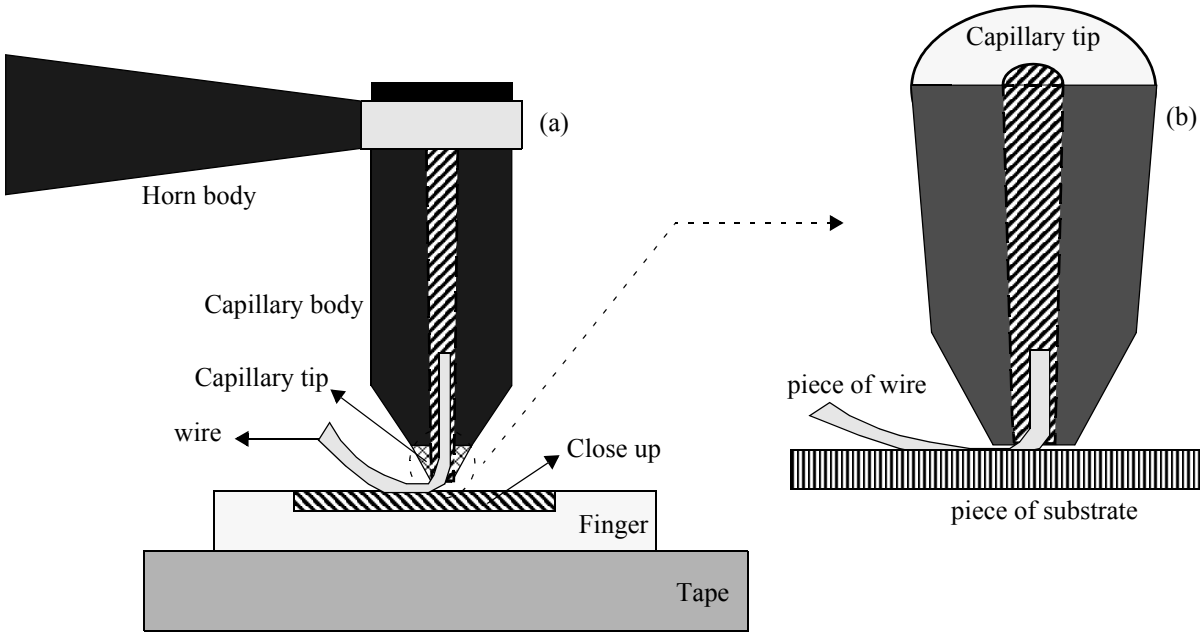

Fig. 79 (a) Complete set of components of the stitch bond process (b) Simplified model of the stitch bond process, used in this work.

piece of substrate, and the capillary tip. As an analytical rigid body, the capillary does not require material properties such as elastic modulus. It can be represented (defined) with a reference point, and all the loads and boundary conditions are applied to this reference point. The capillary is made by 360 ° revolution of its section design. As required for the dynamic explicit module, the mass of the capillary tip part has to be calculated and entered as the inertia factor. Therefore, the volume of the capillary part is calculated mathematically and multiplied by the density of alumina (4 g/cm^3). The volume obtained is 1.73 × 10^5 μm^3.The mass (inertia) is then applied to the reference point of the capillary part. The wire is a three dimensional deformable solid constructed using the "sweep" function of ABAQUS. The wire diameter is 18 μm. The design of the capillary and wire parts are shown in Figs. 81 (a) and (b), respectively. Finally, the substrate is made by using the "extrusion" function of ABAQUS. The thickness of the substrate piece is 10 μm. The pictures of the capillary tip, wire, and substrate parts are shown in Fig. 82. To include in the model, the parts are assembled independently within the assembly module.

4•4 Model Simplifications

Four types of model simplifications are used:

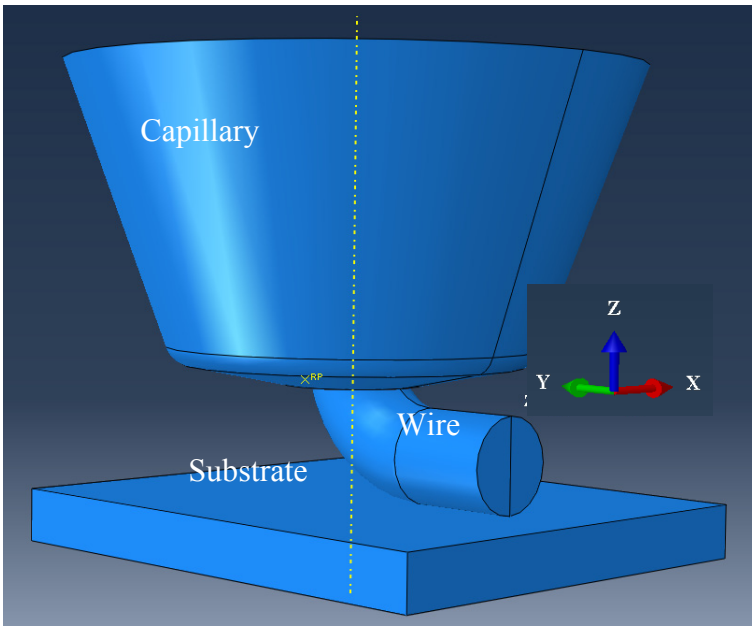

Fig. 80 Components of FE model of stitch bond.

1. *Reduced set of model components*. Capillary tip, wire piece, and substrate piece are considered as the process components instead of the hole bond head. The limitation coming with this assumption is the impossibility of considering the stiffnesses of the bonding horn and whole capillary body, and therefore the impossibility of the effect of bonding direction on the model outputs. In addition, the capillary is considered as a rigid body in the current model and so if there are small displacements at the capillary tip, they will not be

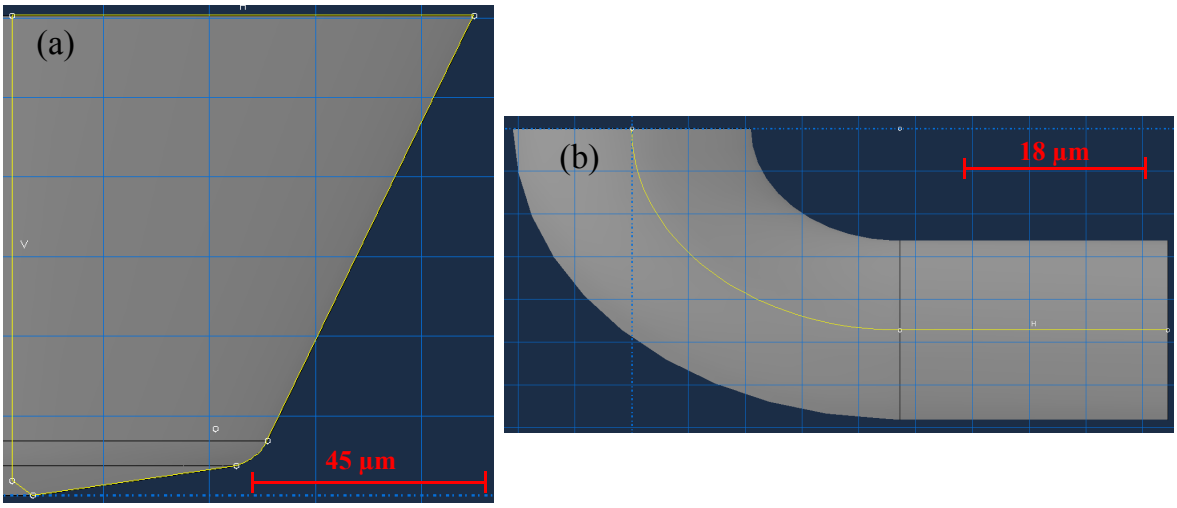

Fig. 81 Screen-shots of parts design for FE model. (a) Capillary tip, (b) wire part.

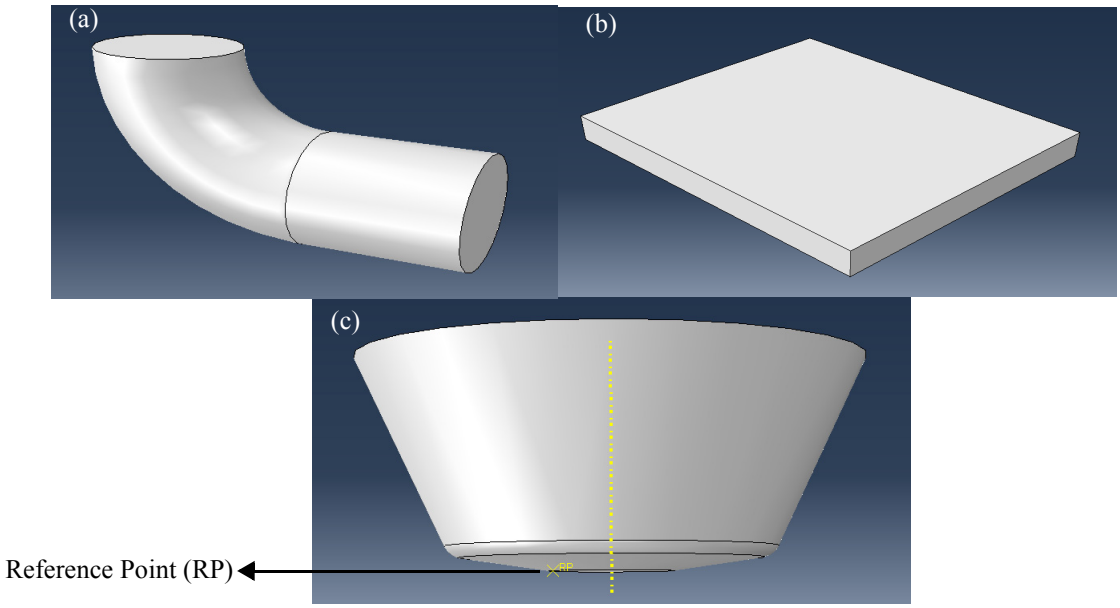

Fig. 82 (a) wire (b) substrate (c) capillary, with its reference point.

reflected. This will limit the model from having the possibility of analyzing capillaries with variable stiffnesses.

2. *Absence of thermal, chemical, and metallurgical analysis.* Therefore, the bond quality in this model cannot be represented with metallurgical adhesion directly, and cannot predict deformations due to the temperature. In addition, the effect of inclusion of different elements cannot be reflected in the results.

3. *Absence of thin films.* The plated layer on top of the QFN substrate are only modeled as a different friction coefficient, and not as an individual part. This assumption is based on the fact that such a coating is significantly thinner than the bulk Cu QFN substrate (less than 0.05%). This assumption might not be valid if a thicker top plated layer is used.

4. *Absence of ultrasonic vibration.* This will limit the model to only the processes without ultrasonic such as those used for QFN substrate, and cannot predict deformations due to ultrasonic vibration.

4•5 Properties of Materials and Contacts

4•5•1 Mechanical Properties

For the capillary part, no mechanical properties are considered. For wire and substrate, the mechanical properties (elasticity and plasticity) for PCC wire and Cu wire are taken from tensile testing and implemented into the model. The elastic (Young's) modulus, plastic stress, and plastic strains are extracted from the test results. The uniaxial tensile test machine (Instron, Norwood, MA, United States of America) custom designed for micron sized wires is shown in Fig. 83 (a). Two special grippers are holding the wire at its two ends and apply tensile force. The gage length of the wire used is 28 cm. This relatively long gage length is selected mainly to ensure a successful tensile test as it is helpful for a defect-less sample preparation. A short gage length needs extra care and there is a high chance of causing initial deformation at the two ends of the wire prior to the test initiation.

The raw data is in the form of load-displacement. To convert the data into the conventional form of stress-strain,

Engineering Strain = (Displacement) / (Gage Length) *(11)*

Engineering Stress = (Load) / (Wire cross section area) *(12)*

are used. An example stress-strain curve for PCC wire at a displacement rate of 100 mm/min is shown in Fig. 83 (b). The mechanical properties of the PCC wire is extracted from five tensile tests and the resulting average values for Young's modulus and yield stress are shown in Table 5. The plastic properties table used in the ABAQUS software is extracted from five tensile tests and shown in Table 6. As the PCC wire is coated with only a thin layer of palladium (about 100 nm thick), its bulk properties are considered similar to that of bare Cu wire.

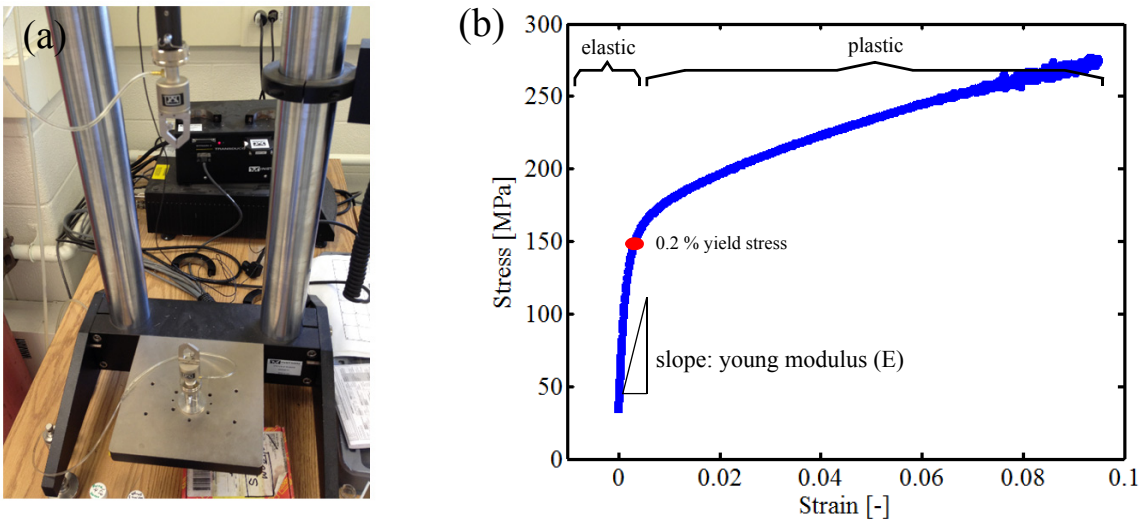

Fig. 83 (a) tensile test machine (b) tensile test result of PCC wire at 100 mm/min displacement rate.

Table 5: Mechanical and physical properties of parts used in the model

Material	Elastic Modulus (E)	Yield Stress	Density [105]	Poisson Ratio [105]
PCC and Cu	120 GPa	140 MPa	8.9 g/cm^3	0.35

Table 6: Plastic properties table used in ABAQUS for PCC wire and Cu substrate

Plastic Stress [MPa]	140	170	200	245	265	350	430	510	590
Plastic Strain [-]	0	0.008	0.03	0.075	0.1	0.2	0.3	0.4	0.5

4•5•2 Contacts and Friction Coefficients

The stitch bonding process includes three different contact surfaces. They can be characterized using their friction coefficients μ_1, μ_2, and μ_3. The first surface is defined between wire and capillary (μ_1), the second between wire and substrate (μ_2), and the third between capillary and substrate (μ_3). In ABAQUS, contact between parts is introduced in the interaction module. The "surface to surface" kinematic contact method is used for all three surfaces. The other options for contact definition in ABAQUS are "general contact" and "penalty" contact method. However, the "surface to surface" contact method is preferred for models containing analytical rigid parts as recommended in the ABAQUS software manual [106]. The "penalty" contact property is used for the tangential behavior of the contacts, and the "hard contact" property is used for the normal behavior of the contacts. The different contact parts defined in the model are coded with red and purple color as shown in Figs. 84 (a) - (c). In all contacts, the red surface is the master surface, and the purple surface is the slave surface.

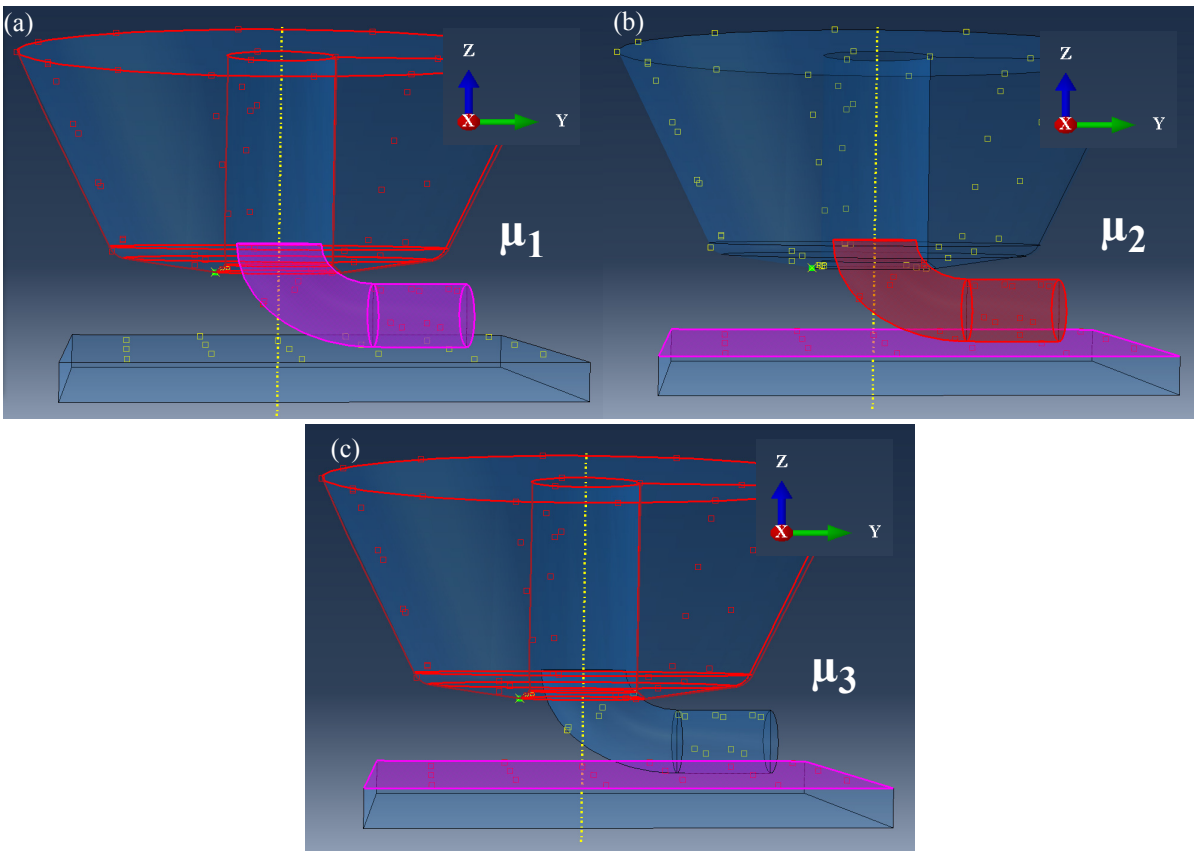

Fig. 84 Three contact pairs defined in the model. (a) capillary and wire, (b) substrate and wire, and (c) capillary and substrate.

The friction coefficient values needed for the model are measured through a custom designed test setup suitable for small samples [108]. The principles of the measurement are based on inclined plane method described in the ASTM 4516-91 standard [109], and is illustrated in Fig. 85 (a). A photo of the developed setup is shown in Fig. 85 (b). The setup has a heated surface developed in [111]. A power supply is used to generate temperature of up to 200 °C is used in a typical stitch bonding process. The samples are placed on the heated inclined plane in couples of one top and one bottom part. The inclined plane is then manually raised up gradually from the flat condition to larger angles using the set screw. At the onset of sliding (when the top part starts to move with respect to the bottom part), the friction coefficient between the top part and the bottom part is equal to the tangent of the current inclined plane angle (Θ):

$$\Theta = \operatorname{asin}\left(\frac{\text{height}}{\text{length}}\right) \tag{13}$$

$$\mu_s = \tan\Theta \tag{14}$$

For the sliding test, wire samples are made by bonding 100 wire loops beside each other to simulate a flat surface made of the wire material. Capillary samples are made by gluing four capillaries sideways next to each other onto an auxiliary substrate. Substrate samples are cut from QFN substrates. Example samples for wire, capillaries, and substrate are shown in

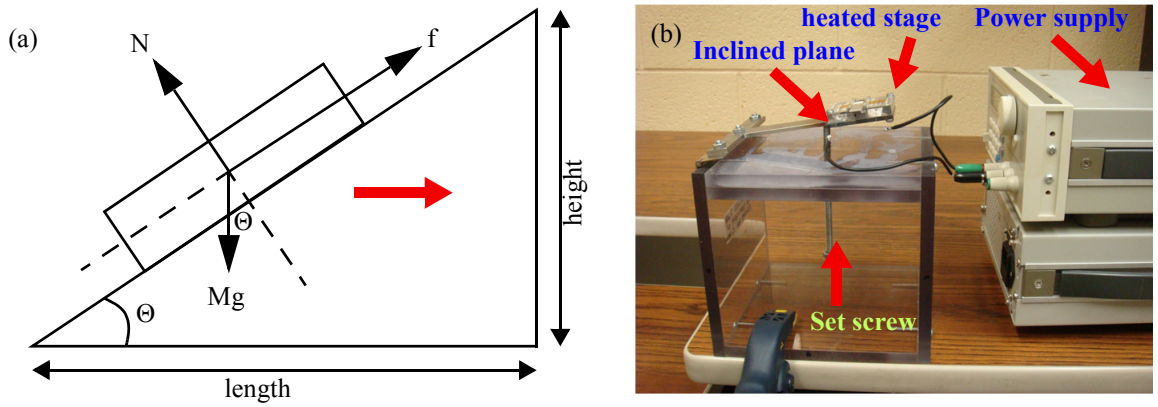

Fig. 85 (a) Illustration of inclined plane principle for friction coefficient determination, where N is normal force to inclined plane, f is friction force, M is mass, g is gravity, and theta at the sliding transition is used for the friction coefficient determination. (b) photograph with inclined plane and power supply for heating of inclined plane.

Figs. 86 (a), (b), and (c), respectively. The measured friction coefficients for different sample combinations are shown in Table 7. These values are the same as published in [110]. Friction coefficient values of more material combinations can be found in [110 and 111].

4•6 Transient Boundary Conditions

4•6•1 Modeling Steps

Due to the dynamics of the cyclic scrubbing, the dynamic explicit module of ABAQUS is selected. As the process of stitch bonding contains a relatively large deformation, the explicit type of the solver is used, as recommended in the ABAQUS software manual [106]. Using explicit method instead of implicit method speeds up the simulation significantly, but it requires extra care.

The stitch bonding process is divided into three steps as shown in the schematic bonding steps in Fig. 87. The original bonding signals are omitted due to confidentiality but could easily be replaced by signals from any wire bond machine commercially available. The first step is the

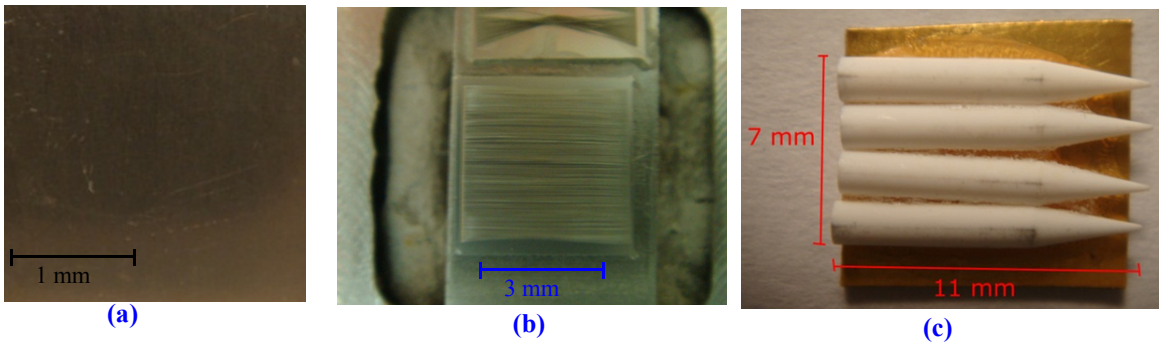

Fig. 86 Example samples used in friction coefficient test (a) QFN substrate, (b) PCC wire bonded sample, and (c) Capillary.

Table 7: Friction coefficient between different counter parts [81]

Material Pair	PCC wire and QFN substrate	PCC wire and alumina capillary	QFN substrate and alumina capillary
Friction coefficient	0.4 ± 0.25	0.5 ± 0.25	0.5 ± 0.25

"touch down" step. In the experiment, the constant contact velocity (CV) used in this step before the detection of touch down (impact) is 0.3 mil/ms (7.62 µm/ms). CV is used in the wire bonding machine to move down the capillary with a constant reduced speed before detecting the contact between capillary and bonding surface. The machine detects the contact by observing either a change in motor current, a discrepancy between target and measured z position, or a dedicated touchdown sensor signal. Usually, contact detection is followed by an impact force acting on the wire before the bonding (scrubbing) segment starts. In the numerical model, no impact sensor can be implemented so the capillary is descending towards the wire due to an increasing acceleration force (impact force). The impact force is acting for 3 ms and no scrub or skid is applied. To find out the correct impact force value to reproduce the specific CV used in the experiment, signals of the wire bonding machine can be used. It is possible to find the impact force corresponding to CV of 0.3 mil/ms by

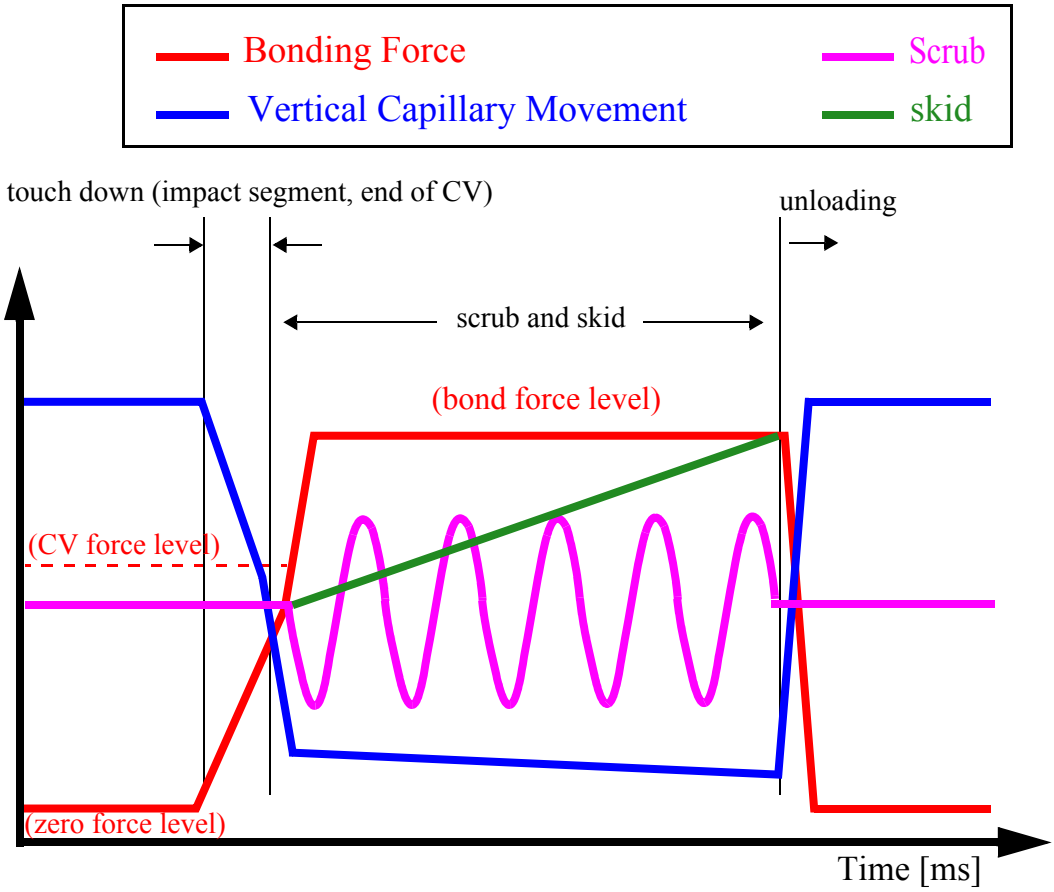

Fig. 87 Schematic bonding steps.

$$ImpactForce_i = \frac{F_{CV} - F_0}{F_B - F_0} \cdot B \tag{15}$$

where F_{CV} is the level of the CV force signal, F_B is the level of the bond force signal, F_0 is the level of the zero force signal (the voltage reference for zero gram force), as shown in Fig. 87. B is the nominal (experimental) bond force level (not the value of signal). Performing such a calculation for example bond forces of 60 gf, 80 gf, and 100 gf results in impact force values of 24.3 gf, 23.9 gf, and 24.2 gf, respectively. The average value is 24.1 gf and is implemented in the model. Therefore, 24.1 gf is the impact force resulting from setting CV to be 0.3 mil/ms, which is used for all the stitch bonds in the current FE model. If a different CV is used in another stitch bond experiment (e.g. CV = 0.45 mil/ms), then a re-extraction of the bond signals reveals the exact duration of the impact force (which is 3 ms for CV = 0.3 ms in this study), and the magnitude of the F_{CV}, F_0, and F_B. These values are helpful to determine the new impact force by means of Equation 15.

The second step is the scrubbing step. In this step, three cycles of scrub at 100 Hz frequency and perpendicular to wire direction are applied together with skid and bond force, experimentally, as shown in Fig. 87. In order to avoid the excessive mesh distortion, two cycles of scrub are used in the model instead of three cycles, while the scrub frequency is kept exactly the same as the experiment (100 Hz). The third and last step is the "unloading" step where the capillary is moving upwards, disengaging from the now permanently deformed wire.

The time steps in the model are calculated automatically. They depend on the duration of each segment (touch down, scrub and skid, and unloading), and the level of mesh deformation during the modeling. The more deformation occurring in the model, the smaller is the minimum time step increment required, and consequently, the longer the computation time.

4•6•2 Load, Boundary Conditions, Process Parameters

The wire part is kept completely free (no load or boundary conditions applied). The boundary condition of the substrate is applied to all its sides except the upper side. The type of the boundary condition is the complete lock down of the displacement and rotational degrees of freedom. It is schematically shown in Fig. 88. In other words $\delta U_x = \delta U_y = \delta U_z = \delta UR_x = \delta UR_y = \delta UR_z = 0$ where δU_x, δU_y, and δU_z, are the allowable cartesian displacement in x, y,

and z directions, respectively, and δUR_x, δUR_y, and δUR_z, are the allowable rotational displacement in x, y, and z directions, respectively.

The load is applied to the reference point of the capillary as concentrated (point) force. In the touch down segment, a "smooth" amplitude type is used to minimize artificial inertia and excessive mesh distortion in the early stages of the deformation. Several different boundary conditions are applied to the reference point of the capillary tip at various times during the process. During the touch down step, the capillary has no displacement or rotational degrees of freedom except vertical in load direction (downwards). In the bonding step, bonding force is kept constant, while the scrub and skid are applied as boundary conditions to the capillary. The scrub motion is applied perpendicular to the wire direction with 100 Hz frequency and two full cycles. A periodic amplitude mode is available in the force module of ABAQUS and it is well suited for applying scrub. In addition, skid is also applied to the capillary reference point in the XY plane in the wire direction. In contrast to scrub, skid is a non-periodic one time motion along the wire direction for a predefined distance. Finally, in the unloading segment, the load is dropping to 3 gf and the stitch bond process is complete. Selecting 3 gf for the end of unloading is mainly to avoid artificial numerical bouncing of the capillary. The difference in the final stress field is insignificant if either 3 gf or 0 gf is selected as the end force. The position of the capillary reference point is shown in Fig. 89 (a) and the plots of load and capillary tip movements during modeling are shown in Fig. 89 (b).

4•6•3 Model Meshing

As the wire and substrate parts are deformable materials in the model, they need appropriate meshing in order to be included in the simulation. For both wire and substrate, the "Hex" type

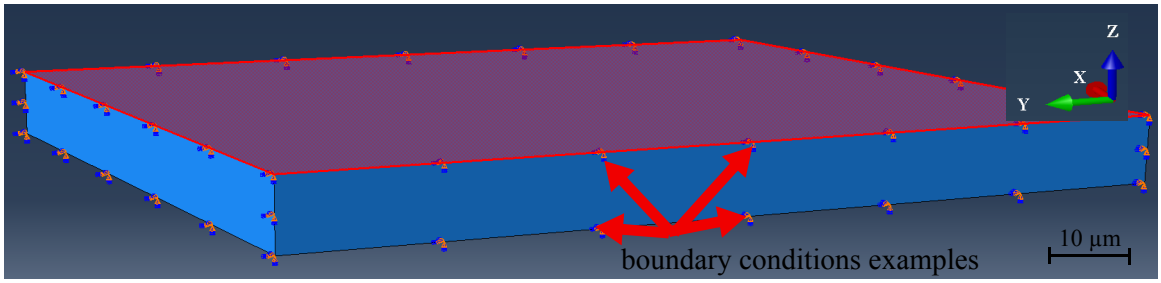

Fig. 88 Boundary condition of the substrate. All the sides except the shaded side are excluded with the displacement and rotational degrees of freedom.

of the mesh elements are used. Hex elements are the three dimensional form of the square elements in the two dimensional problems. The reason for selecting hex elements over "Tet" triangular elements is mainly due to their increased number of the integration points which makes them more precise. The structured type of the Hex element is used for the substrate as it has a cubic type of geometry. However, for the wire, the sweep version of the Hex element is used to suit the somewhat rotational symmetric geometry of the wire.

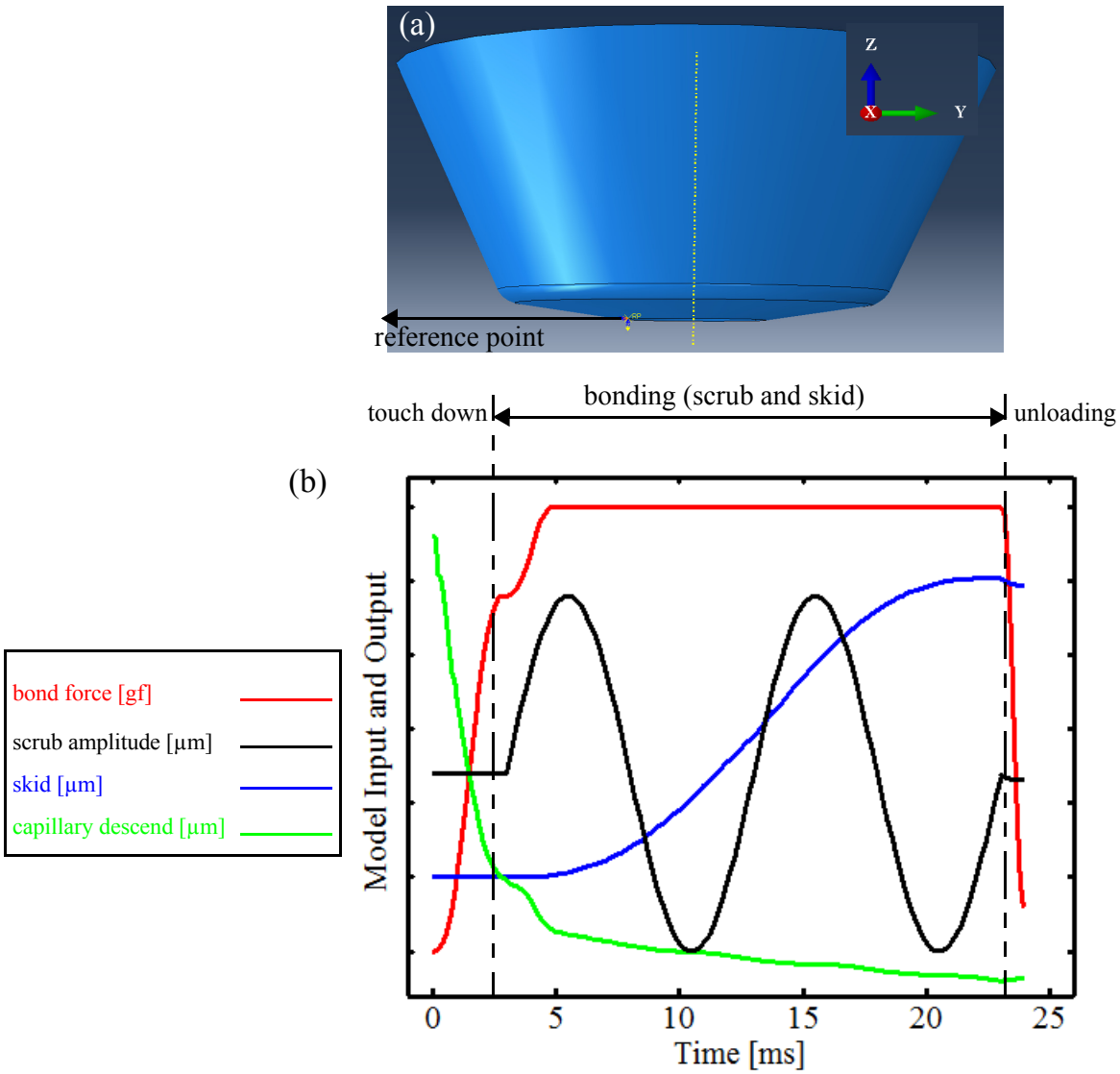

Fig. 89 (a) capillary tip with its reference point (b) Schematic bonding loads and capillary tip movements during modeling. Process parameters are 30 gf bond force, 5 µm scrub amplitude, and +5 µm skid.

When analyzing the model geometry it is obvious that not all regions are undergoing the same amount of deformation. For example, the wire regions below the capillary chamfer area are undergoing more severe deformation than other wire and substrate regions. Therefore, a non-uniform distribution of mesh element size is applied to generate a higher element density at regions where the largest deformations are expected. This helps to reduce the process modeling computational cost and requires a proper partitioning of the various parts into subregions. The mesh generated in this way on the wire and substrate parts are shown in Fig. 90. The wire part contains 4050 mesh elements with a minimum size of 0.5 µm and maximum size of 3 µm. The substrate part contains 3000 mesh elements with a minimum size of 1 µm and maximum size of 7.5 µm.

4•6•4 Mass Scaling Optimization

In order to speed up the process simulation, a feature of ABAQUS dynamic explicit module called "mass scaling" is used which is recommended for large deformation problems [107]. With mass scaling the material density is increased artificially. If the material density in the model is increased by a factor of F^2, then the wave propagation speed inside material is decreasing by the factor of F, which consequently increases the stable time increment by the factor F. In other words, the simulation computation time is reduced by factor F. However, the mass scaling factor has to be increased carefully to avoid artificial inertial effects and consequently erroneous solutions. Therefore, a mass scaling optimization is necessary to ensure that physical artifacts are negligible. Before the mass scaling optimization, a mesh sensitivity analysis is done, and through measuring the vertical displacement of the capillary (in z direction) versus mesh size, it is assured that the results are for the converged meshes and do not

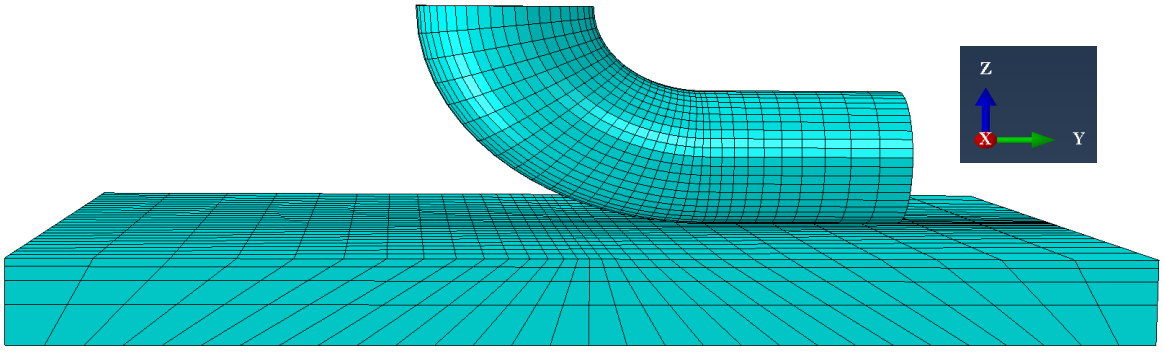

Fig. 90 Mesh distribution in the wire and substrate

depend on the mesh size. To investigate the effect of mass scaling in the current model, six levels of mass scaling are considered. They are shown in Table 8 together with their corresponding run times. It was planned to repeat a fixed modeling condition (50 gf force, -5 µm skid, and 3 µm scrub amplitude) with all the six mass scaling factors (MSF). The MSF can be implemented in the model directly and it is equal to the square of the multiplier of the density. So everything in the model is kept fixed except the MSF value. The effect of MSF on the computational run time is shown in Fig. 91. Results indicate that there is a logarithmic relationship between MSF and run time. An optimized selection of the MSF provides significantly accurate results in the lowest possible time.

The effect of MSF on the deformed stitch bond is shown in Figs. 92 and 93. In Fig. 92, the von Mises stress in the deformed model is shown for various MSF values. The qualitative

Table 8: Mass scaling factor (MSF) levels

Level #	1	2	3	4	5	6
MSF	500000	100000	50000	10000	1000	500
Run Time [h]	0.67	1.29	1.55	2.98	7.32	10.76

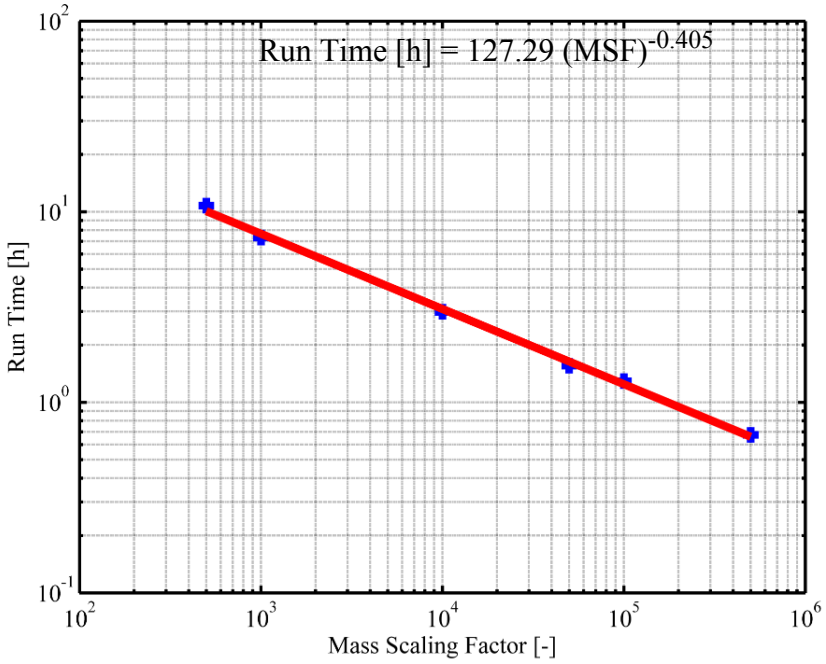

Fig. 91 Effect of mass scaling factor on model run time.

observation is that at MSF lower than 1000, the changes in the contour colors is insignificant. The wire reached a maximum deformation of 34.6 µm width with the largest MSF compared to 27.8 µm width with the smallest MSF as shown in Fig. 93. The same kind of observation is detectable in Fig. 94 which shows the equivalent plastic strain distribution at various MSF levels. However, to have a more quantitative type of response to highlight the effect of MSF level on the model, the internal energy and kinetic energies are extracted from the model his-

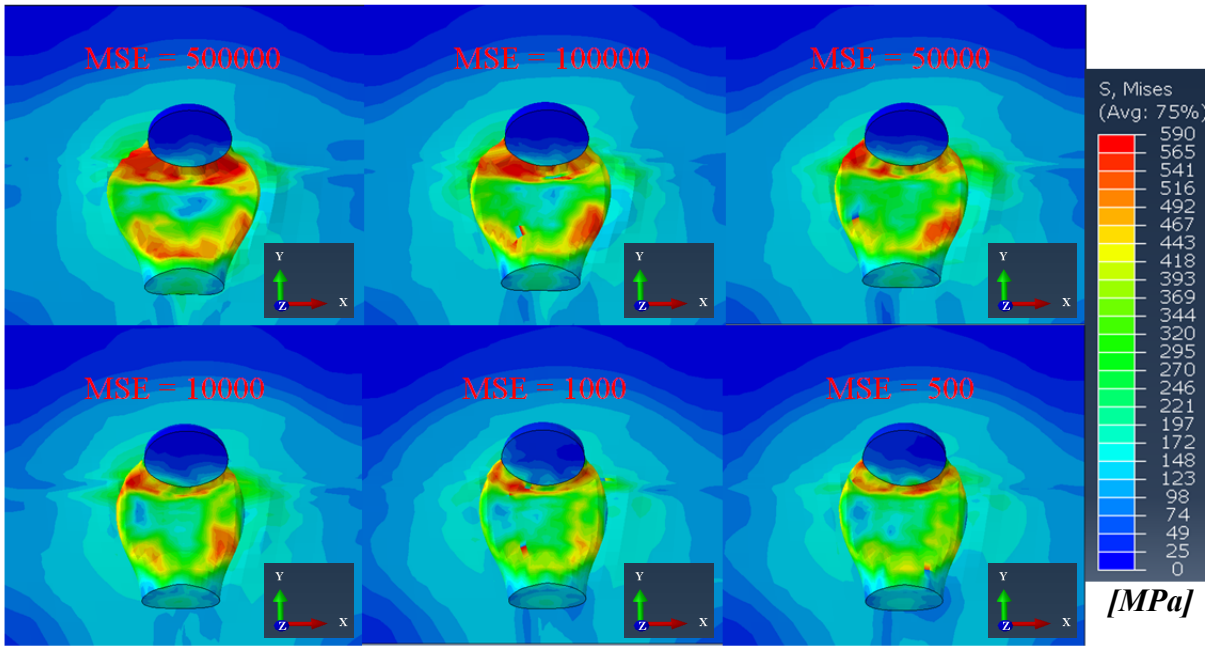

Fig. 92 Effect of MSF on von Mises stress distribution in deformed stitch bond model.

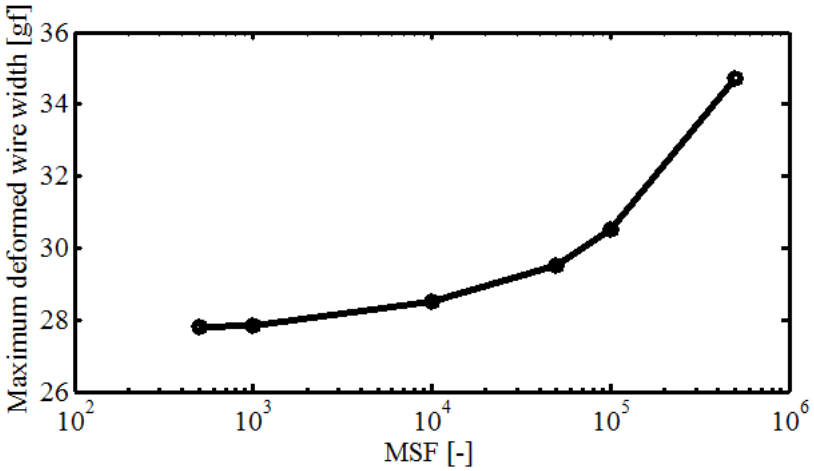

Fig. 93 Effect of MSF maximum deformation of wire width.

tory output (in tables provided by ABAQUS) and shown in Figs. 95 and 96, respectively. Figure 95 shows that decreasing the MSF level down to 1000 decreases the internal energy of the model constantly. However the step from 1000 to 500 causes virtually no change in the

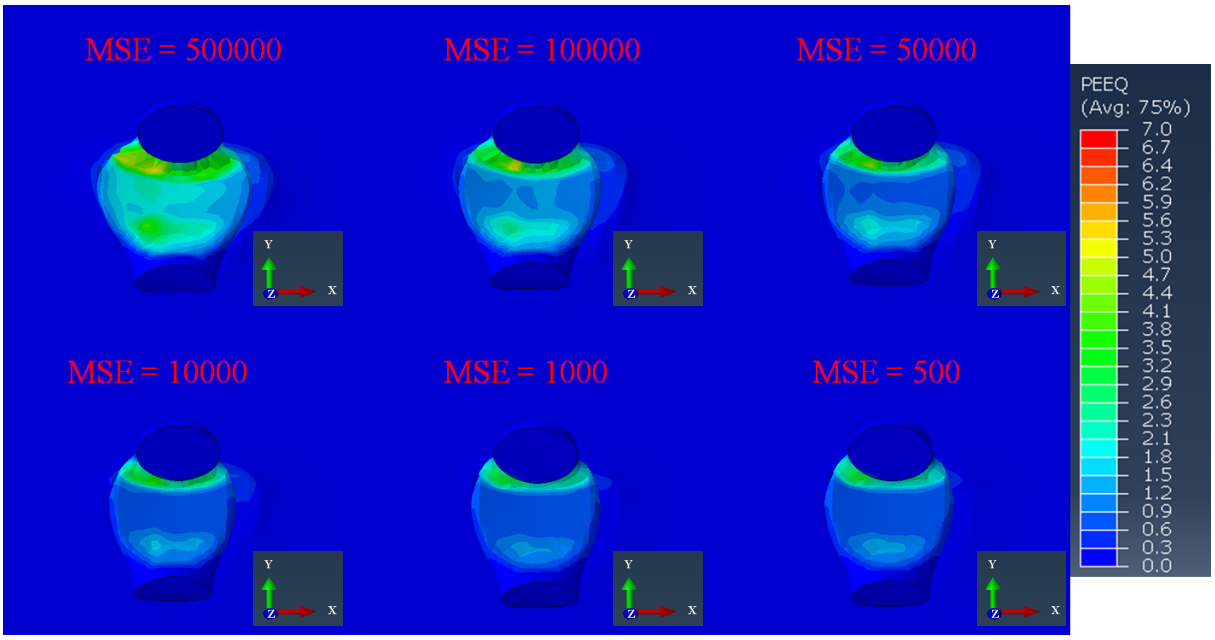

Fig. 94 Effect of MSF on equivalent plastic strain distribution in deformed stitch bond model.

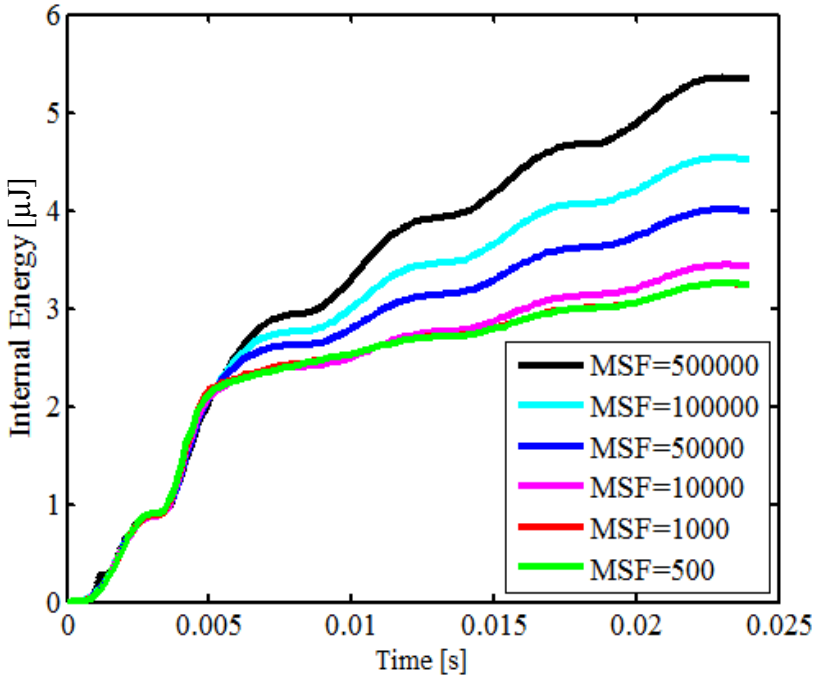

Fig. 95 Effect of MSF on model internal energy.

result (less than 0.2%). In addition, the kinetic energy of the model is virtually constant for MSF of 1000 and below (yellow plot) as shown in Fig. 96. In summary, a MSF level of 1000 is a safe level in this model to ensure that there are no unwanted artifacts of inertia.

4•7 Example Result with Standard Responses

The ABAQUS model is able to output some standard responses automatically. The standard responses extracted from the current model include stress, strain, displacement, and sliding distance. Some of these standard responses are implemented into proper formulas to derive custom numerical responses and will be discussed in the next chapters. An example of a deformed stitch bond with process parameters is shown in Figs. 97 (a) - (d). The process parameter used is 50 gf force, 3 µm scrub amplitude, and no skid. The equivalent plastic strain distribution in the wire and substrate are shown. Deformed model pictures reveal that the magnitude of strain levels are much higher in wire compared with the substrate. The plots of force, scrub, and skid upon modeling time is shown in Fig. 98. The force, scrub, and skid are applied on the capillary tip reference point and are shown. In addition, the descent of the capillary tip during loading and scrubbing is shown. The step by step evolution of the model ver-

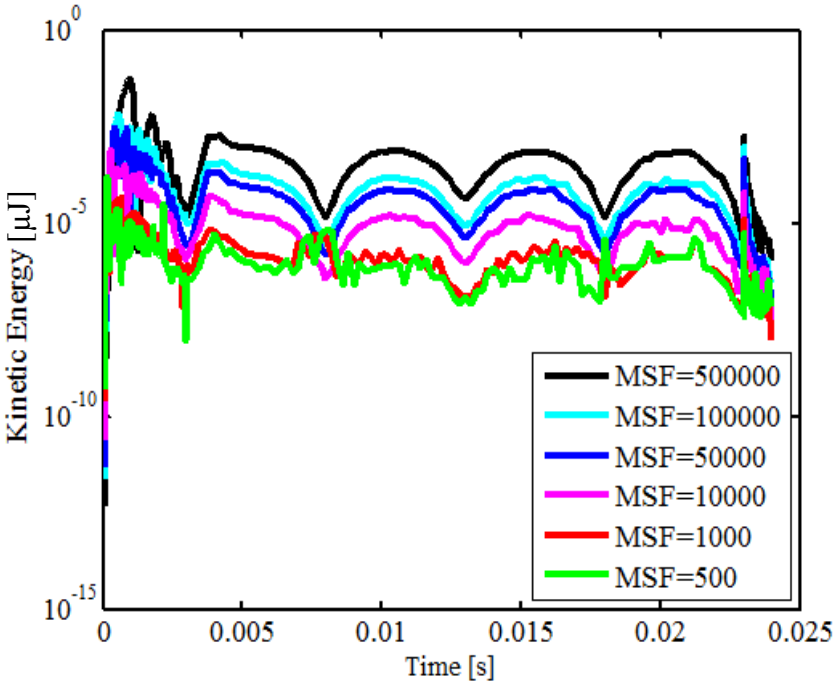

Fig. 96 Effect of MSF on model kinetic energy.

sus time is shown in Fig. 99.

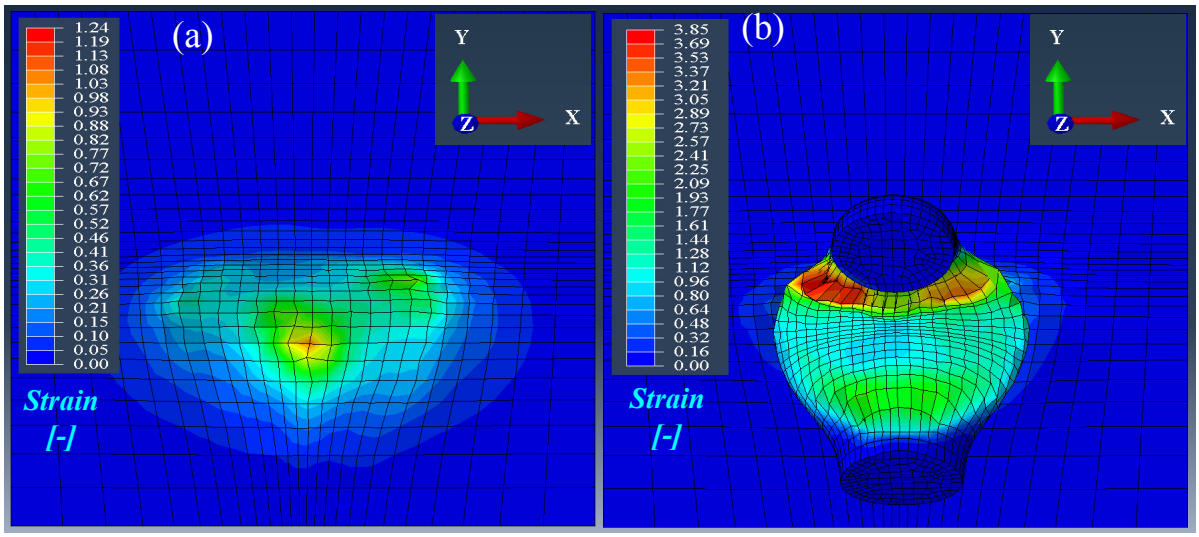

Fig. 97 Deformed model of stitch bond made by 50 gf force, 3 µm scrub amplitude, and no skid. (a) Equivalent plastic strain distribution in substrate and (b) Equivalent plastic strain distribution in wire.

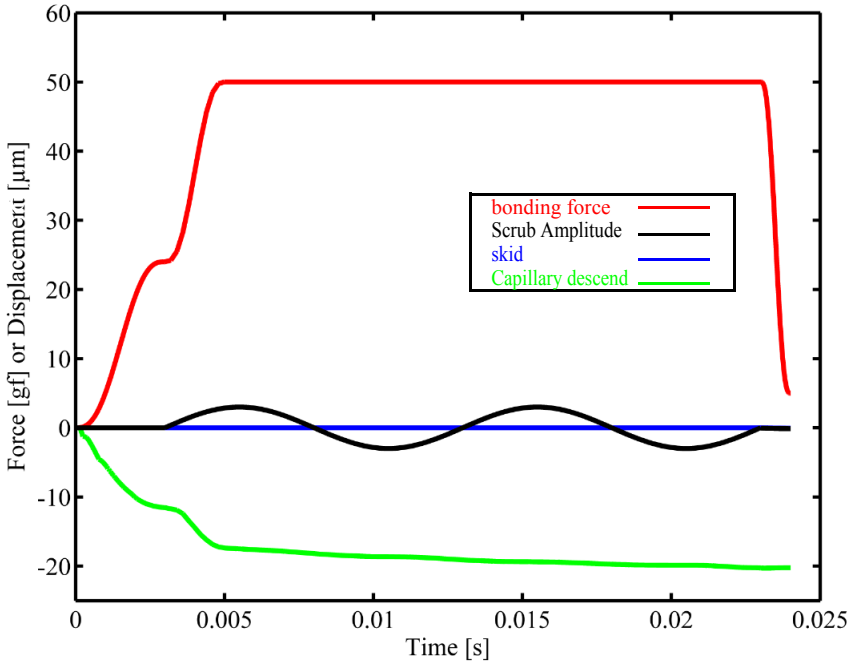

Fig. 98 Description of bond force, scrub, and skid implementation into the model, and the following descend of capillary tip. Process parameters are 50 gf bond force, 3 µm scrub amplitude, and zero skid.

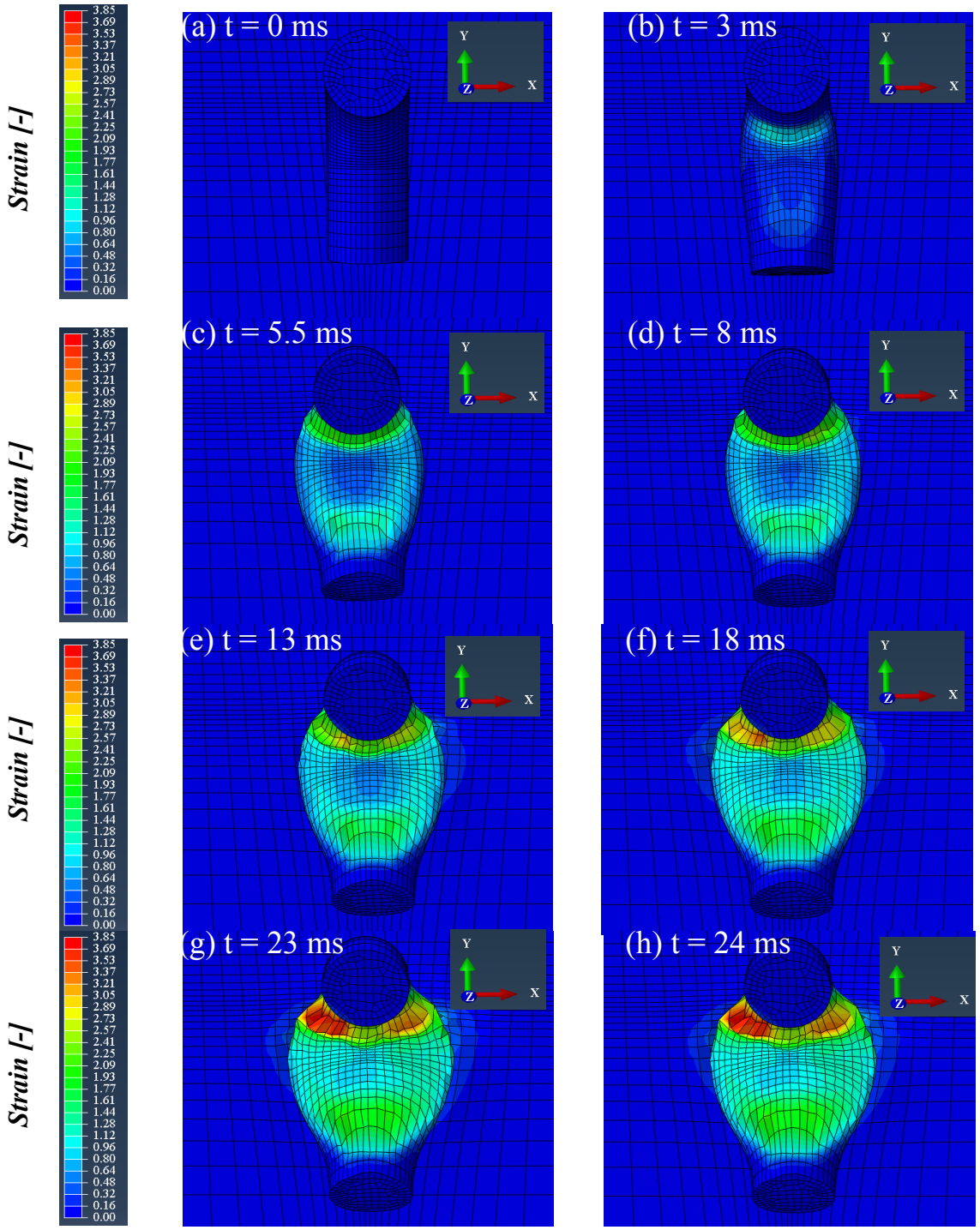

Fig. 99 Evolution of equivalent plastic strain of deforming model with modeling time. (a) 0 ms, (b) 3 ms, (c) 5.5 ms, (d) 8 ms, (e) 13 ms, (f) 18 ms, (g) 23 ms, (h) 24 ms. The wire diameter is 18 μm.

4•8 New Post-Processing Methods to Extract Quality Responses

4•8•1 Contact Area Calculation

The stitch bond is formed at the interface between wire and the substrate. Therefore, this interface is of special interest during the modeling. In other words, the properties, geometry, and size of this interface needs to be considered when attempting to correlate model outputs with experimental observations. The very first type of response that can be extracted from the model results is the contact area (A_C). Such an area is not normally automatically rendered by ABAQUS and therefore has to be calculated in a separate procedure based on the data available after the FE calculation.

The procedure to calculate A_C starts with extracting the end coordinates of all the substrate and wire nodes. This is done by using the "report" feature of ABAQUS to save the coordinates of all wire and substrate nodes before and after modeling. The next step is to load this data into Matlab™ (Mathworks, Natick, MA, UNITED STATES). An example is shown in Figs. 100 and 101 for the wire and substrate before and after modeling, respectively. The sample is bonded with 50 gf force, 3 µm scrub amplitude, and no skid.

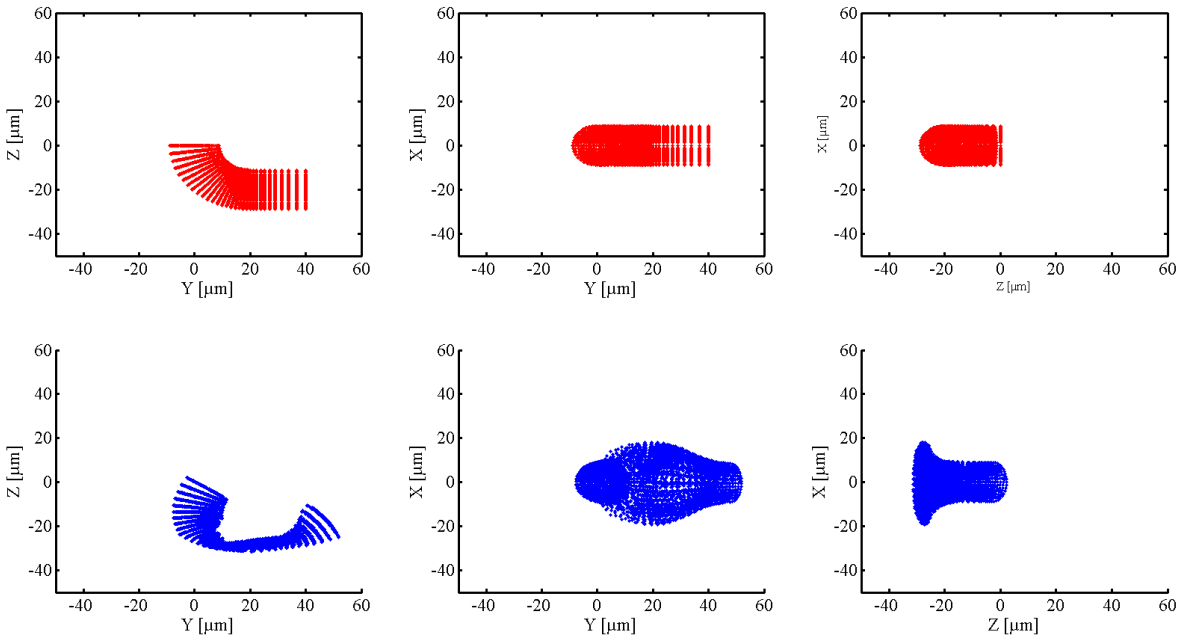

Fig. 100 Wire nodes coordination in the model in different views. Red plots are before modeling and the blue plots are after modeling. The 3rd axis locations are at (a) center of wire (b) wire-substrate interface, and (c) center of wire.

The next step is to find the nodes which are part of the wire/substrate contact in either the wire or the substrate. To do this, a specific response of ABAQUS called FSLIPEQ is used. It is the distance slided a contact node for a specific contact pair. It can be selected for any contact pairs defined in the model. In the current model, as the wire/substrate is the preferred contact pair, the FSLIPEQ values are extracted from the wire/substrate contact pair. Two values can be extracted: FSLIPEQ1 and FSLIPEQ2 are the total sliding distances for the wire and substrate nodes, respectively, which are in contact with the substrate and wire, respectively. The distribution of total sliding distances in the wire and the substrate are shown in Figs. 102 (a) - (d).

The extracted sliding distance response has a non-zero value if there is any contact in the substrate or wire and therefore can be used to distinguish between the contacts nodes and non-contact nodes in the wire and substrate. Thus, the sliding distance values of all the wire and substrate nodes are reported out of ABAQUS into a text file together with the x, y, and z coordinates of all the nodes. Using the "node_extraction.m" code [117], the nodes with non-zero sliding distance are filtered from the other nodes and so that the wire and substrate contact areas are found and defined as A_{CW} and A_{CS}, respectively. Examples are shown in Fig. 103. For both the wire and substrate, the peripheral contact nodes were found using the "convhull"

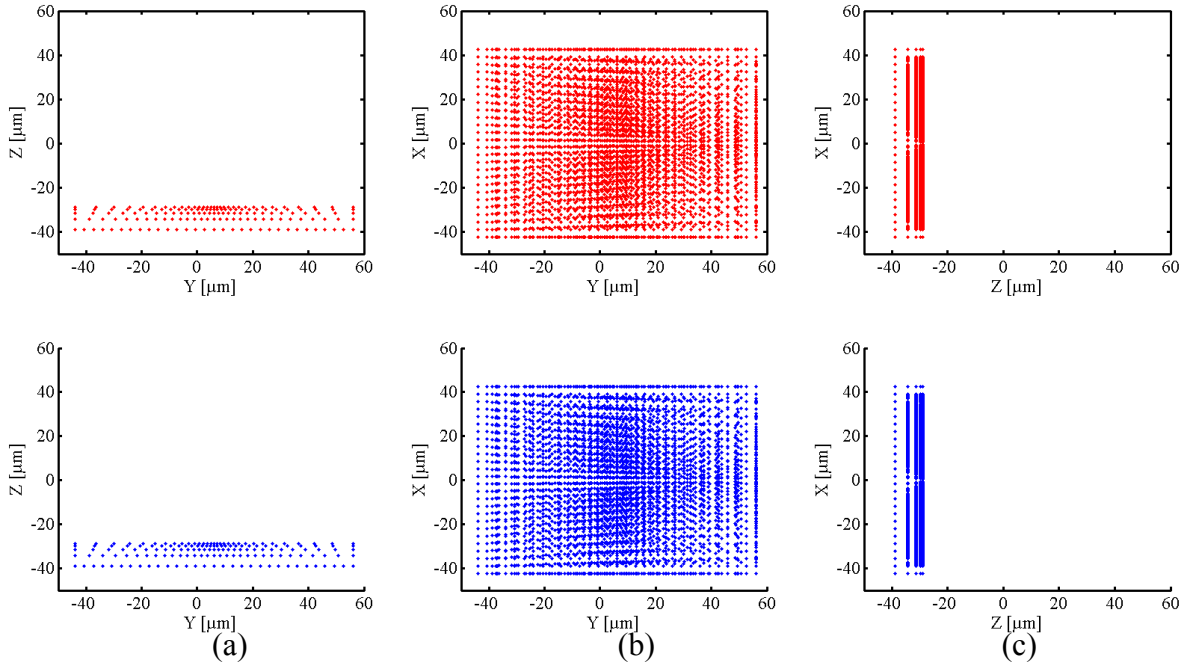

Fig. 101 Substrates nodes coordination in the model in different views. Red plots are before modeling and the blue plots are after modeling. The 3rd axis locations are at (a) center of wire (b) wire-substrate interface, and (c) center of wire.

function of MATLAB, and the “polyarea” function was then used to calculate the contact area.

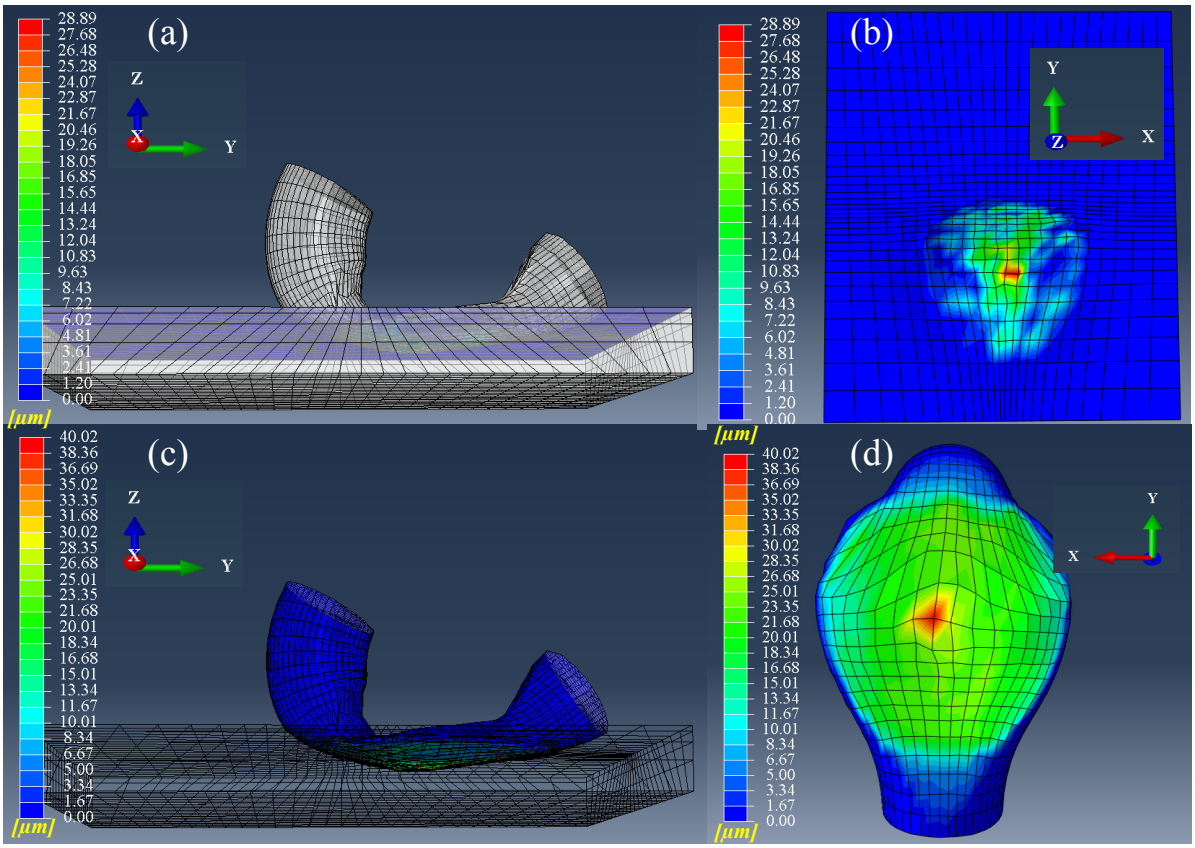

Fig. 102 Total sliding distance distribution in model parts. (a) and (b) sliding distance distribution for substrate nodes in two different views. (c) and (d) sliding distance distribution for wire nodes in two different views.

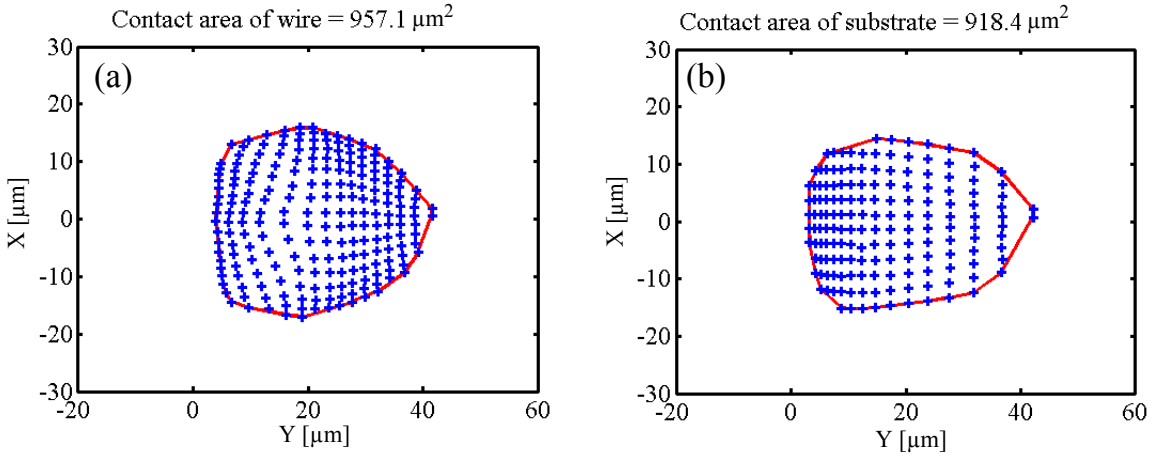

Fig. 103 Contact areas on (a) wire (b) substrate.

However, when scrub is used, the wire get moved from side to side, covering more area on the substrate than there finally is at the interface. Also, the wire deforms and parts that touch the substrate eventually lift off again when the scrub moves to the other side. Therefore, the surface area with this procedure tends to be slightly larger than the real bond area if scrub is used (at least).

4•8•2 Surface Expansion

For successful cold welding the expansion of the faying surfaces is a key factor. It opens up cracks in surface contamination layers. The cracks work as metal extrusion paths. Via these cracks there is intimate contact of fresh metal surfaces from opposing sides of the interface which is a prerequisite for adhesion/bonding [73, 74].Surface expansion is defined as the ratio of the clean surface area produced by the plastic deformation to the total bond area after the deformation, or equally the plastic strain, as shown in Eqn. 4.

Within the current model, two ABAQUS responses are candidates representing the interfacial surface expansion. The first candidate is the amount of nodal equivalent plastic strain which can be presented by *PS*. *PS* can be calculated for wire contact *PSW*, substrate contact *PSS*, averaged over wire and substrate contacts, or combined over substrate contact *PSC* (all dimensionless).

The second candidate is the sliding distance of the contact nodes *SD*, and it can be calculated for wire contact *SDW*, substrate contact *SDS*, averaged over wire and substrate contacts *SDA*, or combined over substrate contact *SDC* (all in μm). The distribution of *PS* and *SD* in the wire and substrate for a sample bonded with 50 gf, 3 μm scrub amplitude, and no skid is shown in Fig. 104.

4•8•3 Mesh Grid Method

The two defined output candidates for the surface expansions need to be averaged over the area. To do this, a grid averaging method is carried out. The averaging process starts with defining a Cartesian grid in the XZ contact plane. This grid spans all interfacial nodes. To average an output, e.g. PS, first all the grid points which lie inside the contact area are detected using “PE_and_SD_Extraction.m” [117]. If any of the grid points are outside of the

contact area, they will be ignored. For each of the grid points inside the contact area, the three nearest neighbor contact nodes are found. For the three points, their PS values are weighted proportional to their distance to their corresponding mesh grid point. The closest point has the highest weight. The weight formula for an example response is

$$W_1 = \frac{r_2 + r_3}{r_1 + r_2 + r_3} \cdot \frac{1}{2} \cdot Response_1 \tag{16}$$

$$W_2 = \frac{r_1 + r_3}{r_1 + r_2 + r_3} \cdot \frac{1}{2} \cdot Response_2 \tag{17}$$

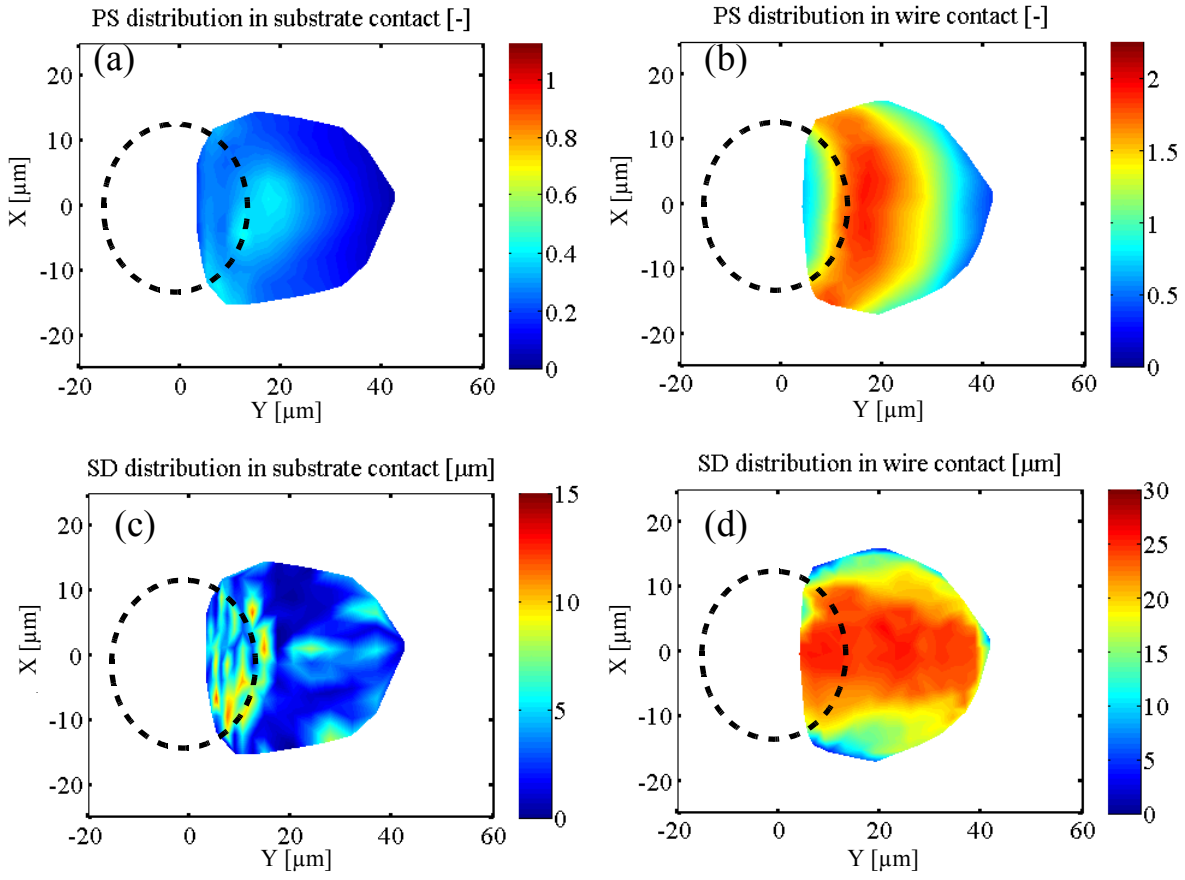

Fig. 104 *PS* and *SD* distribution in the deformed model parts (a) *PS* for substrate contact area, (b) PS for wire contact area, (c) *SD* for substrate contact area, and (d) *PS* for wire contact area. The dashed circle shows the position of capillary chamfer.

$$W_3 = \frac{r_1 + r_2}{r_1 + r_2 + r_3} \cdot \frac{1}{2} \cdot Response_3 \tag{18}$$

These formulas are inspired by the Lever rule as used in materials science. They assure the sum of all weights is always 1. In Fig. 105 an example calculation of the three first nearest neighbors for wire and substrate is shown. Example evaluations with mesh grid numbers of 2 and 7 are shown in Fig. 106. The averaging could be done for the wire contact area (blue symbols), the substrate contact area (red symbols), average of the wire and substrate, or combination of wire and substrate. It is assumed that if enough number of partitions are used, the average value tends to its actual value. An example response for various numbers of grid points is shown in Fig. 107. It shows that the response error falls below 2% if more than a mesh grid number of 8, resulting in 64 points, is used. This level of accuracy is sufficient for this study.

4•8•4 Frictional Energy (Work) Generated in the Model

During bonding, energy from sliding friction is delivered to the interface which is beneficial for bonding. Sliding friction is able to render a cleaner bond interface and brings cleaner metal surfaces together. Therefore, the amount of friction energy (work) is extracted during model-

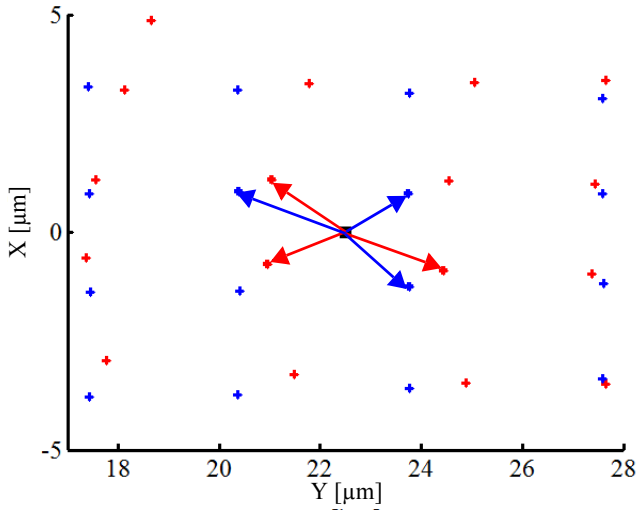

Fig. 105 Calculation of the three first nearest neighboring nodes of a grid position in an example contact. The blue + symbols correspond to the wire contact area nodes, and the red + symbols correspond to the substrate contact area nodes.

ing. To do this, the "history output" of the ABAQUS software is used to collect the frictional energy accumulated at various times during bonding. An example of frictional energy extracted during modeling is shown for a sample bonded by 50 gf bond force, 3 µm scrub amplitude and no skid in Fig. 109. The data shows that the major generation of the frictional energy is upon start of scrubbing at 3 ms. In this example bond simulation, a total of 0.6 µJ of

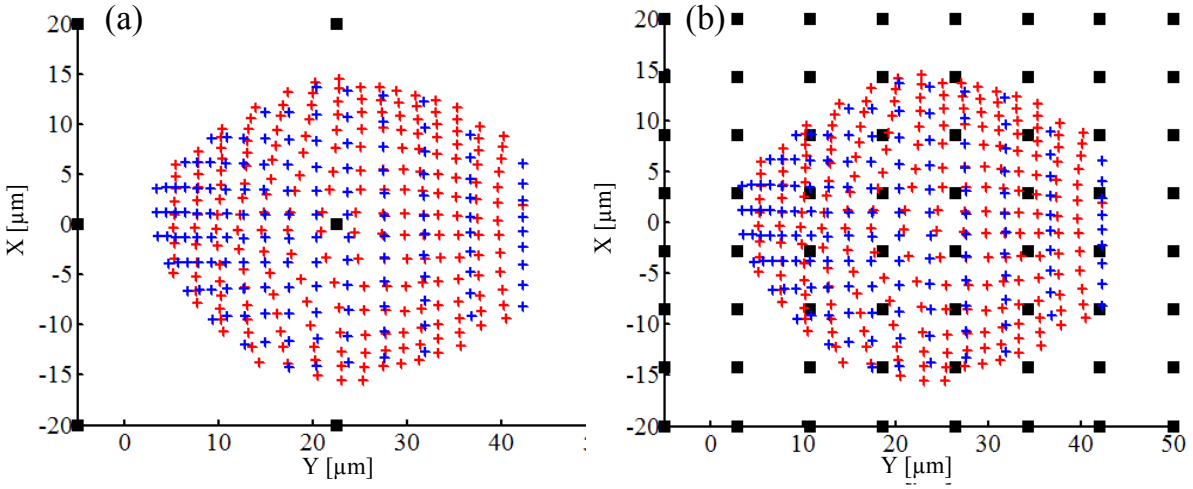

Fig. 106 Mesh grid averaging of outputs through contact area (a) 2 × 2 grid elements (3 × 3 grid points) (b) 7 × 7 grid elements (8 x 8 grid points). The blue + symbols correspond to the wire contact area nodes, and the red + symbols correspond to the substrate contact area nodes.

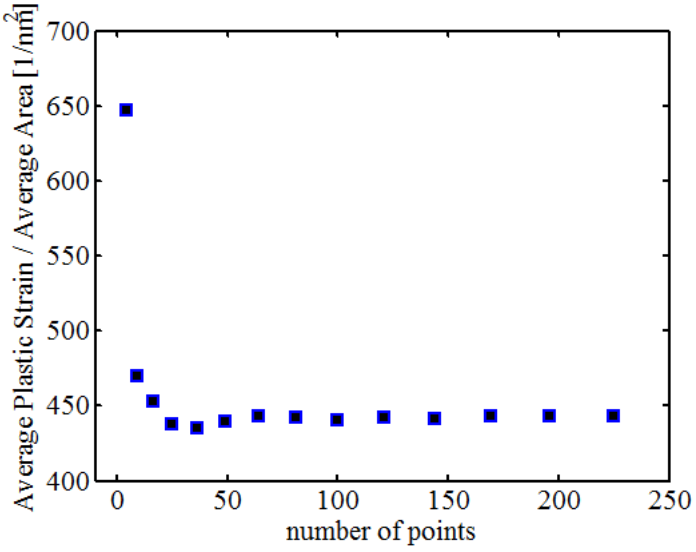

Fig. 107 The evolution of the average PS per area by increasing the number of grid points (squared mesh grid number).

friction energy is delivered by scrub to the complete (tail + wedge) bond interface after 20 ms of bonding. The calculated friction work in this work is about 100 times smaller than the typical ultrasonic friction work [116]. This is expected mainly due to the lower frequency of the scrub (~ 100 Hz) than a typical ultrasonic vibration (~ 120 kHz).

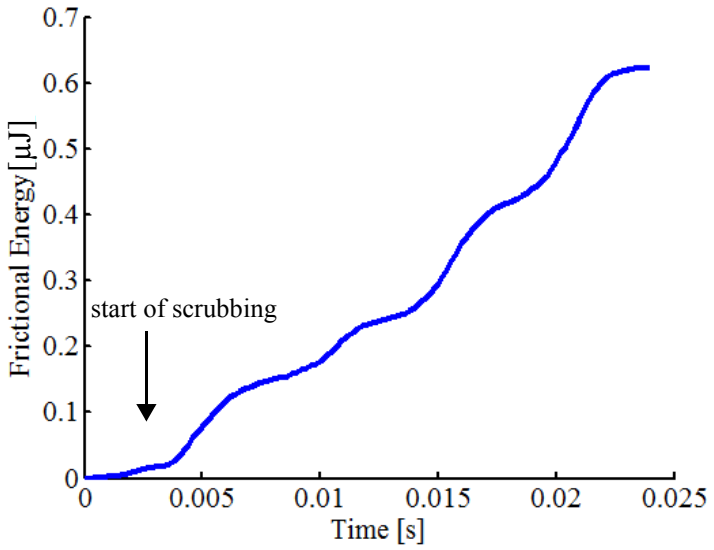

Fig. 108 Frictional energy built up during modeling.

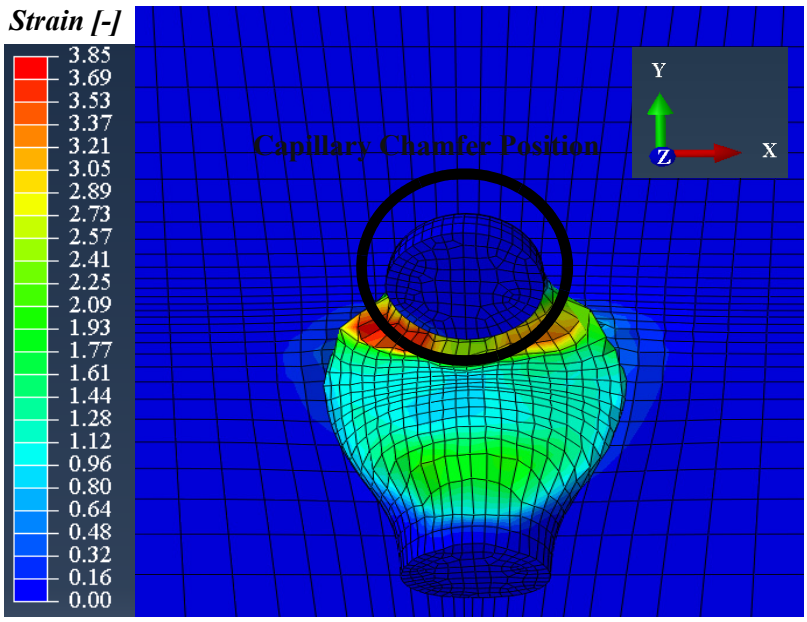

Fig. 109 The position of the capillary chamfer.

4•8•5 Distinguishing between Different Regions of Contact Area

The stitch bond is divided into a “wedge” and a “tail” part, as shown in Fig. 4. To identify the two parts in the model the location of the capillary chamfer is determined using a custom made program “Tail_Separation.m” [117]. The position of the capillary chamfer is shown in Fig. 108. Using the position of the capillary chamfer the custom program applies a filter to the contact nodes considering the contact nodes inside the chamfer as tail nodes, and the contact nodes outside the chamfer as stitch nodes or “wedge” nodes, as shown in Fig. 110.

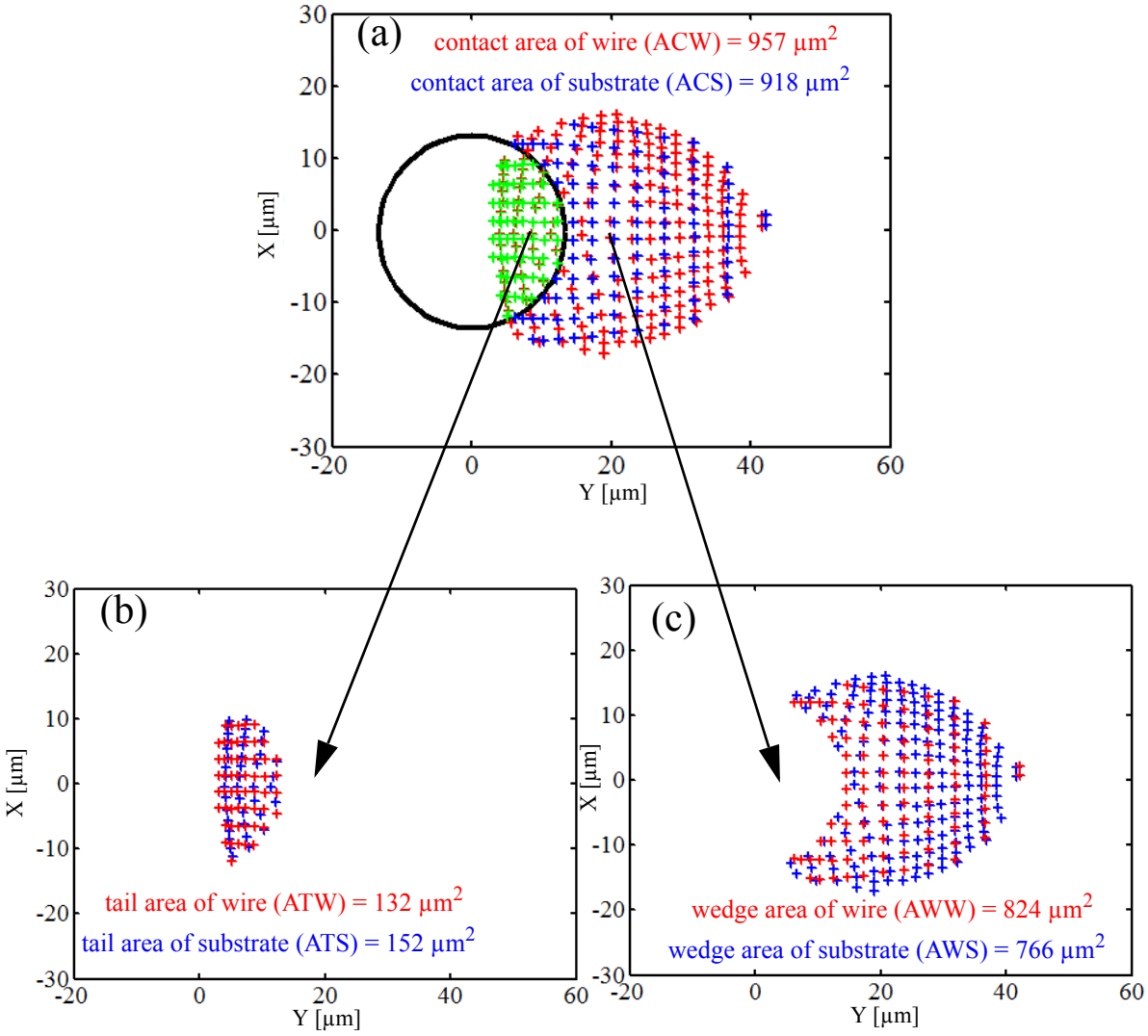

Fig. 110 Simulated regions in a contact area. (a) Total contact area (b) Tail region (c) Wedge region. Red nodes belong to substrate contact and blue nodes belong to wire contact. The process parameters are 50 gf bond force, 3 µm scrub amplitude, and -5 µm skid.

The friction energy calculated in the model is a global output and it cannot be calculated for different regions of the contact pair (tail or wedge). But, the plastic strain and sliding distance standard responses are local (node-wise) responses, and so can be calculated for different regions of the contact.

4•8•6 Candidate Responses

Model responses are grouped in four sets including area responses, plastic strain responses, sliding distance responses, and friction energy responses. All responses are investigated for bond quality prediction. The correlation of each candidate with the experimental results is determined in Chapter 5.

The areas of the tail and wedge contact regions make up the first set of candidate responses extracted from the model for both the wire and substrate. A total of six areas are evaluated as defined in Fig. 111.

The second set of responses is related to the surface change, either by expansion (strain, elongation) or by motion (sliding distance) per area that can be evaluated for all six areas. Both plastic strain (*PS*, dimensionless) and sliding distance (*SD*, in μm) are evaluated using the below expressions:

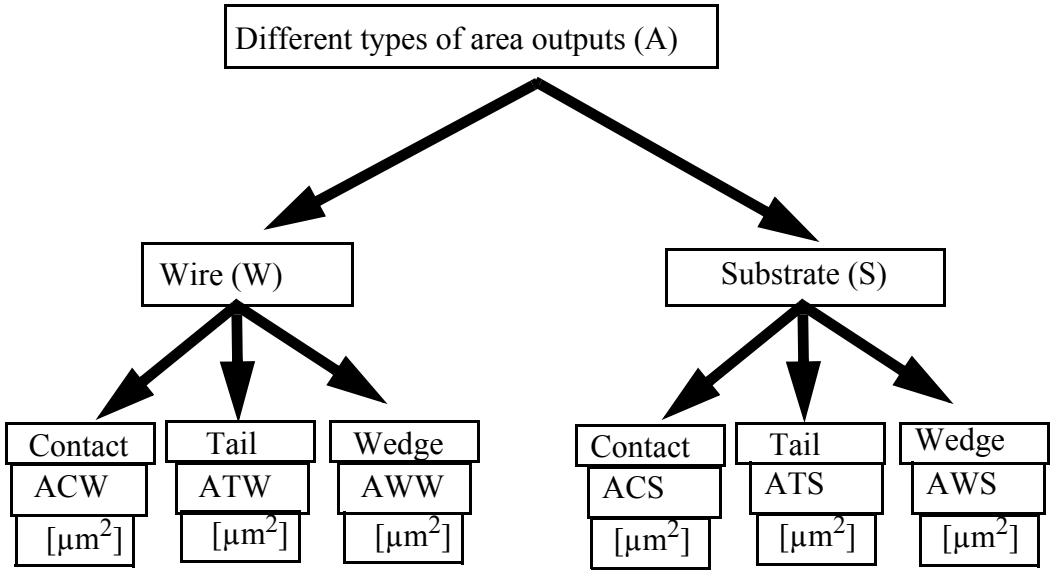

Fig. 111 Different types of area output extracted from the model.

$$(Response)_1 = \frac{Average(PS)}{Area} \tag{19}$$

$$(Response)_2 = \frac{Average(SD)}{Area} \tag{20}$$

These responses can be calculated for the wire, the substrate, the average of wire and substrate, and the combination (multiplication) of wire and substrate. In addition, each of those responses can be calculated for contact, tail, and wedge. This leads to 24 different types of responses, as defined in Fig. 112. Building up the combined response is inspired from "overlapping surface exposure" term reported in [76].

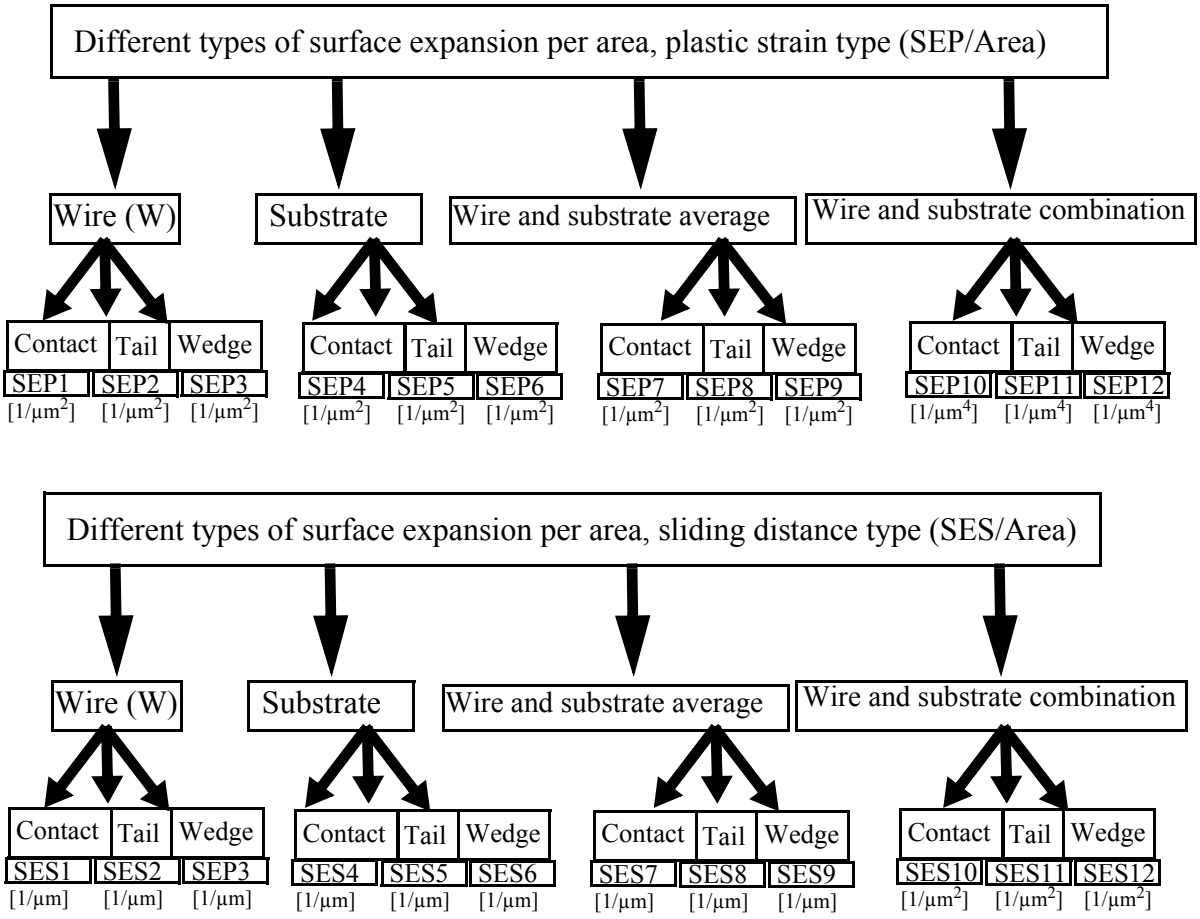

Fig. 112 Different types of area output possible to extract from the model.

The response calculation is done by using the mesh grid method described in subsection 4•8•3. Regardless of the type of the surface change response (plastic strain or sliding distance) and the region of the interface (wedge, tail, or contact), four methods of response extraction can be performed: only on wire, only on substrate, average of wire and substrate, and combination by multiplication of wire and substrate. These could be expressed in the following formulas for enhancing the clarity:

For wire only, substrate only, average of wire and substrate, and combination of wire and substrate, the following four equations are used:

$$\left(\frac{SE}{Area}\right)^{W} = \frac{1}{A_W} \cdot \frac{1}{n} \cdot \sum_{1}^{n} (Response)^{W} \tag{21}$$

$$\left(\frac{SE}{Area}\right)^{S} = \frac{1}{A_S} \cdot \frac{1}{n} \cdot \sum_{1}^{n} (Response)^{S} \tag{22}$$

$$\left(\frac{SE}{Area}\right)^{Average} = \frac{1}{average(A_W, A_S)} \cdot \frac{1}{n} \cdot \frac{1}{2} \sum_{1}^{n} [(Response)^{W} + (Response)^{S}] \tag{23}$$

$$\left(\frac{SE}{Area}\right)^{Combination} = \frac{1}{(A_W \cdot A_S)} \cdot \frac{1}{n} \sum_{1}^{n} [(Response)^{W} \cdot (Response)^{S}] \tag{24}$$

where response is either equivalent plastic strain or sliding distance, the area is contact, tail, or wedge, and *n* is the number of the mesh grid points which lie inside the stitch bond interfacial area.

The third set of responses are based on the amount of the frictional energy produced in the model. This response is available from ABAQUS only as one global number corresponding to the entire interface regardless of tail, contact or wedge regions. The evaluation of frictional energy for the two subregions of the contact area would require additional steps, including

multiplying normal stress and sliding distance increments are at all times during the calculation and has not been carried out in this thesis.

The fourth and final set of responses are based on the multiplication of the surface change responses with the frictional energy. The frictional energy delivered to the interface can be multiplied by all 24 surface expansion responses, resulting in 24 new responses.

In summary 6+24+1+24 = 55 responses extracted in this thesis that are expected to have a physical relationship to the quality of the bond process. The next step is to run a simulation DOE matching a selection the experimental cases and make comparisons to determine the degree of correlation.

5 Finite Element Model of Stitch Bond, Part II: Results

In this chapter, the correlation between numerical candidate responses and the experimental observations of the stitch bond is going to be discussed. The stitch bond process with 18 µm diameter PCC wire on PPF plated QFN substrate described in section 3•1 is used as a basis for the numerical model. The same type of materials, wire diameter, and capillary geometry are used in the model. The various process parameters for the numerical DOE include 30 gf to 70 gf bond force (5 levels), 1 µm to 5 µm scrub amplitude at 100 Hz (3 levels) and -5 µm to 5 µm (3 levels) of skid (XY-distance), 45 cases all together.

To make the correlation between numerical quantitative candidate responses and the qualitative stitch bond responses, the experimental observations will be coded in different ways. In addition, the candidate responses will be divided for three different regions including total contact, wedge, and tail regions. The numerical candidate responses will be plotted with respect to the coded experimental observation for all of the cells. The total computation time for the 45 cases was about 30 days on Mijo06 PC which has a Intel(R) Core(TM) i7-4770K CPU @ 3.50 GHz CPU and 16 GB RAM.

5•1 Development Steps of Finite element model

The FE model of the stitch bond has been developed to enhance the understanding of the stitch bond process. To do this development, several steps have been done. The model development flowchart (diary) is shown in Fig. 113.

The FE model development started with considering the half parts. However, due to the non-symmetric nature of scrub, attempting the half model was unsuccessful. Therefore a full model is developed. The SI system of units is used at the beginning. However, soon using SI units was found to be slightly confusing for a model at µm scale. Therefore, a unit system including µm, kg, and µN for distances, mass, and load is used, respectively.

Standard ABAQUS module is used first. But it was realized that a standard model is not suitable for a large-deformation model of stitch bond, and therefore the dynamic explicit is used, and mass scaling feature is added and adjusted carefully. For meshing the parts, the “Tet” type

of element is used first, but it is changed to “Hex” type. The “Hex” mesh elements are more suitable for stitch bond model.

Once the model is set up, a numerical job was conducted and the standard ABAQUS responses including plastic strain, sliding distance, displacement, and nodal coordinates were extracted. Using the standard responses, custom candidate responses are calculated by using proper formulas. Finally, numerical jobs corresponding to the experimental DOE cells are performed, and all the standard and custom responses were extracted and calculated, respec-

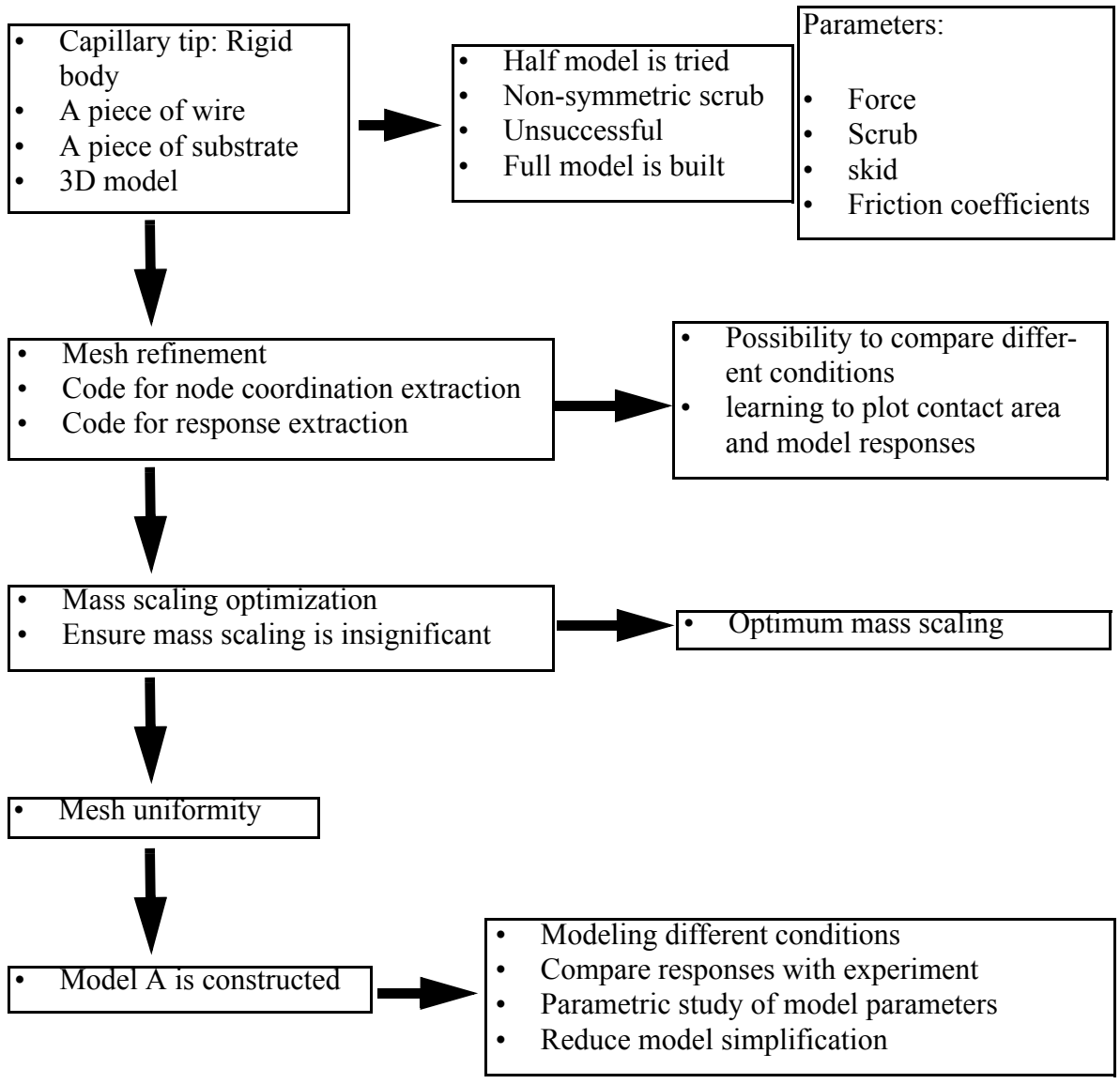

Fig. 113 FE model development steps.

tively. The comparison between numerical candidate responses and the experimental observations is discussed in the next chapters.

5•2 Quantification of Correlation of Numerical DOE with Experiment

The experimental responses consist of qualitative grading information in the form of non-sticking, sticking, and tail lifting. The expected quantitative numerical responses cannot directly be correlated with such qualitative experimental responses. Therefore, artificially, each of the experimental response types is coded with a number. Considering the different types of the possible experimental outcomes including non-sticking, sticking, and tail lifting, three different coding schemes are used. If the outcomes are separated regarding the non-sticking and sticking, the coding is 1 for non-sticking, and 2 for sticking and tail lifting (coding scheme 1). If the outcomes are separated regarding the tail lifting and non-tail lifting, the coding would be 1 for non-sticking and sticking, and 2 for tail lifting (coding scheme 2). Finally, if the outcomes are not separated at all, i.e. the occurrence of non-sticking, sticking, and tail lifting are looked all together, the coding would be 1 for non-sticking, 2 for sticking, and 3 for non-sticking (coding scheme 3). The three differently coded experimental responses are shown in Fig. 114.

To make correlations between model and experiment, all of the 55 above mentioned candidate responses are extracted from all of the 45 numerical DOE cells and normalized between 0 and 1. To find out the level of correlation between each numerical candidate response and experiment, 45 numerical candidate responses corresponding to that specific response are linearly correlated with the 45 experimental codes (all the three possible coding schemes), and the level of linear regression factor of R is calculated. Apparently a higher R means a stronger correlation between model and experiment. An example model-experimental correlation attempt using frictional energy of the model and the experimental coding schemes 1, 2, and 3 are shown in Fig. 115.

5•3 Ranking the model responses according to correlation with experiment

The correlation coefficient is calculated for all the 55 numerical responses with all three different coding schemes. The results of the model-experimental correlation between model

areas and the three different codings of the experimental data are shown in Figs. 116-118.

(a) Coding Scheme 1

Bond Skid [μm]	Bond Force [gf] 30	40	50	60	70	Bond Scrub Amplitude [μm]
5	1	1	1	1	2	1
0	1	1	1	1	1	
-5	1	1	1	1	1	
5	1	1	2	2	2	3
0	1	1	1	1	1	
-5	1	1	1	1	1	
5	2	2	2	2	2	5
0	1	2	2	2	2	
-5	1	1	1	2	2	

(b) Coding Scheme 2

Bond Skid [μm]	Bond Force [gf] 30	40	50	60	70	Bond Scrub Amplitude [μm]
5	1	1	1	1	1	1
0	1	1	1	1	1	
-5	1	1	1	1	1	
5	1	1	1	1	1	3
0	1	1	1	1	1	
-5	1	1	1	1	1	
5	1	1	1	2	2	5
0	1	1	1	1	1	
-5	1	1	1	1	1	

(c) Coding Scheme 3

Bond Skid [μm]	Bond Force [gf] 30	40	50	60	70	Bond Scrub Amplitude [μm]
5	1	1	1	1	2	1
0	1	1	1	1	1	
-5	1	1	1	1	1	
5	1	1	2	2	2	3
0	1	1	1	1	1	
-5	1	1	1	1	1	
5	2	2	2	3	3	5
0	1	2	2	2	2	
-5	1	1	1	2	2	

Fig. 114 Experimental responses with the coded status for the sake of the model-experiment correlation (a) Code 1, non-sticking and sticking (b) Code 2, tail lifting and non-tail lifting, (c) Code 3, non-sticking, sticking, and tail lifting.

Candidate responses can be divided into direct and indirect. The indirect responses are derived from some direct responses using a formula. The candidate responses number 1 to number 7 are direct, and from number 8 to number 55 are indirect. For the indirect ones, the formula is provided below. The details of number 1 to number 55 numerical responses are presented in Appendix A. Two examples of such numerical responses are given here, while the remaining 53 can be found in Appendix A.

1. Average of sliding distance of wire per wire wedge area and sliding distance of substrate per substrate wedge area (SES_{12}) [1/μm^2]

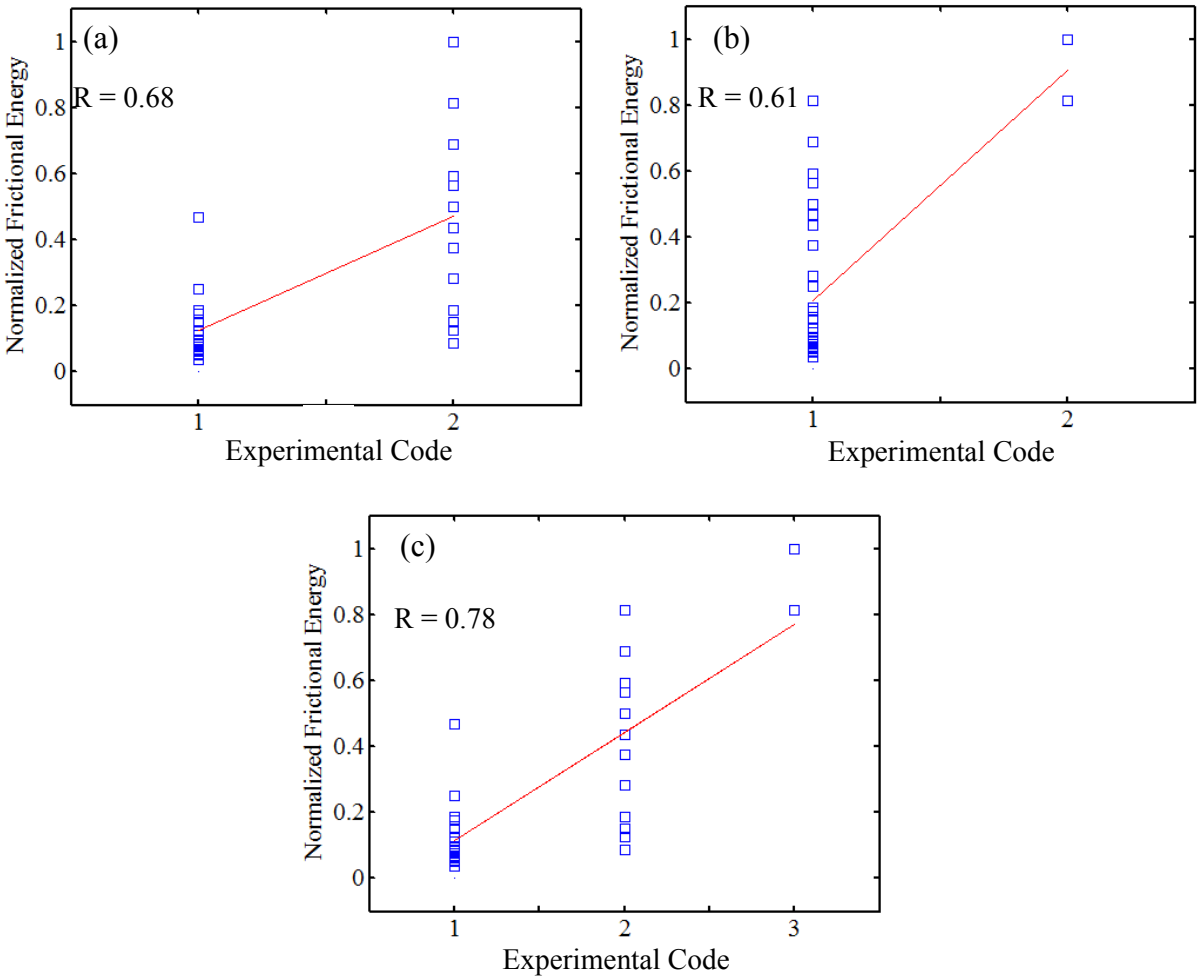

Fig. 115 Example model - experimental correlation between frictional energy produced in the model and the experimental (a) coding 1, (b) coding 2, and (c) coding 3.

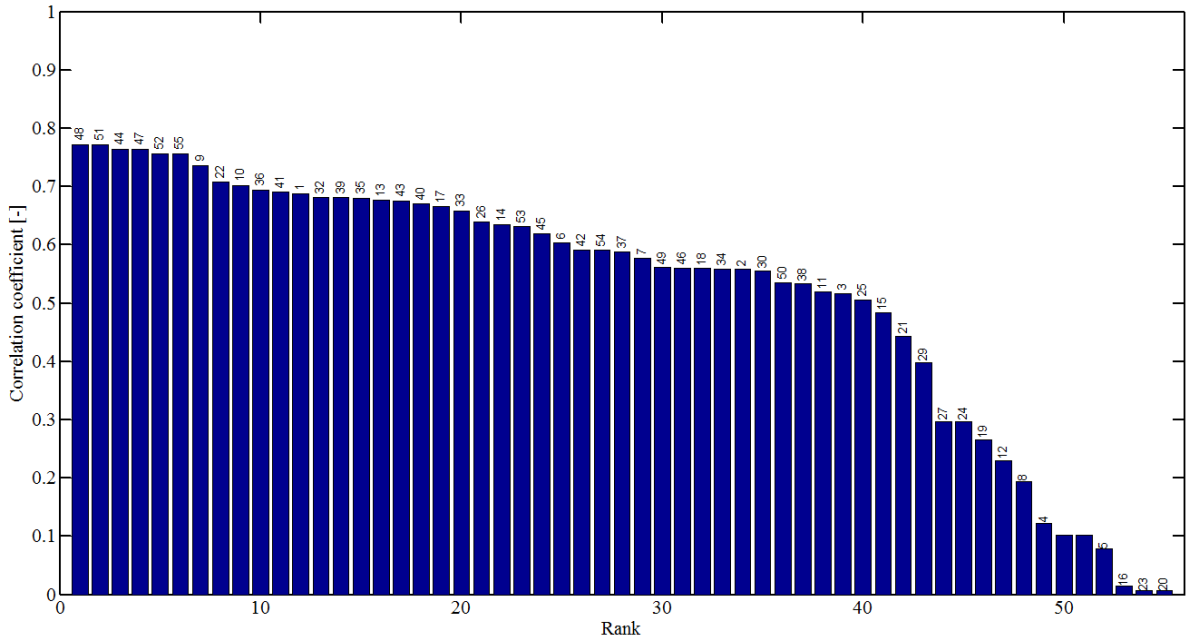

Fig. 116 Model-experimental correlation between model responses and the experimental data with coding 1.

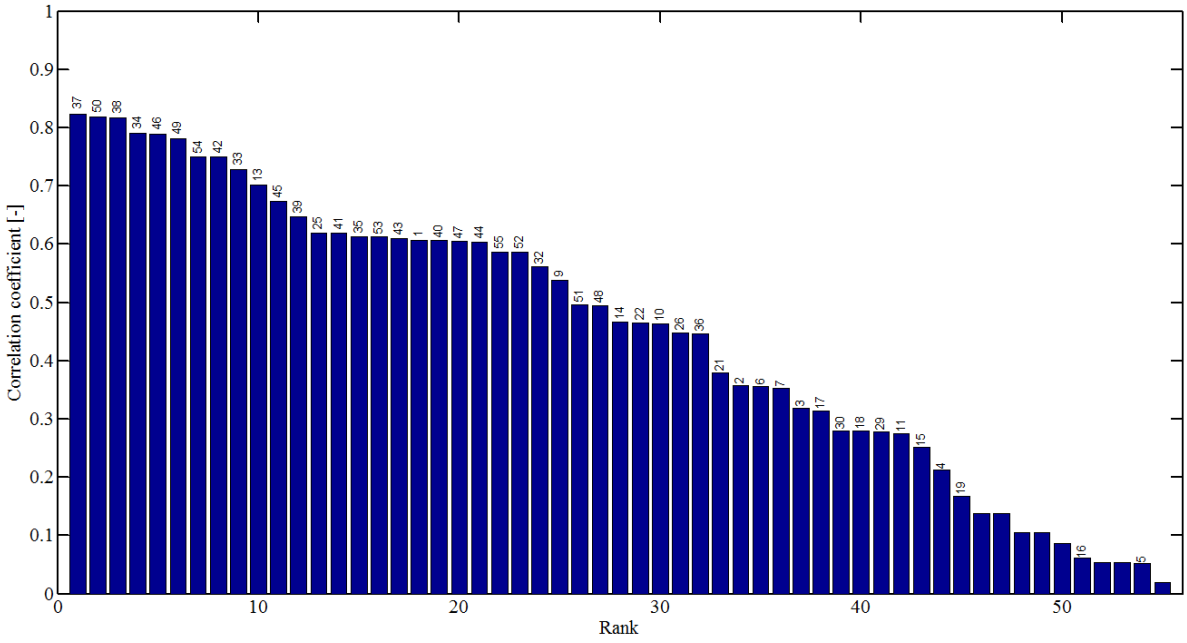

Fig. 117 Model-experimental correlation between model responses and the experimental data with coding 2.

$$SES_{12} = \frac{1}{average(A_{WW}, A_{WS})} \cdot \frac{1}{n} \cdot \frac{1}{2} \sum_{1}^{n} [(SD)^{Wire} + (SD)^{Substrate}] \tag{25}$$

2. Equivalent plastic strain of wire per wire contact area ($FESEP_1$) multiplied by frictional energy [µJ/µm^2]

$$FESEP_1 = \frac{FE}{A_{CW}} \cdot \frac{1}{n} \cdot \sum_{1}^{n} (PS)^{wire} \tag{26}$$

Considering the coding 1 of the experimental data, the non-sticking and sticking responses are only of interest. With such coding, the following six responses result in the best model-experiment correlations:

1. Sliding distance of wire per wire tail area ($FESES_2$) multiplied by frictional energy [µJ/µm] with R = 0.77

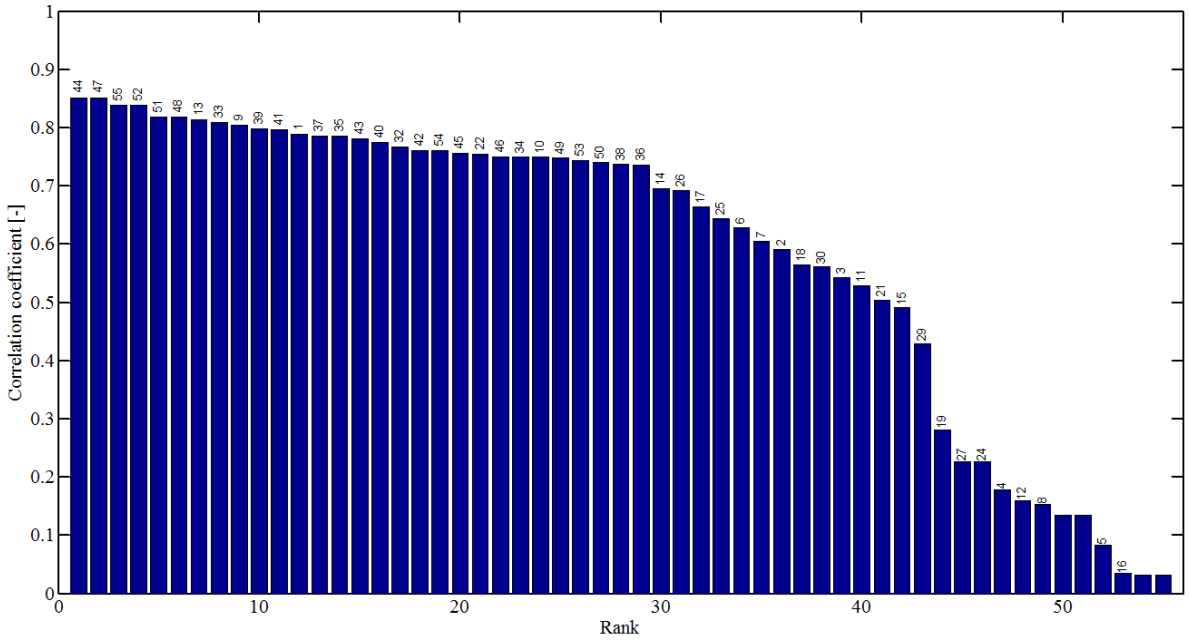

Fig. 118 Model-experimental correlation between model responses and the experimental data with coding 3.

2. Average of sliding distance of wire per wire tail area and sliding distance of substrate per substrate tail area ($FESES_{11}$) multiplied by frictional energy [µJ/µm2] with R = 0.77

3. Sliding distance of wire per wire contact area ($FESES_{1}$) multiplied by frictional energy [µJ/µm] with R = 0.76

4. Average of sliding distance of wire per wire contact area and sliding distance of substrate per substrate contact area ($FESES_{10}$) multiplied by frictional energy [µJ/µm^2] with R = 0.76

5. Sliding distance of wire per wire wedge area ($FESES_{3}$) multiplied by frictional energy [µJ/µm] with R = 0.75

6. Average of sliding distance of wire per wire wedge area and sliding distance of substrate per substrate wedge area ($FESES_{12}$) multiplied by frictional energy [µJ/µm^2] with R = 0.75

Considering the coding 2 of the experimental data, the non-tail lifting and tail lifting responses are only of interest. With such coding, the following six responses result in the best model-experiment correlations:

1. Equivalent plastic strain of substrate per substrate tail area ($FESEP_{5}$) multiplied by frictional energy [µJ/µm^2] with R = 0.82

2. Combination of sliding distance of wire per wire tail area and sliding distance of substrate per substrate tail area ($FESES_{8}$) multiplied by frictional energy [µJ/µm^2] with R = 0.81

3. Combination of equivalent plastic strain of wire per wire tail area and equivalent plastic strain of substrate per substrate tail area ($FESEP_{8}$) multiplied by frictional energy [µJ/µm^2] with R = 0.81

4. Combination of equivalent plastic strain of wire per wire contact area and equivalent plastic strain of substrate per substrate contact area ($FESEP_{7}$) multiplied by frictional energy [µJ/µm^2] with R = 0.79

5. Combination of sliding distance of wire per wire contact area and sliding distance of substrate per substrate contact area ($FESES_7$) multiplied by frictional energy [µJ/µm] with R = 0.78

6. Sliding distance of substrate per substrate tail area ($FESES_5$) multiplied by frictional energy [µJ/µm] with R = 0.78

Considering the coding 3 of the experimental data, the non-sticking, sticking, and tail lifting are all of interest. With such coding, the following six responses result in the best model-experiment correlations:

1. Sliding distance of wire per wire contact area ($FESES_1$) multiplied by frictional energy [µJ/µm] with R = 0.85

2. Average of sliding distance of wire per wire contact area and sliding distance of substrate per substrate contact area ($FESES_{10}$) multiplied by frictional energy [µJ/µm^2] with R = 0.85

3. Average of sliding distance of wire per wire wedge area and sliding distance of substrate per substrate wedge area ($FESES_{12}$) multiplied by frictional energy [µJ/µm^2] with R = 0.83

4. Sliding distance of wire per wire wedge area ($FESES_3$) multiplied by frictional energy [µJ/µm] with R = 0.83

5. Average of sliding distance of wire per wire tail area and sliding distance of substrate per substrate tail area ($FESES_{11}$) multiplied by frictional energy [µJ/µm^2] with R = 0.81

6. Sliding distance of wire per wire tail area ($FESES_2$) multiplied by frictional energy [µJ/µm] with R = 0.81

5•4 Numerical process window

Once the correlating numerical responses are found, it is possible to find a numerical process window. To do this, the most correlating response of the coding 1, sliding distance of wire per

wire tail area multiplied by frictional energy [µJ/µm], is selected to predict sticking (Stitch Response). The fact that a response extracted from tail region provides the best correlation for the stitch responses rather than a response extracted from wedge region might look controversial at the first glance. There are two possible causes of this controversy. First, the difference between correlation coefficient of the current best correlating response extracted from the tail region (#48) and that taken from the wedge region (#52) is less than 2%, and therefore less than the typical uncertainty associated with FE simulations. Second, there might be a real physical phenomena. For example, it might indicate that the bond formation is stronger or more susceptible to form at regions close to tail region, and reflected in high correlation between experimental sticking and model response extracted from the tail region.

In addition to the stitch response, the best correlating response of the coding 2, equivalent plastic strain of substrate per substrate tail area multiplied by frictional energy [µJ/µm^2] is selected to predict the tail lifting (Tail Response). Both of these model output responses are normalized between 0 and 1 to allow for a comparison. For the stitch response, "0" output means non-sticking, i.e. 0% chance of sticking, and "1" output means 100% chance of sticking. Similarly, for the tail response, "0" output means 0% chance of tail lifting and "1" output means 100% chance of tail lifting. The contour plots of the stitch response and tail response as a function of skid and scrub amplitude are shown in Fig. 119 for a bond force of 70 gf. To produce a numerical process window, arbitrarily levels are assigned for stitch and tail

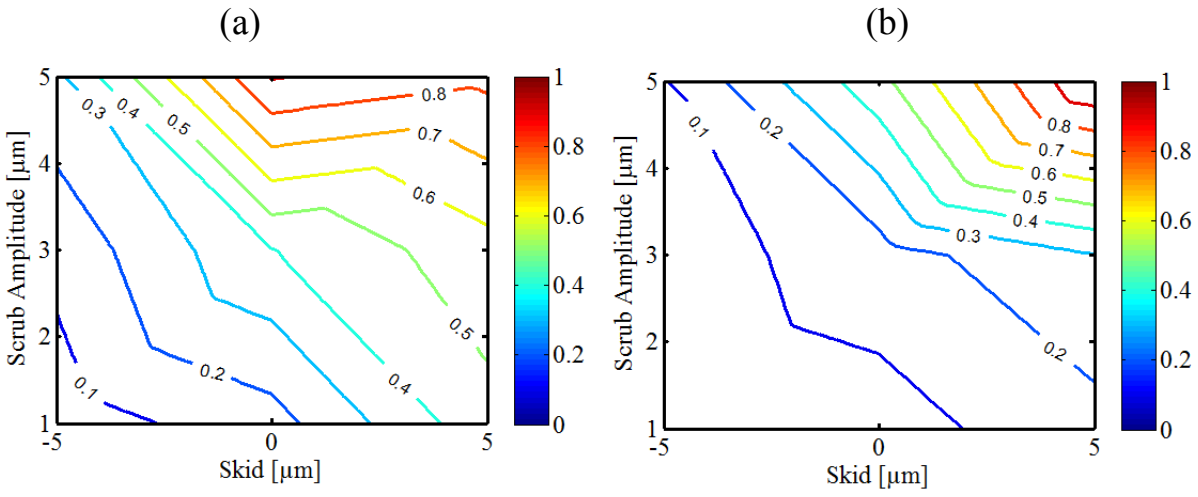

Fig. 119 Contour plot of the model responses vs scrub amplitude and skid for bond force equal to 70 gf (a) normalized stitch response (b) normalized tail response. A larger number in each of the responses means a higher tendency.

responses. These levels can be defined by experienced engineers depending on the level of importance of each of the tail or stitch responses for their applications. For example, one can select a level of 0.5. So it means that we are looking for process parameters that result in more than 50% chance of sticking and less than 50% chance of tail lifting. Such process windows are plotted for 30, 40, 50, 60, and 70 gf bond forces in Figs. 120 (a) to (d). This process window can be a representative of the specific experimental results used in this work, and to predict the stitch bond outcomes. Similar plots can be reproduced to understand how sensitive such process window is to the variations in the material properties, bonding tool geometries, substrate geometry, or process parameters.

5•5 Discussion

In this chapter, a FE model of the stitch bond is presented and its results are compared with experimental observation. To search for correlations between the model and the experiment, it

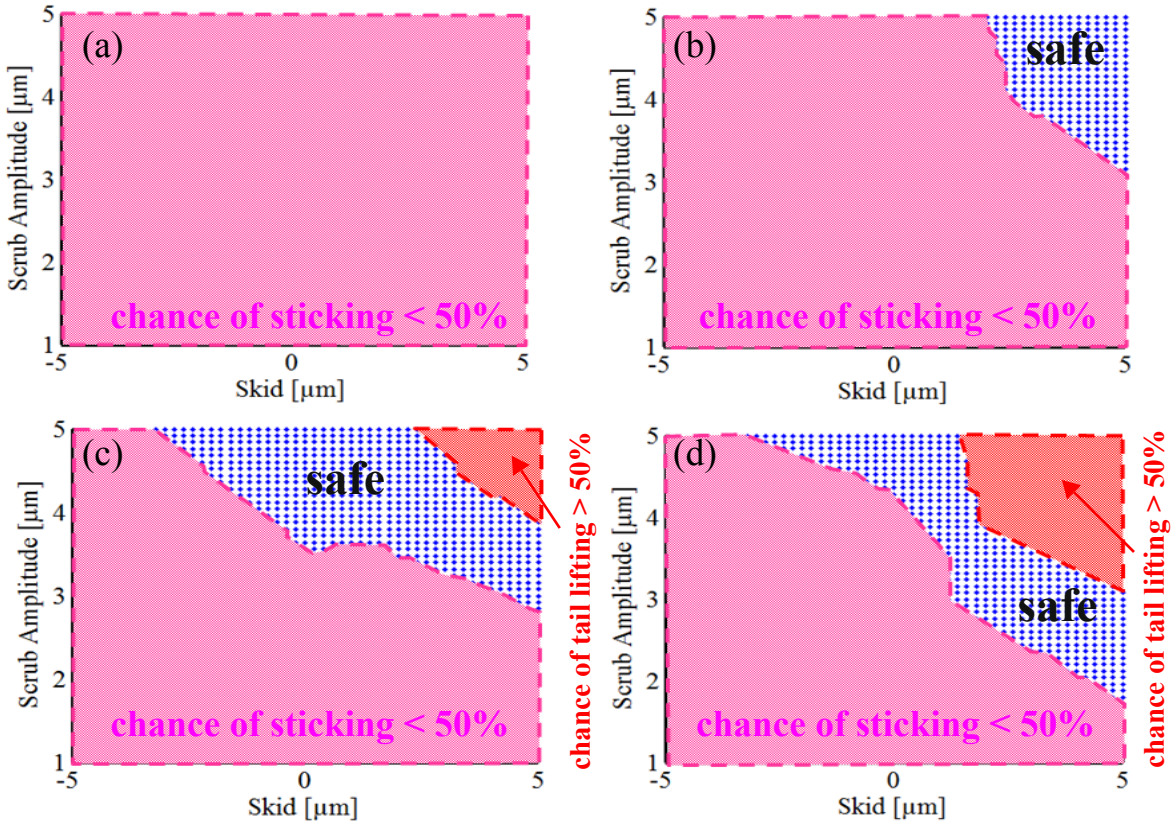

Fig. 120 Process windows for a process which could result in more than 50% chance of sticking and less than 50% chance of tail lifting (a) bond force of 30 and 40 gf (b) bond force of 50 gf (c) bond force of 60 gf (d) bond force of 70 gf.

was needed to extract nodal coordinates of the model part, filter the contact nodes, extract proper model outputs, build up candidate responses, and compare the candidate responses with coded experimental results. Performing such steps, correlations are found that made it possible to represent a process window for the current PCC wire on PPF QFN substrate bonding. The procedure to find the process window could be an asset for process engineers to improve the stitch bond process. In addition, using a numerical approach, it would be possible to understand or predict the effect of parameters which are sometimes hard to change experimentally. Examples of these parameters could be friction coefficients of the bonding materials, geometry of capillary tool, and thickness of substrate. Having developed a FE model for testing these different conditions by a PC with software is the main contribution of this work. However, remains room for improvement. For example, some assumptions and simplifications might cause the model responses to deviate from a real bond process. These assumptions could include a lack of mechanisms, to the lack of considering of thermal analysis, and the lack of considering the full size of important machine components instead of only partially including the capillary, wire, and substrate.

For the current model, some modifications can enhance its usefulness. For example:

1. Replacing the current parts with the full size bond head, and then compare with the current results.
2. Adding thermal analysis to the current mechanical model.
3. Replacing the substrate piece with a more complete substrate (e.g. including a complete leadframe finger).

With such modifications implemented into the model, a better correlation is expected. In addition, another possible useful next step would be to run the model for a high bondability substrate, and compare the FE model responses not only with the non-sticking, sticking, and tail lifting occurrences, but with real stitch pull force and tail pull force.

6 Conclusions and Outlook

Section 6•1 contains the conclusions of this research and section 6•2 the recommendations for future work.

6•1 Conclusions

The conclusions of this work are divided into three groups including Test I (process window), Test II (optimization), and numerical-experimental correlation.

Experimental Process Window for a Low Bondability Substrate

When stitch bonding on a low bondability substrate, increasing bonding force and scrub amplitude, and using positive skid levels increase the chance of sticking along with increasing the chance of tail-lifting failure. Considering these observations, it is possible to find proper process parameters sets for successful stitch bonding on low bondability substrates. For example, it is possible to keep the bond force and scrub amplitude at high levels to ensure a high chance of sticking, and reduce the skid level to negative values to ensure a strong enough tail bond.

Stitch Bonding Process Optimization for a High Bondability Substrate

Stitch bonding on a high bondability substrate showed significantly different influence of process parameters comparing with the results from the low bondability substrate. For example, increasing scrub amplitude increases the chance of sticking for low bondability substrate but it reduces the stitch pull force of bonds made on high bondability substrate. In addition, while a positive skid increases the chance of sticking and tail-lifting for low-bondability substrate, it decreases both the stitch and tail pull forces for a high bondability substrate. In conclusion finding a general model for stitch bonding quality prediction is difficult, maybe impossible. The effect of process parameters on stitch bonding responses obviously depends strongly on the materials used for individual stitch bonding applications.

Model - Experimental Correlation

A numerical FE model is successfully developed for the stitch bonding process. For the first time a relatively strong correlation between a numerical model and stitch bonding process responses is found. Two mechanisms widely accepted in ultrasonic and cold welding are also

relevant in the FE model: expansion of the faying surfaces and sliding friction at the interface. In particular, combining two mechanisms resulted in correlation.

Friction energy generated at contact interface helps bonding by removing surface contamination layers and bringing fresh metals together by an improved cleaning due to the relative motion. This mechanism is implemented into the model extracting the accumulated friction energy during modeling.

Surface expansions at the contact interface can break the surface contamination and oxide layers and open up cracks in the surface and bringing fresh metals together. This mechanism is implemented into the model by extracting the plastic strains at sliding distances at the contact interface and building up custom numerical candidate responses.

The friction energy and surface expansion related candidate responses did not result in the best correlation coefficients when considered as the only mechanism. However, a combination of them results in the best correlation coefficient. In conclusion, a sufficient surface expansion and a sufficient friction energy are equally important to have a successful stitch bond.

The best correlating response for sticking is extracted from the tail region of the bond. It indicates that the tail region (below the capillary chamfer) has a significant role in the final bond. This is in accordance with the experimental observation of tail-lifting at the excessive amounts of the same parameters that encouraged the sticking. The best six correlating responses for sticking are extracted from wire only or average of wire and substrate. Considering the much greater values of surface expansions for wire than substrate, it could be concluded that the wire has a more significant influence on bonding than the substrate.

The best correlating responses for tail-lifting is extracted from the tail region of the substrate. While observing the tail region to be the determining region for the tail-lifting is expectable, the observation of the substrate to be more correlating than wire indicates its higher importance for the tail-lifting issue.

The numerical model is able to produce numerical process windows to provide a proper process parameter selection. The high sensitivity of the numerical process window to process parameters and its irregular shape at various forces confirms the complexity of the stitch

bonding process, and indicates that the existence of such numerical process windows can be crucially helpful for proper process designs for different applications, materials, tool, and geometries. In addition, they can potentially be used to develop similar models for other solid - state cold welding processes.

6•2 Outlook

The following topics are for future research:

1. The full geometry of bond head is not considered in this study. Such a consideration can be helpful to understand the effect of different bond head geometries and materials on the stitch bonding process, and to investigate the effect of wire bonding loop direction on the stitch bond.

2. The capillary used in this study is a rigid portion of capillary tip. To improve the model, it is possible to consider the whole body of capillary as a deformable solid. This consideration, can reveal the effect of capillary body types and materials on the stitch bond quality.

3. Implementing more sophisticated mesh generation techniques such as arbitrary Lagrangian Eulerian (ALE) or adaptive meshing techniques can reduce the mesh distortion. Such an improvement could enhance the accuracy of the model results.

4. In this research, QFN substrate is considered as a cut piece of one finger. Including the full geometry of the QFN substrate with the fingers and the tape, could improve the model responses, and reveal information about the relative sliding between tape and substrate and the bouncing effects of fingers, and their effects on the bond quality.

5. Adding thermal analysis to investigate the contribution of bonding temperature on the wire deformation during modeling, and consequently the final quality of the stitch bond.

Bibliography

[1] Vardaman, E. J., "Drivers for Advanced Packaging", Proceedings of 2013 TechSearch International, Inc. A, 2012 available at: http://semieurope.omnibooksonline.com/2013/semicon_europa/Advanced_Packaging_Conference/11_Jan%20Vardaman_TechSearch.pdf. Reference is retrieved by September 2013.

[2] Chauhan, Preeti S., Anupam Choubey, ZhaoWei Zhong, and Michael G. Pecht. "Copper Wire Bonding." In Copper Wire Bonding, pp. 1-9. Springer New York, 2014.

[3] E. J. Vardaman (2007, July), "Advanced packaging interconnect trends and technology development" K&S interconnect technology symposium. [Online]. Available: http://www.kns.com/_temp/downloads/agendaJuly2007/1.pdf. Reference is retrieved by September 2013. Reference is retrieved by September 2013.

[4] Harman, George G. Wire bonding in microelectronics: materials, processes, reliability, and yield. Vol. 2. New-York, NY, USA: McGraw-Hill, 1997.

[5] Ho, Hong Meng. "Advanced copper wire bonding technology." In Electronic Manufacturing Technology Symposium (IEMT), 2010 34th IEEE/CPMT International, pp. 1-2. IEEE, 2010.

[6] Yauw, Oranna, Horst Clauberg, Kuan Fang Lee, Liming Shen, and Bob Chylak. "Wire bonding optimization with fine copper wire for volume production." In Electronics Packaging Technology Conference (EPTC), 2010 12th, pp. 467-472. IEEE, 2010.

[7] Zhong, Z. W. "Wire bonding using copper wire." Microelectronics International 26, no. 1 (2009): 10-16.

[8] Zhong, Z. W. "Overview of wire bonding using copper wire or insulated wire." Microelectronics Reliability 51, no. 1 (2011): 4-12.

[9] Rezvani, A., A. Shah, M. Mayer, Y. Zhou, and J. T. Moon. "Role of impact ultrasound on bond strength and Al pad splash in Cu wire bonding." Microelectronics Reliability (2013).

[10] Palesko, Chet A., and E. Jan Vardaman. “Cost comparison for flip chip, gold wire bond, and copper wire bond packaging.” In Electronic Components and Technology Conference (ECTC), 2010 Proceedings 60th, pp. 10-13. IEEE, 2010.

[11] Zhang, Changliang, Yingwei Jiang, Zhijie Wang, and Wei Xiao. “Method of forming wire bonds in semiconductor devices.” U.S. Patent 8,198,737, issued June 12, 2012.

[12] Qin, Ivy W., Bob Chylak, Horst Clauberg, Aashish Shah, and John Foley. “Ball Bond Process Optimization with Cu and Pd-Coated Cu Wire.” ECS Transactions 44, no. 1 (2012): 891-901.

[13] Tracy, Daniel P. “Packaging Materials Trends and Outlook.” ECS Transactions 44, no. 1 (2012): 871-875.

[14] Schwizer, Jürg, Michael Mayer, and Oliver Brand. Force sensors for microelectronic packaging applications. Springer, 2004.

[15] Eng, Tan Chee, Pan Yen Jeat, Chin Meei Lian, Chin Lap Sin, and G. Fonseka. “QFN assembly dilemma-solutions.” In Electronic Materials and Packaging, 2007. EMAP 2007. International Conference on, pp. 1-5. IEEE, 2007.

[16] Looe, Siew Han, Soon Wei Wang, and Azhar Aripin. “Methods to Resolve Heel Stress for Ultra Thin QFN Small Package.” In Electronic Manufacturing Technology Symposium, 2007. IEMT'07. 32nd IEEE/CPMT International, pp. 28-33. IEEE, 2007.

[17] Eng, Tan Chee, and Geale Fonseka. “QFN Miniaturization: Challenges and Solutions.” In Electronics Manufacturing and Technology, 31st International Conference on, pp. 314-319. IEEE, 2007.

[18] Srikanth, Narasimalu. “Effects of die-pad resonance on ultrasonic bond quality of wire bonds.” Microelectronics international 24, no. 1 (2007): 23-26.

[19] Tee, C. L., and A. Pascual. “Impact of quad flat no lead package (QFN) on automated X-ray inspection.” In Proceedings of the IEEE International Test Conference, pp. 1-10. 2007.

[20] Eng, Tan Chee, Pan Yen Jeat, and G. Fonseka. “QFN Wire Bond Dilemma-Stress Neck & Stress Heel.” In Electronics Packaging Technology Conference, 2007. EPTC 2007. 9th, pp. 192-195. IEEE, 2007.

[21] Li, Li. “Reliability modeling and testing of advanced QFN packages.” In Electronic Components and Technology Conference (ECTC), 2013 IEEE 63rd, pp. 725-730. IEEE, 2013.

[22] Song, Meijiang, Jinzhong Yao, and Yongsheng Lu. “Failure Mechanism and Solution Study of IC Wire Bond Heel Crack on Leadframe.” In Electronics Packaging Technology Conference, 2008. EPTC 2008. 10th, pp. 1214-1219. IEEE, 2008.

[23] Wei, Tan Boo, and Ken Niu. “Study of Factors Contributing to Robust Copper Wire Bond on QFN.” ECS Transactions 44, no. 1 (2012): 985-989.

[24] Prasad, Shankara K. Advanced wirebond interconnection technology. Springer, 2004.

[25] ILum, Ivan. “Effects of ultrasound in microelectronic ultrasonic wire bonding.” (2007).

[26] Drozdov, M., G. Gur, Z. Atzmon, and W. D. Kaplan. “Detailed investigation of ultrasonic Al–Cu wire-bonds: II. Microstructural evolution during annealing.” Journal of materials science 43, no. 18 (2008): 6038-6048.

[27] Palaganas, Jerome. “Comparative Analyses between Bare Cu Wire and Palladium Coated Cu Wire Performance in IC Packaging Assembly.”

[28] Lim, Adeline BY, Andrew CK Chang, Chee Xian Lee, Oranna Yauw, Bob Chylak, and Zhong Chen. “Palladium-Coated and Bare Copper Wire Study for Ultra-Fine Pitch Wire Bonding.” ECS Transactions 52, no. 1 (2013): 717-730.

[29] Araki, Noritoshi, Yasutomo Ichiyama, Ryo Oishi, and Takashi Yamada. “A study of free air ball formation in palladium-coated copper and bare copper bonding wire.” In Electronic Components and Technology Conference (ECTC), 2013 IEEE 63rd, pp. 1556-1563. IEEE, 2013.

[30] Xu, Hui, Ivy Qin, Horst Clauberg, Bob Chylak, and Viola L. Acoff. "Behavior of palladium and its impact on intermetallic growth in palladium-coated Cu wire bonding." Acta Materialia (2012).

[31] Chang, A. C. K., A. B. Y. Lim, C. X. Lee, B. Milton, H. Clauberg, O. Yauw, and B. Chylak. "Characterization of a Wire Bonding Process with the Added Challenges from Palladium-coated Copper Wires." (2012).

[32] Song, W. H., M. Mayer, Y. Zhou, S. H. Kim, J. S. Hwang, and J. T. Moon. "Effect of EFO parameters and superimposed ultrasound on work hardening behavior of palladium coated copper wire in thermosonic ball bonding." Microelectronics Reliability 52, no. 11 (2012): 2744-2748.

[33] Breach, C. D., and F. W. Wulff. "A brief review of selected aspects of the materials science of ball bonding." Microelectronics Reliability 50, no. 1 (2010): 1-20.

[34] Qin, Ivy, Hui Xu, Horst Clauberg, Ray Cathcart, Viola L. Acoff, Bob Chylak, and Cuong Huynh. "Wire bonding of Cu and Pd coated Cu wire: Bondability, reliability, and IMC formation." In Electronic Components and Technology Conference (ECTC), 2011 IEEE 61st, pp. 1489-1495. IEEE, 2011.

[35] Lee, J., M. Mayer, Y. Zhou, S. J. Hong, and J. T. Moon. "Concurrent optimization of crescent bond pull force and tail breaking force in a thermosonic Cu wire bonding process." Electronics Packaging Manufacturing, IEEE Transactions on 32, no. 3 (2009): 157-163.

[36] Kumar, B. Senthil, Mohandass Sivakumar Ramkumar Malliah, Li Ming, Song Keng Yew, and J. James. "Process characterization of Cu & Pd coated Cu wire bonding on overhang die: Challenges and solution." In Electronics Packaging Technology Conference (EPTC), 2010 12th, pp. 859-867. IEEE, 2010.

[37] Tok, C. W., I. Langut, A. Menache, D. R. M. Calpito, and Y. H. Chew. "Wire bonding Improvement through optimal bonding tools and materials bonding." In Electronics Packaging Technology Conference, 2007. EPTC 2007. 9th, pp. 743-749. IEEE, 2007.

[38] Goh, K. S., and Z. W. Zhong. “A new bonding-tool solution to improve stitch bondability.” Microelectronic Engineering 84, no. 1 (2007): 173-179.

[39] Goh, K. S., and Z. W. Zhong. “Two capillary solutions for ultra-fine-pitch wire bonding and insulated wire bonding.” Microelectronic Engineering 84, no. 2 (2007): 362-367.

[40] Lee, J., M. Mayer, Y. Zhou, and S. J. Hong. “Iterative optimization of tail breaking force of 1mil wire thermosonic ball bonding processes and the influence of plasma cleaning.” Microelectronics Journal 38, no. 8 (2007): 842-847.

[41] Test Method Standards for Microcircuits available at: http://www.q-tech.com/assets/tests/std883_2011.pdf. Reference is retrieved by September 2013.

[42] “TEST METHOD FOR PULL STRENGTH FOR WIRE BONDING,” Standard,. SEMI G73-0997, 1997.

[43] Brunner, “Tail bond strength measurement - feasibility report” K&S internal report,1999.

[44] Lee, J., M. Mayer, Y. Zhou, and S. J. Hong. “Iterative optimization of tail breaking force of 1mil wire thermosonic ball bonding processes and the influence of plasma cleaning.” Microelectronics Journal 38, no. 8 (2007): 842-847.

[45] Hang, C. J., W. H. Song, I. Lum, M. Mayer, Y. Zhou, C. Q. Wang, J. T. Moon, and J. Persic. “Effect of electronic flame off parameters on copper bonding wire: Free-air ball deformability, heat affected zone length, heat affected zone breaking force.” Microelectronic engineering 86, no. 10 (2009): 2094-2103.

[46] Mayer, Michael, J. Lee, Y. Zhou, S. J. Hong, and S. M. Lee. “Tail breaking force in thermosonic wire bonding with novel bonding wires.” In Materials Science Forum, vol. 580, pp. 201-204. 2008.

[47] Mayer, Michael, J. Lee, Y. Zhou, S. J. Hong, and S. M. Lee. “Tail breaking force in thermosonic wire bonding with novel bonding wires.” In Materials Science Forum, vol. 580, pp. 201-204. 2008.

[48] Shah, Aashish, Jaesik Lee, Michael Mayer, and Y. Norman Zhou. “Online methods to measure breaking force of bonding wire using a CMOS stress sensor and a proximity sensor.” Sensors and Actuators A: Physical 148, no. 2 (2008): 462-471.

[49] Lee, J., M. Mayer, Y. Zhou, and J. Persic. “Pull force and tail breaking force optimization of the crescent bonding process with insulated Au wire.” In Electronics Packaging Technology Conference, 2007. EPTC 2007. 9th, pp. 725-730. IEEE, 2007.

[50] Lee, J., M. Mayer, Y. Zhou, S. J. Hong, and J. T. Moon. “Silver pick-up during tail formation and its effect on free air ball in thermosonic copper ball bonding.” In Electronic Components and Technology Conference, 2008. ECTC 2008. 58th, pp. 2024-2029. IEEE, 2008.

[51] Lee, J., M. Mayer, Y. Zhou, J. T. Moon, and J. Persic. “Influence of gold pick up on the hardness of copper free air ball.” Microelectronics Reliability 51, no. 1 (2011): 30-37.

[52] Fujimoto, K., S. Nakata, T. Manabe, and A. Fujii. “Effects of bonding conditions and surface state on bondability: Study of Cu wire stitch bonding (1st Report).” (1996): 705-710.

[53] Fujimoto, K., S. Nakata, Y. Masutani, and A. Fujii. “Effects of wire deformation behaviour on bondability: Study of Cu wire stitch bonding (2nd Report).” (1996): 711-716.

[54] Ji, Hongjun, Mingyu Li, and Chunqing Wang. “Interfacial Characterization and Bonding Mechanism of Ultrasonic Wedge Bonding.” In Electronic Packaging Technology, 2006. ICEPT'06. 7th International Conference on, pp. 1-5. IEEE, 2006.

[55] Lee, J., M. Mayer, Y. Zhou, S. J. Hong, and J. T. Moon. “Concurrent optimization of crescent bond pull force and tail breaking force in a thermosonic Cu wire bonding process.” Electronics Packaging Manufacturing, IEEE Transactions on 32, no. 3 (2009): 157-163.

[56] TIAN, Yan-hong, Chun-qing WANG, and Y. Norman ZHOU. “Bonding mechanism of ultrasonic wedge bonding of copper wire on Au/Ni/Cu substrate.” Transactions of Nonferrous Metals Society of China 18, no. 1 (2008): 132-137.

[57] Geissler, Ute, Jürgen Funck, Martin Schneider-Ramelow, Hans-Jürgen Engelmann, Ingrid Rooch, Wolfgang H. Müller, and Herbert Reichl. "Interface formation in the US-wedge/wedge-bond process of AlSi1/CuNiAu contacts." Journal of electronic materials 40, no. 2 (2011): 239-246.

[58] Ji, Hongjun, Mingyu Li, Chunqing Wang, Jongmyung Kim, and Daewon Kim. "Nanoscale analysis of ultrasonic wedge bond interface by using high-resolution transmission electron microscopy." In Electronic Packaging Technology & High Density Packaging, 2008. ICEPT-HDP 2008. International Conference on, pp. 1-5. IEEE, 2008.

[59] Liu, Xingjie, Techun Wang, Yuqi Cong, and Jiaji Wang. "Study on interface of Pd-plated Cu wire stitch bonding." In Advanced Packaging Materials (APM), 2011 International Symposium on, pp. 213-219. IEEE, 2011.

[60] Gao, Shixin, Zhuo Chen, Anmin Hu, Ming Li, and Kaiyou Qian. "Electrode posited Ni microcones with a thin Au film bonded with Au wire." Journal of Materials Processing Technology 214, no. 2 (2014): 326-333.

[61] Lin, Yung-Sen. "A surface analysis on oxygen plasma-cleaned gold pattern-plated substrates for wire bondability." Surface and Coatings Technology 173, no. 1 (2003): 47-57.

[62] Lin, T. Y., W. S. Leong, K. H. Chua, R. Oh, Y. Miao, J. S. Pan, and J. W. Chai. "The impact of copper contamination on the quality of the second wire bonding process using X-ray photoelectron spectroscopy method." Microelectronics reliability 42, no. 3 (2002): 375-380.

[63] Hung, Liang Yi, Don Son Jiang, C. M. Huang, and Yu Po Wang. "Investigation of ultrasonic Pd coated Cu wire wedge bonding on different surface finish." In Electronics Packaging Technology Conference (EPTC), 2011 IEEE 13th, pp. 705-709. IEEE, 2011.

[64] Lim, L. A., Jimmy Castaneda, and Shinji Shirakawa. "Fine pitch copper wire bonding process and materials study." ASM publication.

[65] Goh, K. S., and Z. W. Zhong. "A new bonding-tool solution to improve stitch bondability." Microelectronic engineering 84, no. 1 (2007): 173-179.

[66] Goh, K. S., and Z. W. Zhong. “Two capillary solutions for ultra-fine-pitch wire bonding and insulated wire bonding.” Microelectronic Engineering 84, no. 2 (2007): 362-367.

[67] Mindlin RD. Compliance of elastic bodies in contact. J Appl Mech 1949;71:259–68

[68] Chen, Jian, Dominick Degryse, Petar Ratchev, and Ingrid De Wolf. “Mechanical issues of Cu-to-Cu wire bonding.” Components and Packaging Technologies, IEEE Transactions on 27, no. 3 (2004): 539-545.

[69] Hang, C. J., C. Q. Wang, M. Mayer, Y. H. Tian, Y. Zhou, and H. H. Wang. “Growth behavior of Cu/Al intermetallic compounds and cracks in copper ball bonds during isothermal aging.” Microelectronics reliability 48, no. 3 (2008): 416-424.

[70] Lum, I., M. Mayer, and Y. Zhou. "Footprint study of ultrasonic wedge-bonding with aluminum wire on copper substrate." Journal of electronic materials 35, no. 3 (2006): 433-442.

[71] Xu, Hui, Changqing Liu, Vadim V. Silberschmidt, Zhong Chen, and Jun Wei. “Initial bond formation in thermosonic gold ball bonding on aluminium metallization pads.” Journal of Materials Processing Technology 210, no. 8 (2010): 1035-1042.

[72] DEANGELIS, Dominick, and Gary SCHULZE. “ULTRASONIC TRANSDUCERS FOR WIRE BONDING AND METHODS OF FORMING WIRE BONDS USING ULTRASONIC TRANSDUCERS.” WIPO Patent 2011019692, issued February 18, 2011.

[73] Mohamed, H. A., and J. Washburn. “Mechanism of solid state pressure welding.” Welding Journal 54, no. 9 (1975): 302-310.

[74] Bay, Niels. “Cold Pressure Welding—The Mechanisms Governing Bonding.” Journal of Engineering for Industry 101 (1979): 121.

[75] Zhang, Wenqi, and Niels Bay. “Cold welding: experimental investigation of the surface preparation methods.” Welding journal 76, no. 8 (1997): 326-s.

[76] Zhang, Wenqi, and Niels Bay. “Cold welding-theoretical modeling of the weld formation.” Welding Journal-Including Welding Research Supplement 76, no. 10 (1997): 477s.

[77] Zhang, Wenqi, Niels Bay, and T. Wanheim. “Influence of hydrostatic pressure in cold-pressure welding.” CIRP Annals-Manufacturing Technology 41, no. 1 (1992): 293-297.

[78] Bay, Niels. “Mechanisms producing metallic bonds in cold welding.” WELDING J. 62, no. 5 (1983): 137.

[79] Li, Long, Kotobu Nagai, and Fuxing Yin. “Progress in cold roll bonding of metals.” Science and Technology of Advanced Materials 9, no. 2 (2008): 023001.

[80] Grunzweig, J., I. M. Longman, and N. J. Petch. “Calculations and measurements on wedge-indentation.” Journal of the Mechanics and Physics of Solids 2, no. 2 (1954): 81-86.

[81] Rezvani, A., C. Nan, M. Mayer, and I. Qin. “The role of friction coefficient on the stitch bondability in Pd coated Cu and bare Cu wire bonding.” In Electronic Components and Technology Conference (ECTC), 2012 IEEE 62nd, pp. 2150-2156. IEEE, 2012.

[82] McCulloch, Euan. “Experimental and finite element modelling of ultrasonic cutting of food.” PhD diss., University of Glasgow, 2008.

[83] Kraemer, F., P. Ritter, M. Moller, and S. Wiese. “Dynamic Three Dimensional Simulation of Wire Bonding Processes on Soft Polymeric Substrates for High Frequency Applications.” In Proceedings of the 4th Electronics System integration Technology Conference (ESTC), Amsterdam, The Netherlands, Sept, pp. 17-20, 2012

[84] Takahashi, Yasuo, Sigeru Shibamoto, and Katsunori Inoue. “Numerical analysis of the interfacial contact process in wire thermocompression bonding.” Components, Packaging, and Manufacturing Technology, Part A, IEEE Transactions on 19, no. 2 (1996): 213-223.

[85] Takahashi, Yasuo. “Numerical study of wire bonding-analysis of interfacial deformation between wire and pad.” J. Electronic Packaging, ASME 124 (2002): 27-36.

[86] Saiki, Hiroyuki, Yasuo Marumo, Hiroshi Nishitake, Tetsuhiro Uemura, and Takahiro Yotsumoto. “Deformation analysis of Au wire bonding.” Journal of materials processing technology 177, no. 1 (2006): 709-712.

[87] Saiki, Hiroyuki, Hiroshi Nishitake, Takahiro Yotsumoto, and Yasuo Marumo. “Deformation characteristics of Au wire bonding.” Journal of materials processing technology 191, no. 1 (2007): 16-19.

[88] Ding, Yong, and Jang-Kyo Kim. “Numerical analysis of ultrasonic wire bonding: Part 2. Effects of bonding parameters on temperature rise.” Microelectronics Reliability 48, no. 1 (2008): 149-157.

[89] Takahashi, Yasuo, Shinji Suzuki, Yusuke Ohyama, and Masakatsu Maeda. “Numerical analysis of interfacial deformation and temperature rise during ultrasonic Al ribbon bonding.” In Journal of Physics: Conference Series, vol. 379, no. 1, p. 012028. IOP Publishing, 2012.

[90] Viswanath, Akella GK, Xiaowu Zhang, V. P. Ganesh, and Lu Chun. “Numerical study of gold wire bonding process on Cu/low-k structures.” Advanced Packaging, IEEE Transactions on 30, no. 3 (2007): 448-456.

[91] Liu, Yong, Scott Irving, Timwah Luk, Mark Rioux, and Qiuxiao Qian. “Impact of wedge wire bonding and thermal mechanical stress on reliability of BPSG/poly layer of a silicon die.” In Electronic Components and Technology Conference, 2008. ECTC 2008. 58th, pp. 1714-1718. IEEE, 2008.

[92] Huang, Yan, Aashish Shah, Michael Mayer, Norman Zhou, and John Persic. “Effect of ultrasonic capillary dynamics on the mechanics of thermosonic ball bonding.” Ultrasonics, Ferroelectrics and Frequency Control, IEEE Transactions on 57, no. 1 (2010): 241-252.

[93] Beleran, John D., Yang Yong Bo, Hyman G. Robles, Antonino Milanes, Alfred Yeo, and Chan Kai Chong. “Copper wire bond analysis: Pad design effects and process considerations.” In Electronic Components and Technology Conference (ECTC), 2012 IEEE 62nd, pp. 1124-1129. IEEE, 2012.

[94] Ding, Yong, and Jang-Kyo Kim. “Numerical analysis of ultrasonic wire bonding: Part 2. Effects of bonding parameters on temperature rise.” Microelectronics Reliability 48, no. 1 (2008): 149-157.

[95] Degryse, Dominiek, Bart Vandevelde, and Eric Beyne. “Mechanical FEM simulation of bonding process on Cu LowK wafers.” Components and Packaging Technologies, IEEE Transactions on 27, no. 4 (2004): 643-650.

[96] Jeon, Insu. “The study on failure mechanisms of bond pad metal peeling: Part B—Numerical analysis.” Microelectronics reliability 43, no. 12 (2003): 2055-2064.

[97] Chen, Zhaohui, Yong Liu, and Sheng Liu. “Modeling of copper wire bonding process on high power LEDs.” Microelectronics Reliability 51, no. 1 (2011): 171-178.

[98] Liu, Yong, Scott Irving, and Timwah Luk. “Thermosonic wire bonding process simulation and bond pad over active stress analysis.” In Electronic Components and Technology Conference, 2004. Proceedings. 54th, vol. 1, pp. 383-391. IEEE, 2004.

[99] Chen, Jian, Dominick Degryse, Petar Ratchev, and Ingrid De Wolf. “Mechanical issues of Cu-to-Cu wire bonding.” Components and Packaging Technologies, IEEE Transactions on 27, no. 3 (2004): 539-545.

[100] Ding, Yong, Jang-Kyo Kim, and Pin Tong. “Numerical analysis of ultrasonic wire bonding: Effects of bonding parameters on contact pressure and frictional energy.” Mechanics of materials 38, no. 1 (2006): 11-24.

[101] http://imapsaz.org/wp-content/uploads/2011/05/TechSearch%2520IMAPS%2520CuW-BHD1.pdf. Reference is retrieved by September 2013.

[102] Seltman, Howard J. “Experimental design and analysis.” Pittsburgh, PA: Carnegie Mellon University (2012).

[103] Myers, Raymond H., and Christine M. Anderson-Cook. Response surface methodology: process and product optimization using designed experiments. Vol. 705. Wiley. com, 2009.

[104] Poh, Christine Ng Bee, Tee Heng Ving, Tham Veng Leong, and Eric Neo Cheng Chye. "Process development of 17.5 µm gold wire bonding on C65 low-k devices with probe marks." In Electronics Packaging Technology Conference (EPTC), 2010 12th, pp. 359-363. IEEE, 2010.

[105] ASM Handbook Volume 02: Properties and Selection: Nonferrous Alloys and Special-Purpose Materials

[106] Abaqus, Inc. "ABAQUS Analysis: User's Manual." (2007).

[107] http://imechanica.org/files/l5-quasi-static.pdf. Reference is retrieved by September 2013.

[108] Rezvani, A., C. Nan, M. Mayer, and I. Qin. "The role of friction coefficient on the stitch bondability in Pd coated Cu and bare Cu wire bonding." In Electronic Components and Technology Conference (ECTC), 2012 IEEE 62nd, pp. 2150-2156. IEEE, 2012.

[109] ASME Annual Book of Standards: 4518-91. Standard test methods for measuring static coefficient of coating surfaces; 1991.

[110] Rezvani, A., M. Mayer, I. Qin, J. Brunner, and B. Chylak. "Stitch Bond Process of Pd-Coated Cu Wire: Experimental and Numerical Studies of Process Parameters and Materials." In International Microelectronics Assembly and Packaging Society Conference (IMAPS), 2013 46th.

[111] Ip, K., Rezvani, A., "Static Friction Coefficient Test at High Temperature", internal report at wire bonding group, university of waterloo, May 2012. Available at: \mijofem1\Alireza Rezvani

[112] Hang, C. J., I. Lum, J. Lee, M. Mayer, C. Q. Wang, Y. Zhou, S. J. Hong, and S. M. Lee. "Bonding wire characterization using automatic deformability measurement" Microelectronic Engineering 85, no. 8 (2008): 1795-1803.

[113] Huang, H., B. H. Chang, and D. Du. "Effect of superimposed ultrasound on mechanical properties of copper." Materials Science and Technology 27, no. 7 (2011): 1117-1122.

[114] Wang, Y. M., and E. Ma. “Temperature and strain rate effects on the strength and ductility of nanostructured copper.” Applied physics letters 83, no. 15 (2003): 3165-3167.

[115] Chakrabarty, Jagabanduhu. Theory of plasticity. Butterworth-Heinemann, 2006.

[116] Mayer, Michael, and Andrew Zwart. “Ultrasonic friction power in microelectronic wire bonding” In Materials science forum, vol. 539, pp. 3920-3925. 2007.

[117] Rezvani, Alireza, Collection of evaluation programs, UW/CAMJ local server “mijofem1\data\Alireza Rezvani”

Publications

1. Shah, A., A. Rezvani, M. Mayer, Y. Zhou, J. Persic, and J. T. Moon. “Reduction of ultrasonic pad stress and aluminum splash in copper ball bonding.” Microelectronics Reliability 51, no. 1 (2011): 67-74.

2. Rezvani, A., M. Mayer, A. Shah, N. Zhou, S. J. Hong, and J. T. Moon. “Free-air ball formation and deformability with Pd coated Cu wire.” In Electronic Components and Technology Conference (ECTC), 2011 IEEE 61st, pp. 1516-1522. IEEE, 2011.

3. Rezvani, A., C. Nan, M. Mayer, and I. Qin. “The role of friction coefficient on the stitch bondability in Pd coated Cu and bare Cu wire bonding.” In Electronic Components and Technology Conference (ECTC), 2012 IEEE 62nd, pp. 2150-2156. IEEE, 2012.

4. Rezvani, A., A. Shah, M. Mayer, Y. Zhou, and J. T. Moon. “Role of impact ultrasound on bond strength and Al pad splash in Cu wire bonding.” Microelectronics Reliability (2013).

5. Rezvani, A., M. Mayer, I. Qin, J. Brunner, and B. Chylak. “Stitch Bond Process of Pd-Coated Cu Wire: Experimental and Numerical Studies of Process Parameters and Materials.” In International Microelectronics Assembly and Packaging Society Conference (IMAPS), 2013 46th.

6. Moazenzadeh, A., N. Spengler, R. Lausecker, A. Rezvani, M. Mayer, J. G. Korvink, and U. Wallrabe. “Wire bonded 3D coils render air core microtransformers competitive.” Journal of Micromechanics and Microengineering 23, no. 11 (2013): 114020.

Appendix A:

The details of number 1 to number 55 numerical responses:

1. Frictional energy produced in the model (*FE*) [μJ]
2. Contact area of wire (A_{CW}) [μm^2]
3. Contact area of substrate (A_{CS}) [μm^2]
4. Tail area of wire (A_{TW}) [μm^2]
5. Tail area of substrate (A_{TS}) [μm^2]
6. Wedge area of wire (A_{WW}) [μm^2]
7. Wedge area of substrate (A_{WS}) [μm^2]
8. Equivalent plastic strain of wire per wire contact area (SEP_1) [$1/\mu m^2$]

$$SEP_1 = \frac{1}{A_{CW}} \cdot \frac{1}{n} \cdot \sum_{1}^{n} (PS)^{wire} \tag{27}$$

9. Equivalent plastic strain of substrate per substrate contact area (SEP_4) [$1/\mu m^2$]

$$SEP_4 = \frac{1}{A_{CS}} \cdot \frac{1}{n} \cdot \sum_{1}^{n} (PS)^{Substrate} \tag{28}$$

10. Combination of equivalent plastic strain of wire per wire contact area and equivalent plastic strain of substrate per substrate contact area (SEP_7) [$1/\mu m^2$]

$$SEP_7 = \frac{1}{(A_{CW} \cdot A_{CS})} \cdot \frac{1}{n} \sum_{1}^{n} [(PS)^{Wire} \cdot (PS)^{Substrate}] \tag{29}$$

11. Average of equivalent plastic strain of wire per wire contact area and equivalent plastic strain of substrate per substrate contact area (SEP_{10}) [1/μm^4]

$$SEP_{10} = \frac{1}{average(A_{CW}, A_{CS})} \cdot \frac{1}{n} \cdot \frac{1}{2} \sum_{1}^{n} [(PS)^{Wire} + (PS)^{Substrate}] \tag{30}$$

12. Equivalent plastic strain of wire per wire tail area (SEP_2) [1/μm^2]

$$SEP_2 = \frac{1}{A_{TW}} \cdot \frac{1}{n} \cdot \sum_{1}^{n} (PS)^{wire} \tag{31}$$

13. Equivalent plastic strain of substrate per substrate tail area (SEP_5) [1/μm^2]

$$SEP_5 = \frac{1}{A_{TS}} \cdot \frac{1}{n} \cdot \sum_{1}^{n} (PS)^{Substrate} \tag{32}$$

14. Combination of equivalent plastic strain of wire per wire tail area and equivalent plastic strain of substrate per substrate tail area (SEP_8) [1/μm^2]

$$SEP_8 = \frac{1}{(A_{TW} \cdot A_{TS})} \cdot \frac{1}{n} \sum_{1}^{n} [(PS)^{Wire} \cdot (PS)^{Substrate}] \tag{33}$$

15. Average of equivalent plastic strain of wire per wire tail area and equivalent plastic strain of substrate per substrate tail area (SEP_{11}) [1/μm^4]

$$SEP_{11} = \frac{1}{average(A_{TW}, A_{TS})} \cdot \frac{1}{n} \cdot \frac{1}{2} \sum_{1}^{n} [(PS)^{Wire} + (PS)^{Substrate}] \tag{34}$$

16. Equivalent plastic strain of wire per wire wedge area (SEP_3) [1/μm^2]

$$SEP_3 = \frac{1}{A_{WW}} \cdot \frac{1}{n} \cdot \sum_{1}^{n} (PS)^{wire} \tag{35}$$

17. Equivalent plastic strain of substrate per substrate wedge area (SEP_6) [1/μm^2]

$$SEP_6 = \frac{1}{A_{WS}} \cdot \frac{1}{n} \cdot \sum_{1}^{n} (PS)^{Substrate} \tag{36}$$

18. Combination of equivalent plastic strain of wire per wire wedge area and equivalent plastic strain of substrate per substrate wedge area (SEP_9) [1/μm^2]

$$SEP_9 = \frac{1}{(A_{WW} \cdot A_{WS})} \cdot \frac{1}{n} \sum_{1}^{n} [(PS)^{Wire} \cdot (PS)^{Substrate}] \tag{37}$$

19. Average of equivalent plastic strain of wire per wire wedge area and equivalent plastic strain of substrate per substrate wedge area (SEP_{12}) [1/μm^4]

$$SEP_{12} = \frac{1}{average(A_{WW}, A_{WS})} \cdot \frac{1}{n} \cdot \frac{1}{2} \sum_{1}^{n} [(PS)^{Wire} + (PS)^{Substrate}] \tag{38}$$

20. Sliding distance of wire per wire contact area (SES_1) [1/μm]

$$SES_1 = \frac{1}{A_{CW}} \cdot \frac{1}{n} \cdot \sum_{1}^{n} (SD)^{wire} \tag{39}$$

21. Sliding distance of substrate per substrate contact area (SES_4) [1/μm]

$$SES_4 = \frac{1}{A_{CS}} \cdot \frac{1}{n} \cdot \sum_{1}^{n} (SD)^{Substrate} \tag{40}$$

22. Combination of sliding distance of wire per wire contact area and sliding distance of substrate per substrate contact area (SES_7) [1/µm]

$$SES_7 = \frac{1}{(A_{CW} \cdot A_{CS})} \cdot \frac{1}{n} \sum_{1}^{n} [(SD)^{Wire} \cdot (SD)^{Substrate}] \tag{41}$$

23. Average of sliding distance of wire per wire contact area and sliding distance of substrate per substrate contact area (SES_{10}) [1/µm^2]

$$SES_{10} = \frac{1}{average(A_{CW}, A_{CS})} \cdot \frac{1}{n} \cdot \frac{1}{2} \sum_{1}^{n} [(SD)^{Wire} + (SD)^{Substrate}] \tag{42}$$

24. Sliding distance of wire per wire tail area (SES_2) [1/µm]

$$SES_2 = \frac{1}{A_{TW}} \cdot \frac{1}{n} \cdot \sum_{1}^{n} (SD)^{wire} \tag{43}$$

25. Sliding distance of substrate per substrate tail area (SES_5) [1/µm]

$$SES_5 = \frac{1}{A_{TS}} \cdot \frac{1}{n} \cdot \sum_{1}^{n} (SD)^{Substrate} \tag{44}$$

26. Combination of sliding distance of wire per wire tail area and sliding distance of substrate per substrate tail area (SES_8) [1/µm]

$$SES_8 = \frac{1}{(A_{TW} \cdot A_{TS})} \cdot \frac{1}{n} \sum_{1}^{n} [(SD)^{Wire} \cdot (SD)^{Substrate}] \tag{45}$$

27. Average of sliding distance of wire per wire tail area and sliding distance of substrate per substrate tail area (SES_{11}) [1/µm^2]

$$SEPS_{11} = \frac{1}{average(A_{TW}, A_{TS})} \cdot \frac{1}{n} \cdot \frac{1}{2} \sum_{1}^{n} [(SD)^{Wire} + (SD)^{Substrate}] \quad (46)$$

28. Sliding distance of wire per wire wedge area (SES_3) [1/μm]

$$SES_3 = \frac{1}{A_{WW}} \cdot \frac{1}{n} \cdot \sum_{1}^{n} (SD)^{wire} \quad (47)$$

29. Sliding distance of substrate per substrate wedge area (SES_6) [1/μm]

$$SES_6 = \frac{1}{A_{WS}} \cdot \frac{1}{n} \cdot \sum_{1}^{n} (SD)^{Substrate} \quad (48)$$

30. Combination of sliding distance of wire per wire wedge area and sliding distance of substrate per substrate wedge area (SES_9) [1/μm]

$$SES_9 = \frac{1}{(A_{WW} \cdot A_{WS})} \cdot \frac{1}{n} \sum_{1}^{n} [(SD)^{Wire} \cdot (SD)^{Substrate}] \quad (49)$$

31. Average of sliding distance of wire per wire wedge area and sliding distance of substrate per substrate wedge area (SES_{12}) [1/μm^2]

$$SES_{12} = \frac{1}{average(A_{WW}, A_{WS})} \cdot \frac{1}{n} \cdot \frac{1}{2} \sum_{1}^{n} [(SD)^{Wire} + (SD)^{Substrate}] \quad (50)$$

32. Equivalent plastic strain of wire per wire contact area ($FESEP_1$) multiplied by frictional energy [μJ/μm^2]

$$FESEP_1 = \frac{FE}{A_{CW}} \cdot \frac{1}{n} \cdot \sum_{1}^{n} (PS)^{wire} \quad (51)$$

33. Equivalent plastic strain of substrate per substrate contact area ($FESEP_4$) multiplied by frictional energy [μJ/μm^2]

$$FESEP_4 = \frac{FE}{A_{CW}} \cdot \frac{1}{n} \cdot \sum_{1}^{n} (PS)^{Substrate} \tag{52}$$

34. Combination of equivalent plastic strain of wire per wire contact area and equivalent plastic strain of substrate per substrate contact area ($FESEP_7$) multiplied by frictional energy [μJ/μm^2]

$$FESEP_7 = \frac{FE}{(A_{CW} \cdot A_{CS})} \cdot \frac{1}{n} \sum_{1}^{n} [(PS)^{Wire} \cdot (PS)^{Substrate}] \tag{53}$$

35. Average of equivalent plastic strain of wire per wire contact area and equivalent plastic strain of substrate per substrate contact area ($FESEP_{10}$) multiplied by frictional energy [μJ/μm^4]

$$FESEP_{10} = \frac{FE}{average(A_{CW}, A_{CS})} \cdot \frac{1}{n} \cdot \frac{1}{2} \sum_{1}^{n} [(PS)^{Wire} + (PS)^{Substrate}] \tag{54}$$

36. Equivalent plastic strain of wire per wire tail area ($FESEP_2$) multiplied by frictional energy [μJ/μm^2]

$$FESEP_2 = \frac{FE}{A_{TW}} \cdot \frac{1}{n} \cdot \sum_{1}^{n} (PS)^{wire} \tag{55}$$

37. Equivalent plastic strain of substrate per substrate tail area ($FESEP_5$) multiplied by frictional energy [μJ/μm^2]

$$FESEP_5 = \frac{FE}{A_{TS}} \cdot \frac{1}{n} \cdot \sum_{1}^{n} (PS)^{Substrate} \tag{56}$$

38. Combination of equivalent plastic strain of wire per wire tail area and equivalent plastic strain of substrate per substrate tail area ($FESEP_8$) multiplied by frictional energy [µJ/µm^2]

$$FESEP_8 = \frac{FE}{(A_{TW} \cdot A_{TS})} \cdot \frac{1}{n} \sum_{1}^{n} [(PS)^{Wire} \cdot (PS)^{Substrate}] \tag{57}$$

39. Average of equivalent plastic strain of wire per wire tail area and equivalent plastic strain of substrate per substrate tail area ($FESEP_{11}$) multiplied by frictional energy [µJ/µm^4]

$$FESEP_{11} = \frac{FE}{average(A_{TW}, A_{TS})} \cdot \frac{1}{n} \cdot \frac{1}{2} \sum_{1}^{n} [(PS)^{Wire} + (PS)^{Substrate}] \tag{58}$$

40. Equivalent plastic strain of wire per wire wedge area ($FESEP_3$) multiplied by frictional energy [1/µm^2]

$$FESEP_3 = \frac{FE}{A_{WW}} \cdot \frac{1}{n} \cdot \sum_{1}^{n} (PS)^{wire} \tag{59}$$

41. Equivalent plastic strain of substrate per substrate wedge area ($FESEP_6$) multiplied by frictional energy [µJ/µm^2]

$$FESEP_3 = \frac{FE}{A_{WS}} \cdot \frac{1}{n} \cdot \sum_{1}^{n} (PS)^{Substrate} \tag{60}$$

42. Combination of equivalent plastic strain of wire per wire wedge area and equivalent plastic strain of substrate per substrate wedge area ($FESEP_9$) multiplied by frictional energy [µJ/µm^2]

$$FESEP_9 = \frac{FE}{(A_{WW} \cdot A_{WS})} \cdot \frac{1}{n} \sum_{1}^{n} [(PS)^{Wire} \cdot (PS)^{Substrate}] \tag{61}$$

43. Average of equivalent plastic strain of wire per wire wedge area and equivalent plastic strain of substrate per substrate wedge area (SEP_{12}) multiplied by frictional energy [μJ/μm^4]

$$FESEP_{12} = \frac{FE}{average(A_{WW}, A_{WS})} \cdot \frac{1}{n} \cdot \frac{1}{2} \sum_{1}^{n} [(PS)^{Wire} + (PS)^{Substrate}] \tag{62}$$

44. Sliding distance of wire per wire contact area ($FESES_1$) multiplied by frictional energy [μJ/μm]

$$FESES_1 = \frac{FE}{A_{CW}} \cdot \frac{1}{n} \cdot \sum_{1}^{n} (SD)^{wire} \tag{63}$$

45. Sliding distance of substrate per substrate contact area ($FESES_4$) multiplied by frictional energy [μJ/μm]

$$FESES_4 = \frac{FE}{A_{CS}} \cdot \frac{1}{n} \cdot \sum_{1}^{n} (SD)^{Substrate} \tag{64}$$

46. Combination of sliding distance of wire per wire contact area and sliding distance of substrate per substrate contact area ($FESES_7$) multiplied by frictional energy [μJ/μm]

$$FESES_7 = \frac{FE}{(A_{CW} \cdot A_{CS})} \cdot \frac{1}{n} \sum_{1}^{n} [(SD)^{Wire} \cdot (SD)^{Substrate}] \tag{65}$$

47. Average of sliding distance of wire per wire contact area and sliding distance of substrate per substrate contact area ($FESES_{10}$) multiplied by frictional energy [μJ/μm^2]

$$FESES_{10} = \frac{FE}{average(A_{CW}, A_{CS})} \cdot \frac{1}{n} \cdot \frac{1}{2} \sum_{1}^{n} [(SD)^{Wire} + (SD)^{Substrate}] \tag{66}$$

48. Sliding distance of wire per wire tail area ($FESES_2$) multiplied by frictional energy [μJ/μm]

$$FESES_2 = \frac{FE}{A_{TW}} \cdot \frac{1}{n} \cdot \sum_{1}^{n} (SD)^{wire} \tag{67}$$

49. Sliding distance of substrate per substrate tail area ($FESES_5$) multiplied by frictional energy [μJ/μm]

$$FESES_5 = \frac{FE}{A_{TS}} \cdot \frac{1}{n} \cdot \sum_{1}^{n} (SD)^{Substrate} \tag{68}$$

50. Combination of sliding distance of wire per wire tail area and sliding distance of substrate per substrate tail area ($FESES_8$) multiplied by frictional energy [μJ/μm]

$$FESES_8 = \frac{FE}{(A_{TW} \cdot A_{TS})} \cdot \frac{1}{n} \sum_{1}^{n} [(SD)^{Wire} \cdot (SD)^{Substrate}] \tag{69}$$

51. Average of sliding distance of wire per wire tail area and sliding distance of substrate per substrate tail area ($FESES_{11}$) multiplied by frictional energy [μJ/μm^2]

$$FESES_{11} = \frac{FE}{average(A_{TW}, A_{TS})} \cdot \frac{1}{n} \cdot \frac{1}{2} \sum_{1}^{n} [(SD)^{Wire} + (SD)^{Substrate}] \tag{70}$$

52. Sliding distance of wire per wire wedge area ($FESES_3$) multiplied by frictional energy [μJ/μm]

$$FESES_3 = \frac{FE}{A_{WW}} \cdot \frac{1}{n} \cdot \sum_{1}^{n} (SD)^{wire} \tag{71}$$

53. Sliding distance of substrate per substrate wedge area ($FESES_6$) multiplied by frictional energy [μJ/μm]

$$FESES_6 = \frac{FE}{A_{WS}} \cdot \frac{1}{n} \cdot \sum_{1}^{n} (SD)^{Substrate} \tag{72}$$

54. Combination of sliding distance of wire per wire wedge area and sliding distance of substrate per substrate wedge area ($FESES_9$) multiplied by frictional energy [µJ/µm]

$$FESES_9 = \frac{FE}{(A_{WW} \cdot A_{WS})} \cdot \frac{1}{n} \sum_{1}^{n} [(SD)^{Wire} \cdot (SD)^{Substrate}] \tag{73}$$

55. Average of sliding distance of wire per wire wedge area and sliding distance of substrate per substrate wedge area ($FESES_{12}$) multiplied by frictional energy [µJ/µm^2]

$$FESES_{12} = \frac{FE}{average(A_{WW}, A_{WS})} \cdot \frac{1}{n} \cdot \frac{1}{2} \sum_{1}^{n} [(SD)^{Wire} + (SD)^{Substrate}] \tag{74}$$